

Structure sensitivity in nanoparticle catalysis : for Fischer-Tropsch and other hydrogenation reactions

Citation for published version (APA):

Quek, X. Y. (2013). *Structure sensitivity in nanoparticle catalysis : for Fischer-Tropsch and other hydrogenation reactions*. [Phd Thesis 1 (Research TU/e / Graduation TU/e), Chemical Engineering and Chemistry]. Technische Universiteit Eindhoven. <https://doi.org/10.6100/IR754783>

DOI:

[10.6100/IR754783](https://doi.org/10.6100/IR754783)

Document status and date:

Published: 01/01/2013

Document Version:

Publisher's PDF, also known as Version of Record (includes final page, issue and volume numbers)

Please check the document version of this publication:

- A submitted manuscript is the version of the article upon submission and before peer-review. There can be important differences between the submitted version and the official published version of record. People interested in the research are advised to contact the author for the final version of the publication, or visit the DOI to the publisher's website.
- The final author version and the galley proof are versions of the publication after peer review.
- The final published version features the final layout of the paper including the volume, issue and page numbers.

[Link to publication](#)

General rights

Copyright and moral rights for the publications made accessible in the public portal are retained by the authors and/or other copyright owners and it is a condition of accessing publications that users recognise and abide by the legal requirements associated with these rights.

- Users may download and print one copy of any publication from the public portal for the purpose of private study or research.
- You may not further distribute the material or use it for any profit-making activity or commercial gain
- You may freely distribute the URL identifying the publication in the public portal.

If the publication is distributed under the terms of Article 25fa of the Dutch Copyright Act, indicated by the "Taverne" license above, please follow below link for the End User Agreement:

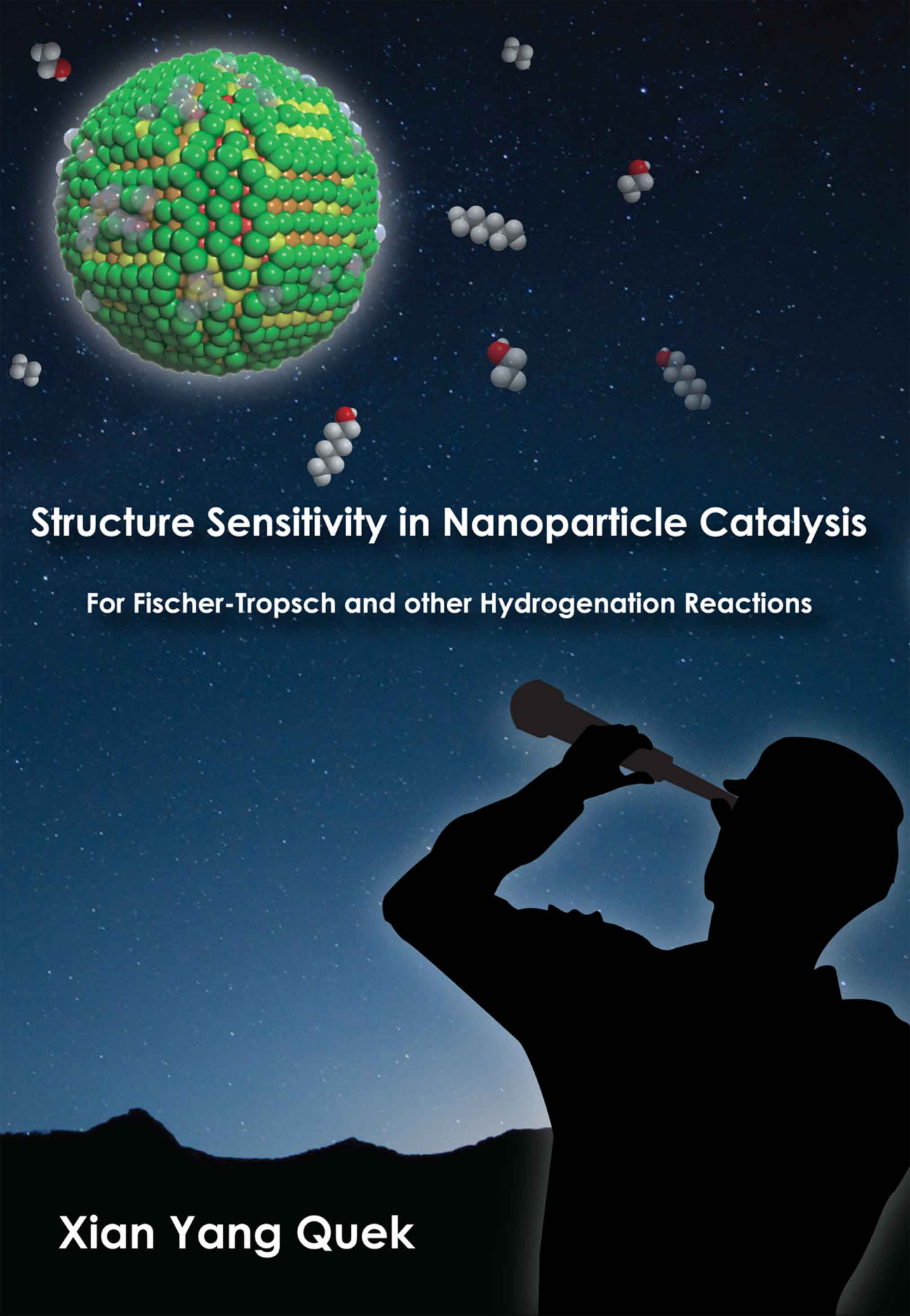
www.tue.nl/taverne

Take down policy

If you believe that this document breaches copyright please contact us at:

openaccess@tue.nl

providing details and we will investigate your claim.



Structure Sensitivity in Nanoparticle Catalysis

For Fischer-Tropsch and other Hydrogenation Reactions

Xian Yang Quek

Structure Sensitivity in Nanoparticle Catalysis

For Fischer-Tropsch and other Hydrogenation Reactions

PROEFSCHRIFT

ter verkrijging van de graad van doctor aan de
Technische Universiteit Eindhoven, op gezag van de
rector magnificus, prof.dr.ir. C.J. van Duijn, voor een
commissie aangewezen door het College voor
Promoties in het openbaar te verdedigen
op dinsdag 18 juni 2013 om 16.00 uur

door

Xian Yang Quek

geboren te Singapore, Singapore

Dit proefschrift is goedgekeurd door de promotoren:

prof.dr.ir. E.J.M. Hensen

en

prof.dr. R.A. van Santen

Xian Yang Quek

Structure Sensitivity in Nanoparticle Catalysis for Fischer-Tropsch and other Hydrogenation Reactions

A catalogue record is available from the Eindhoven University of Technology Library

ISBN: 978-90-386-3388-6

Copyright © 2013 by Xian Yang Quek

The work described in this thesis has been carried out at the Schuit Institute of Catalysis, within the Laboratory of Inorganic Materials Chemistry, Eindhoven University of Technology, The Netherlands. Financial support has been provided by the Dutch National Research School Combination Catalysis Controlled by Chemical Design (NRSC-Catalysis).

Cover design: Bryan Ng, Xian Yang Quek

Printed at Ipskamp Drukkers

*Dedicated to my wife Winnie
and my parents*

*“It is not difficult circumstances that defeat one, but one's own weakness”
(Daisaku Ikeda, Buddhist Philosopher)*

Table of Contents

Structure Sensitivity in Nanoparticle Catalysis For Fischer-Tropsch and other Hydrogenation Reactions

Chapter 1	1
<i>Introduction and Outline</i>	
Chapter 2	19
<i>Unprecedented Oxygenate Selectivity in Aqueous Phase Fischer-Tropsch Synthesis by Ruthenium Nanoparticles</i>	
Chapter 3	35
<i>Structure Sensitivity in Ru Nanoparticles Catalyzed Fischer-Tropsch Synthesis: Catalyst Characterization</i>	
Chapter 4	49
<i>Structure Sensitivity in Ru Nanoparticles Catalyzed Fischer-Tropsch Synthesis: Catalytic Performance</i>	
Chapter 5	77
<i>Effect of the Organic Capping Agent on Ru-Nanoparticle Catalyzed Aqueous Phase Fischer-Tropsch Synthesis</i>	
Chapter 6	93
<i>Structure Sensitivity in the Hydrogenation of Unsaturated Hydrocarbons over Rh Nanoparticles</i>	
Chapter 7	109
<i>Ionic Liquid Stabilized Rh Nanoparticles for Citral Cyclodehydration</i>	
Summary	121
Acknowledgements	125
List of Publications	129
Curriculum Vitae	131

Chapter 1

Introduction and Outline

Summary

Catalysis has played an important role in providing energy needs in the past and will continue to be of paramount importance for the processing of alternative feedstocks to meet future energy demands. For instance, catalysts are being used in the Fischer-Tropsch synthesis, where a mixture of CO and H₂ derived from either natural gas, coal, or biomass, is converted into clean fuels. Current understanding on the Fischer-Tropsch (FT) mechanism and the catalyst used are discussed. The elementary reaction steps in the Fischer-Tropsch reaction are strongly influenced by the structure of the catalyst, which can be affected by the particle size. The basis of using colloidal chemistry to control the size and morphology of transition metal particles and their applications catalytic reactions are illustrated. This chapter concludes with the scope of this thesis, which aims to understand the structure sensitivity in Fischer-Tropsch catalysis.

1.1 Energy and Catalysis

The 20th century has experienced a vast advancement in science and technology through the exploitation of cheap and portable energy sources. Oil, in particular, has played a major role to enable the enormous improvement in the quality of life. The extraction of energy and valuable products from oil has evolved significantly with increasing complexity. The first oil refinery was built around the middle of the 19th century, used atmospheric distillation to produce kerosene for lighting. Naphtha (gasoline) was the major by-product [1]. However, within several decades, the introduction of the internal combustion engine shifted the demand from kerosene to gasoline. Subsequently, numerous catalytic reactions such as cracking, isomerization, hydrotreating, alkylation, isomerization, and hydrogenation were introduced into refineries to meet the escalating demand for transportation fuel and also to conform to increasingly stringent environmental regulations.

With the oil reserves estimated to last for about 50 years [2], it is unrealistic to rely solely on the refining and catalytic conversion of crude oil to meet the soaring energy demand. In the last few decades, a significant amount of research and investments have been made to reduce the world's dependence on crude oil. One possible solution to address the concern for diminishing oil reserves and soaring oil price is to utilize other carbon sources for energy. Viable short term substitutions for crude oil include natural gas and coal, which are expected to last for another 63 and 112 years [2]. Recently, attempts have been made to explore the extraction of energy from unconventional sources, such as shale gas and methane hydrates. This is because a conservative estimate on the amount of carbon bounded in methane hydrates is more than twice the amount of carbon in all fossil fuel [3]. However, existing technologies are still unable to extract and utilize methane hydrates.

Apart from being a non-renewable resource, the direct utilization of natural gas and coal has its disadvantages. The major drawback for the relatively clean natural gas utilization is that many locations where natural gas can be exploited are remote from where it can be utilized. Transportation is thus needed. However, its low density leads to very high transportation costs. Coal is considered as an extremely "dirty" source of energy due to the high carbon to hydrogen ratio and high sulphur content. Therefore, the utilization of coal is very detrimental to the environment. Furthermore, the exploitation of fossil fuels in the past century has resulted in a rapid increase in the emission of carbon dioxide (CO₂), which is a major greenhouse gas (GHG). Although attempts were made to mitigate the accumulation of GHG in the atmosphere by carbon capture and sequestration, there is a huge imbalance in the

carbon cycle, due to the continuous burning of fossil fuels for energy. In order to restore the balance in the carbon cycle, energy has to be derived from a renewable carbon sources instead of fossil fuels. Various government bodies have identified biomass as a plausible alternative for fossil fuel [4-5]. However, direct utilization of biomass is often not feasible. In addition to the need of laborious transportation, the high oxygen to carbon ratio in biomass is incompatible with existing infrastructure, such as vehicles, refineries and chemical plants. Hence, the utilization of natural gas, coal and biomass requires considerable technological developments to enable large scale application and to address environmental concerns.

In comparison to crude oil, the processing of natural gas, coal and biomass is much more intricate due to the higher stability of the reacting molecules and/or the presence of extensive polymeric carbon networks containing functional groups with oxygen, sulphur, or nitrogen. Hence the use of catalysts will play a major role in the technological development of conversion process for natural gas, coal and biomass.

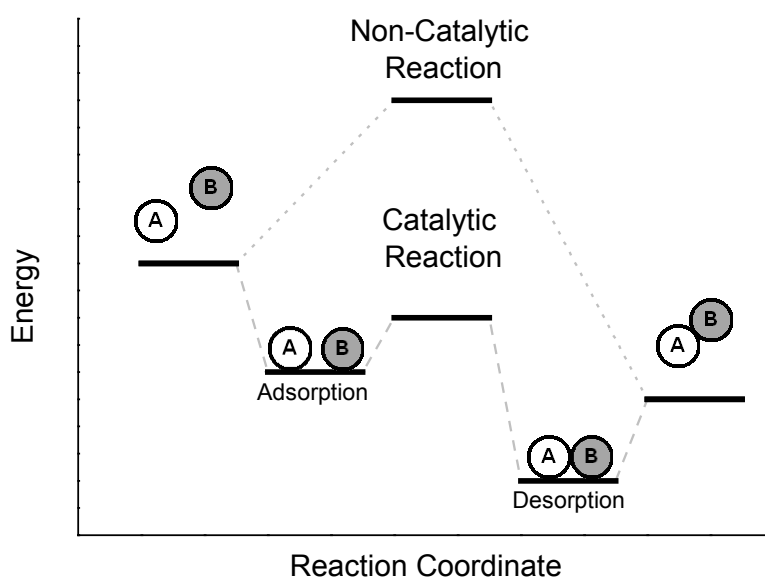


Figure 1.1: Potential energy diagram for catalysed and uncatalysed reaction (modified from [6]).

A catalyst typically accelerates chemical reactions, where chemical bonds are dissociated or combined. Interactions between the catalyst and the reactants lower the reaction energy barrier. However, the catalyst does not alter the thermodynamics of the reaction, hence the overall change in free energy remains the same. As illustrated in the potential energy diagram in Figure 1.1, the intimate contact between the catalyst and the reactants results in an energetically more favourable pathway compared to the uncatalysed reaction. Although the close interaction between reactants, intermediates, products, and catalyst increases the complexity of the reaction pathway, new reaction pathways are being

open. Consequently, implementation of a catalyst needs to be perfectly tuned to reach the desired outcome. For instance, an optimum strength of interaction between the catalyst and the reactants is required. When the reactants are too weakly bonded to the catalyst, there will be no or very little conversion of the reactants to form the product. On the contrary, too strongly bonded reactants, intermediates, or products will result in stable surface species. Consequently, the formation and desorption of the product becomes extremely difficult, and the catalyst is being poisoned. Hence, successful implementation of a catalytic reaction requires understanding of the catalytic properties and the reaction at the molecular level.

1.2 Catalyst Structure

In all three classifications of catalysis, namely (1) biocatalysis, (2) homogeneous catalysis, and (3) heterogeneous catalysis, the structure of the catalyst influences the reaction. Biocatalysis uses nature's catalysts, i.e., enzymes, to catalyze reactions. Enzymes are large proteins. Besides their catalytic properties the structure of the proteins imposes a steric effect, allowing only the reacting molecule to be accommodated at the active site with an optimum configuration for the reaction to take place [7]. The structure of the enzyme also directs the reaction to produce only the targeted molecules. In homogeneous catalysis, both the reactants and the catalyst are in the same phase. Homogeneous catalysis typically uses an organometallic compound to catalyse the reaction and the reaction occurs at the metal center. The structure of a homogeneous catalyst is determined by the ligand attached to the metal center [8]. Similar to enzymes, the ligand attached imposes an electronic and a steric effect on the reacting molecules. As a result, the ligand influence the way which reactants are bonded to the metal center and configuration of the reaction intermediates formed. In contrast to homogeneous catalysis, the reactants and the catalyst exist in different phases for heterogeneous catalysis. Typically, a solid catalyst is used to convert liquid or gaseous reactants. An example where the structure of heterogeneous catalysis imposes a steric effect on the reacting molecules is the application of ordered porous structures, such as zeolites and Metal-Organic-Framework (MOFs). In contrast to earlier examples where the structure of the catalyst imposes a steric effect, the influence of the catalyst structure when supported metal particles are applied in heterogeneous catalysis is very different. In this instant, the structure of the catalyst does not enclose the reacting molecules. Nevertheless, the structure of the reactive site on the catalyst surface still has significant influence on its catalytic behaviour. In metal catalysis the structure can be defined as the number and kind of neighbouring atoms.

Due to the intimate contact of the surface metal atoms with its neighbouring metal atoms, the coordination number of the metal atoms will have tremendous influence on the interaction with reactants, intermediates and products and hence on the catalytic reactivity [9-10].

1.2.1 Structure Sensitivity in Metal Catalysis

Since catalytic reactions take place only on the surface, nanosized metal particles are typically used in catalysis to maximize the catalyst efficiency by increasing the exposed surface. On these small particles, an appreciable amount of active surface sites with a low coordination number such as edges and corners are present. In addition, defects sites such as kinks and steps are also presents. Therefore, particle size variations are of relevance to the structure of the active site. Based on extensive work in the 1960s and 1970s, Boudart classified reactions as structure sensitive or structure insensitive [11-13]. Boudart distinctly demonstrated that ammonia synthesis over supported Fe catalyst is a structure sensitive reaction [14], while hydrogenation of cyclopropane over Pt catalyst is a structure insensitive reaction [15-16]. These results were subsequently verified by Somorjai using surface science techniques [17-18]. Based on the understanding of structure sensitivity/in-sensitive-reactivity, reactions were categorized into three different types, where rate normalized per exposed metal surface atom, (i) decreases, (ii) remained constant or (iii) increases with increasing particle size [9, 19].

Surface science has contributed to more in-depth understanding in structure sensitive and structure insensitive reactions by using well-defined crystal surfaces. Pioneering work of Ertl [20-21] and Somorjai [22-23] uses surface science techniques to gain greater understanding on structure sensitive reaction, in particular the contribution of step sites to the reactivity. A major breakthrough came when Ertl [20] reported direct observation of NO dissociation on the step sites, validating the importance of these sites. This stimulated the need for even greater understanding on structure sensitivity especially from a theoretical viewpoint.

In the last decade, a firm theoretical basis about surface reactivity of metals has been established through quantum chemical calculations [9-10, 24-26]. In particular, Density Functional Theory (DFT) calculations allow investigation and understanding of elementary reaction steps on metal surfaces, which are impossible to study experimentally. By integrating DFT calculations with fundamental concepts, such as Brønsted-Evans-Polanyi (BEP) relations and Sabatier principle, elementary reactions on metal surfaces can be predicted [9-10, 24]. In addition, such combination will provide further insight to the

complex relationship between the catalyst structure, the bonding structure of the reacting molecules, and the activation energy. Van Santen and co-worker have utilized DFT calculations in conjunction with fundamental concepts to explain the issue of structure sensitive and structure insensitive reaction in detail [9-10, 24].

Structure sensitivity depends strongly on the type of bonds involved in the reaction. Surface reactions involving σ -bonds (H_2 , CH_4 , NH_3 , C-C) behave very differently from those concerning π -bonds (CO , N_2 , NO). A key difference between the reactions of σ - and π -bonds relates to their mode of interaction with the metal surface. For instance, NH_3 interacts with the metal surface mainly by donation of the lone pair electron to the metal surface [9-10]. However, CO interacts with the metal surfaces via back-donation of electrons from the metal surface to the π anti-bonding orbital of CO [9-10]. Hence NH_3 interacts more strongly on metal atoms with lower coordination number where electrons are more tightly bonded, while CO interacts more favorably on metal atoms with higher coordination number where electrons are more delocalized which is better for back-donation. Based on the example as illustrated by NH_3 and CO , an implication is that reaction of σ -bond will occur over a single metal atom while reaction for π -bond requires an ensemble of surface atoms.

BEP relations correlates the change in activation energy of an elementary reaction to the change in the reaction energy [10, 24]. An important prerequisite to apply BEP relations is that the transition state structure has to be similar [10]. Since reactions of σ -bonds occur over a single metal atom where the change in the local surface structure of the catalyst does not affect the transition state structure, BEP relations can be applied. The dissociation of a σ -bond, such as the C-H bond in CH_4 , is characterized with a late transition state, where the transition state structure resembles the final state structure [10, 24]. BEP considerations predict that lower surface metal atom coordination number will lead to lower reaction barrier for σ -bond activation due to stabilization of the transition and final states caused by an increase in adsorption energies. Conversely, the reverse reaction where σ -bond is formed is characterized by an early transition state, where the transition state structure resembles the initial state structure [10, 24]. This implies that attempts to stabilize the transition state by a more reactive surface metal atom will also stabilize the initial state. Hence activation barrier for σ -bond formation does not change significantly with change in coordination number. This view relates to the concept of microscopic reversibility [10, 24].

In contrast to reactions involving σ -bonds, changes in surface topology of the catalyst have drastic impact on the transition state configuration for molecules with π -bond. For

instance, the transition state configuration for CO dissociation on the terrace and step sites will lead to very different transition state structure as shown in Figure 1.2. Therefore, BEP relation is not valid when comparing reaction of π -bond on surfaces with different topology. The different transition state configurations have profound influence on the reactivity. For example, CO dissociation on a Ru(0001) surface requires the dissociating C and O atoms to share a metal atom in the transition state where the CO bond is being stretched (Figure 1.2a). This sharing of metal atom will lead to a repulsive interaction, which destabilize the transition state and increase the activation barrier [9-10]. DFT calculations predict the activation barrier of CO dissociation on a Ru(0001) close-packed surface to be 224 kJ/mol, indicating that the reaction is not feasible on terrace sites [27]. In contrast, CO dissociation on step sites does not require the sharing of a metal atom in the transition state as the C and O atoms bind to the bottom and edge of the step, respectively (Figure 1.2b). Hence the transition state is not being destabilized. In addition, the transition state configuration over step sites enhances the back-donation of electrons from the step-edge metal atoms to the antibonding orbital, which weakens the CO bond. This lowers the reaction barrier for CO dissociation on step sites compared to terrace sites. Similar arguments hold for the recombination of C and O to form CO.

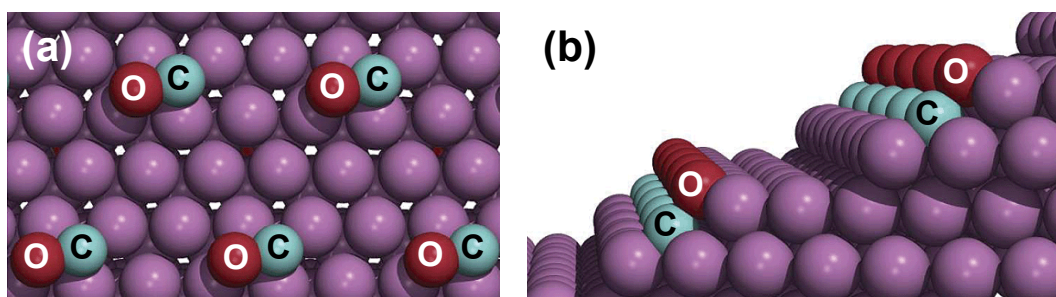


Figure 1.2: Transition state for CO dissociation on (a) close pack sites, and (b) step sites (reprinted from [27]).

Based on understanding on the reactivity of σ -bond and π -bonds with respect to the surface topology, the relation between structure sensitivity and particle size can be understood at the molecular level [9-10, 24]. Decreasing the metal particle size of the catalyst increases the number of low coordination sites. Since lower coordination number would stabilize the transition state for σ -bond dissociation, decrease in particle size would increase the rate of σ -bond dissociation. In agreement with this analysis, increase in activity with decreasing particle size have been observed for CH_4 steam reforming [28-29] and hydrogenolysis reactions [30]. Due to microscopic reversibility, the formation of σ -bond was argued to be insensitive to the change in coordination number, therefore implying that change

in particle size will not affect the surface normalized activity. Experimental evidence supporting this perspective are mainly illustrated by the particle size independence of hydrogenation reactions [15-16]. As discussed above, the dissociation/formation of π -bond requires step sites, where the reaction occurs over an ensemble of metal atoms. As small particles are not able to accommodate step sites, surface normalized activity will either show a maximum or decrease with diminishing particle size. Experimental evidences supporting this analysis include the Fischer Tropsch reaction, where a $\text{C}\equiv\text{O}$ bond has to be dissociated [31-33] and the ammonia synthesis where a $\text{N}\equiv\text{N}$ bond has to be dissociated [18, 34-35].

1.2.2 Colloidal Nanoparticles as Catalyst

Controlling the metal particle size is of paramount importance in catalysis research, especially in understanding the role of the catalyst on a molecular level. Traditionally, the preparation of catalyst with differently sized metal particles is achieved by the use of different supports, by different methods to deposit the metal precursor onto the support, or by different pretreatment temperatures and/or conditions [19]. Recent advancements in nanoscience have allowed more precise control of metal particle size and shape using colloidal chemistry. These colloidal metal particles serve as new model systems in catalytic studies, which bridge the gap between single crystal surfaces and real catalysts [23, 36-41].

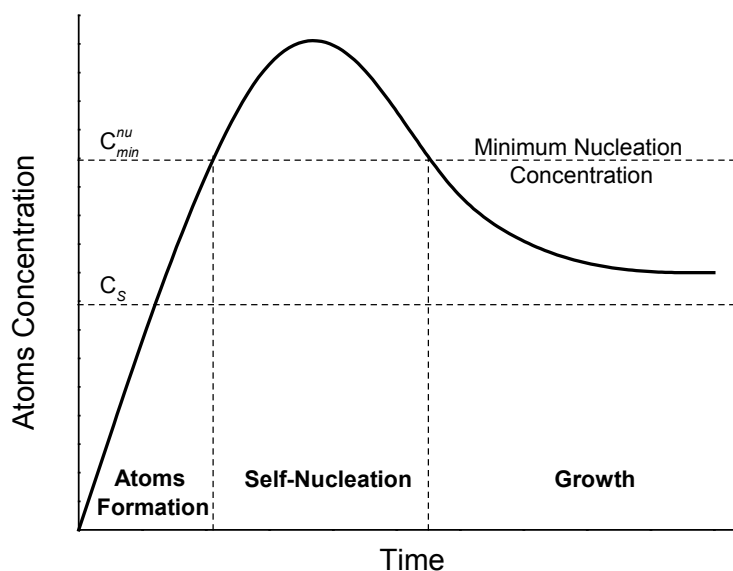


Figure 1.3: Different stages involved in the growth of metal particles (modified from [36]).

Colloidal metal nanoparticles are typically synthesized by liquid phase reduction in the presence of an organic capping agent. The capping agent controls both the reduction rate and the aggregation of the metal particles [42]. Although the chemical reactions involved in

the synthesis of these metal particles are fairly simple, the nucleation and growth mechanism are highly complex. Generally, the synthesis of these colloidal nanoparticles can be divided into three distinct stages as shown in Figure 1.3: (i) generation of (dissolved) metal atoms, (ii) nucleation and evolution of nuclei into seeds, and (iii) growth of seeds into nanoparticles. In the generation of metal atoms, a metal precursor is either decomposed or reduced to generate zero valance metal atoms. The concentration of the metal atoms increases until supersaturation (C_{min}^{nu}), where the atoms start to aggregate into nuclei by nucleation. Once the nuclei are formed, growth of the crystal occurs rapidly and the concentration of the atoms drops. However, if the concentration of the atoms decline below the minimum supersaturation (C_s), no growth will occur. Above minimum supersaturation and with the continuous formation of the atomic precursor, the nuclei will continue to grow in size forming nanoparticles. The growth will continue until equilibrium is reached between the atoms on the surfaces of the nanoparticles and the atoms in the solution.

The control of the size these nanoparticles can be achieved through selection of the reduction temperature [43], type of precursor [44-45], concentration of precursor [36], type of organic capping agent [46] and reduction time [47]. Size control of colloidal nanoparticles have been achieved over a wide range of metals, such as Pt, Pd, Ag, Au, Rh and Ru [23, 36-41, 48]. The narrow particle size distribution of these colloidal nanoparticles allows them to be applied as model systems to understand catalytic properties in reactions such as hydrogenation [49], dehydrogenation [50], oxidation [51], hydrogenolysis [30], hydroformylation [52] and C-C coupling [46] reactions.

Not only control of particle size, but also control of metal particle shape has been achieved using colloidal chemistry. Shape control of the metallic nanoparticles is even more demanding for the metal particles crystallization process. The nuclei play a very important role in shape control. Once the nuclei has grown above a critical size, forming the seeds, the structure becomes locked into a defined structure which determines the final shape of the nanoparticles [36]. Therefore in shape control of nanoparticles, it is crucial to only form seeds with the desired structure [36]. Techniques based on thermodynamic and/or kinetic control have been utilized to manipulate the shapes of Pt, Pd, Au, Ag and Rh nanoparticles [36, 41]. Although metal particles with a variety of shapes have been synthesized [36, 41], the influence of particle shapes on catalytic reactivity is less widely investigated. Catalytic studies on particle shapes have been limited to isomerization [53], oxidation [54-56] and the reduction of NO by CO [57]. Cubic particles were found to be more active compared to polyhedron particles in the oxidation of styrene [56], isomerization of 2-butene [53] and

reduction of NO [57]. However, the reactivity for CO oxidation was insensitive to the shape of particles [55].

1.3 Fischer-Tropsch Reaction

An attractive route to produce clean fuels and chemicals from natural gas, coal and biomass, is through the Fischer-Tropsch (FT) reaction [58-59]. The FT reaction converts syngas (a mixture of CO and H₂) to liquid hydrocarbons and oxygenates. Syngas can be obtained from natural gas, coal and biomass by steam reforming or gasification. The FT reaction is of increasing commercial interest and several large scale commercial plants have been built in recent years by major energy companies such as Chervon, Sasol and Shell [60].

1.3.1 Mechanisms for the Fischer-Tropsch Reaction

Despite after eighty years of research, the mechanism for the FT reaction is still an intensely debated topic. Among the various mechanisms proposed to account for the formation of long-chain hydrocarbons [61], the carbide mechanism has found most support in literature. According to this mechanism, the building blocks for chain growth are CH_x surface intermediates [61-62]. The Fischer-Tropsch reaction comprises three main surface reaction steps as depicted in Figure 1.4: (i) CO dissociation and formation of CH_x intermediates, (ii) chain growth by CH_x insertion and subsequent hydrogen transfer steps, and (iii) termination to form the final product. On surfaces of low reactivity CO dissociation may proceed via an H-assisted pathway [27, 63] as an alternative to direct CO dissociation [64]. For the chain growth step involving CH_x surface intermediates, different routes have been considered such as the Brady-Pettit alkyl [65] and the Gaube-Maitlis alkelydene/alkenyl [66] mechanisms. The Brady-Pettit alkyl mechanism involves insertion of CH₂ into the alkyl chain [67]. In contrast, the Maitlis alkenyl mechanism involves the coupling between CH and CH₂ to form an alkenyl and subsequently chain growth involve the insertion of CH₂ into the alkenyl followed by allyl-vinyl isomerization [67]. The Gaube alkelydene mechanism is relatively similar to the Maitlis mechanism where CH₂ is used as the building block. However in the Gaube mechanism, the growing chain is an alkelydene species and hydrogen transfer to generate the alkenyl intermediate is required for continuous chain growth. There are three different termination steps possible, namely H-addition, β-H elimination and CO insertion giving rise to paraffins, olefins and oxygenates, respectively.

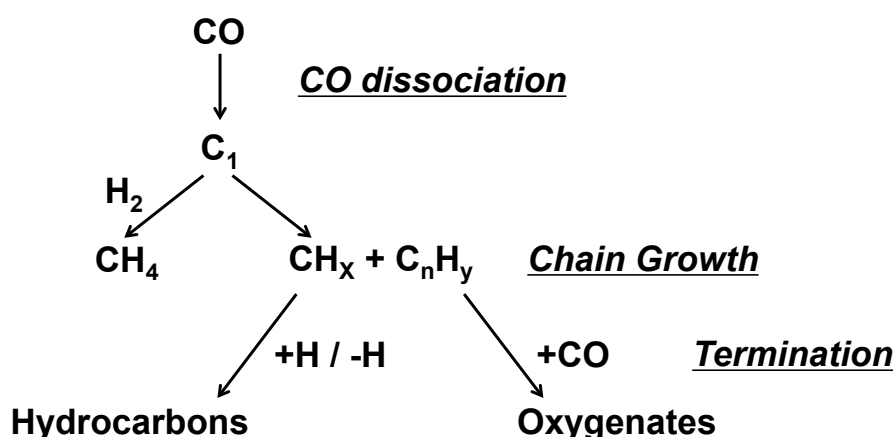


Figure 1.4: The Carbide mechanism for the FT reaction (modified from [61]).

Within the carbide mechanism, in order to form long chain products the rate of CO dissociation has to be fast and the rate of methane formation slow to provide sufficient CH_x intermediates to maintain a high rate of chain growth [61]. Also, the formation of long chain products requires the rate of termination to be slow compared to the rate of chain growth. This implies that in the carbide mechanism an increased rate of chain termination by CO insertion or through hydrogen transfer reactions would decrease chain growth, and accordingly the chain growth probability (α). When oxygenate formation and hydrocarbon formation is the result of competition for the same growing adsorbed hydrocarbon chain increased selectivity towards oxygenate formation implies that the intrinsic rate for chain termination to oxygenates is faster than that for chain termination to hydrocarbon. In this case, the chain growth probabilities of both products would be the same.

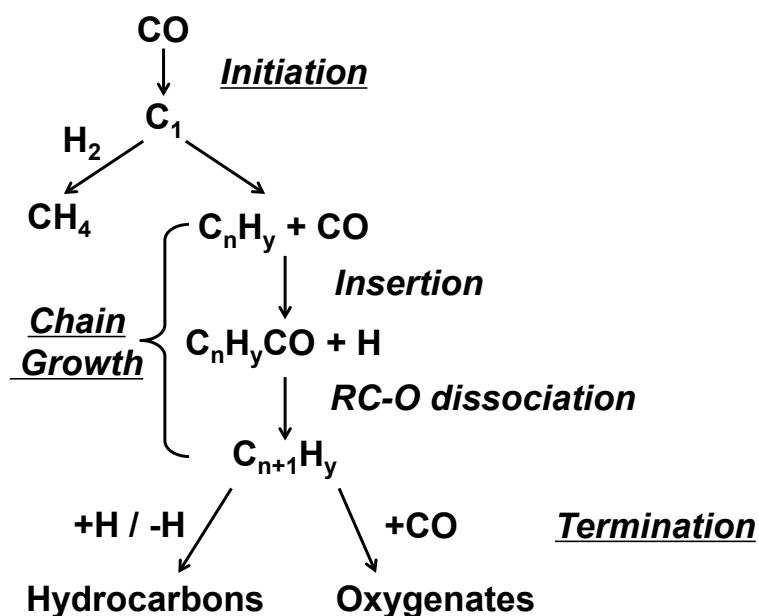


Figure 1.5: The CO-insertion mechanism for the FT reaction (modified from [61]).

The main alternative proposal to the carbide mechanism for the FT reaction is the CO-insertion mechanism formulated by Pichler and Schulz [68-69] as shown in Figure 1.5. In this mechanism, CO is the building block for chain growth. There are also three main steps in the CO-insertion mechanism: (i) initiation, (ii) chain growth and (iii) termination. In this mechanism, the chain growth step consist the insertion of CO into the growing chain followed by the RC-O dissociation. In order to yield long chain product, the insertion of CO followed by the RC-O dissociation has to be faster than the rate of termination [61]. Similar to the carbide mechanism, the reaction can terminate in three different ways to form paraffins, olefins and oxygenates. However termination by CO-insertion for the formation of oxygenates will compete with the chain growth step.

Based on extensive DFT studies on the FT mechanism, it was concluded in a recent review that the carbide mechanism is the most probable mechanism for FT chain growth [61]. CO-insertion mechanism was rejected due to the high energy requirements [61]. DFT calculations found favorable activation energy of 79 kJ/mol for the insertion of CO to a growing chain [70], and the dissociation of the R-OH bond was observed experimentally [71]. However, the overall energy required calculated by DFT, which include the insertion of CO into alkyl chain and subsequent hydrogenation steps, was found to be approximately 180 kJ/mol [70]. This implies chain growth via the CO-insertion is not favorable.

1.3.2 Fischer-Tropsch Catalyst

Various catalysts were found to be active for FT to produce both hydrocarbons [58-59, 72-73] and oxygenates [74-82]. Ru, Co and Fe are widely investigated for the formation of long chain hydrocarbons [58-59, 73]. For these catalyst, termination occurs mainly by either H-addition or β -H elimination and the rate of CO dissociation and propagation are faster than termination to form long chain hydrocarbons [61-62]. In contrast, for Ni a methanation catalyst, the weak Ni-C result in slow CO dissociation compared to termination, hence dissociated CO is instantly hydrogenated to CH₄ and no long chain products are formed [61, 83-84]. For the formation of oxygenates by CO termination, the rate of CO dissociation has to be impeded to have sufficient un-dissociated CO present on the surface. Cu, Rh and modified FT catalyst and were found to produce oxygenates during FT [85]. Cu, a methanol synthesis catalyst does not dissociate CO, hence CO is being hydrogenated to methanol and no long chain alcohols are formed [74-75]. For the higher alcohols synthesis, the catalyst must be able to dissociate CO while maintaining sufficient un-dissociated CO for

CO termination [85]. Another criterion to form long chain oxygenates is that the rate of CO termination must be slower than chain growth [61-62]. Rh being surrounded by metals which dissociate CO readily (Ru, Fe, Co) and those which do not dissociate CO (Pd, Pt, Ir), exhibits unique properties to produce C_2 oxygenates [76-79, 85]. Alternatively, by addition of promoters to FT catalyst or modifying Cu based catalyst, long chain oxygenates can also be formed [80, 86-87]. Despite this fundamental understanding of the expected product type, the formation of by-products cannot be excluded. For instance, oxygenates were found in Ru [88], Co [89] and Fe [90-91] catalyzed FT reactions.

Other than the type of transition metal used, the particle size and the crystal structure of the catalyst is also of paramount importance. For larger transition metal particles, Fischer-Tropsch catalysis can be considered as structure insensitive [92]. However for particles with dimensions below 10 nm the FT activity has been found to be a strong function of particle size [31-33, 93-95]. Recent higher temperature SSITKA data for hydrocarbon production over Ru catalysts indicate that with decreasing size of the nanoparticles, the relative fraction of reactive sites decreases without change in intrinsic activity of these sites [32]. For Co particles, there are strong indications that also the intrinsic reactivity of the reactive center changes [95]. The critical particle size below which the CO consumption rate becomes structure sensitive is in the 7-10 nm range for Co [31, 93-95] and 6-10 nm for Ru [32-33]. This structure sensitive behavior has been attributed to the decreasing stability of step-edge sites for smaller particles, which are essential for low-barrier CO dissociation, [61-62]. An alternative explanation is that CO or C atoms adsorb too strongly on small particles, thus poisoning part of the catalytic surface [31, 93-95]. Salmeron et al. recently suggest that particle size affects in FT is due to difference in the rate of H_2 dissociation [96]. It was also reported that smaller particles produce more methane and have a lower C_{5+} selectivity [31-32]. Apart from the particle size, the crystal structure of nanoparticles also affects their activity. Recent studies have found indications that *hcp*-Co is more active than *fcc*-Co [97-98].

1.4 Scope of the Thesis

The FT reaction is of increasing commercial importance and scientific interest for the production of clean fuels. Catalyst plays a critical role in the FT reaction. However, many aspects related to the FT catalysis are still not completely understood. In particular, the origin of the particle size dependence and the formation of side-products such as oxygenates during

FT have not been elucidated yet. This project aims to understand the origin of structure sensitivity of nanoparticle catalysis for several chemical reactions, including Fischer-Tropsch synthesis in the aqueous phase catalyzed by colloidal Ru particles. Although Ru is too expensive for industrial use, it is known to be the most active catalyst for the FT reaction. Hence the use of promoters is not required for Ru catalyzed FT reaction. It will be more cumbersome and complicate to relate the change in FT catalytic performance to the change in the catalyst structure in the presence of promoters.

Chapter 2 investigates aqueous-phase FT catalyzed by a colloidal Ru nanoparticle catalyst. The Ru nanoparticles are prepared by a variety of methods and post-treatment hydrogenation is employed to increase the degree of reduction. The temperature dependence of the FT reaction is studied in detail with specific attention for the product composition. The results are interpreted in terms of simple kinetic models to account for the selectivity and chain growth of the two main product classes, viz. hydrocarbons and oxygenates.

In Chapter 3, Ru nanoparticles of different size were prepared and characterized in great detail. The surface of the nanoparticles was investigated by IR spectroscopy of adsorbed CO. The bulk structure was analysed by EXAFS. The bulk and surface structure was investigated by synchrotron XRD-PDF in combination with Reverse Monte Carlo simulations. An important corollary of these studies is that the surface structure of the nanoparticles is highly disordered.

Chapter 4 examines the catalytic performance of the FT reaction of different Ru particle sizes. Activity and selectivity of aqueous phase FT strongly depends on Ru particle size. Attempts are made to understand the changes in activity, selectivity and chain growth probability in terms of lumped kinetic models to account for growth of hydrocarbons and oxygenates on different active centers. A comparison of the carbide and Pichler-Schulz mechanism will be made as well. Finally, this chapter presents correlations between the FT rate and the surface composition.

Since the synthesis of colloidal Ru nanoparticles requires the use of organic stabilizers, the effect of organic capping agent on FT activity in the aqueous phase was investigated in Chapter 5. As it would be challenging to prepare equally sized Ru nanoparticles with different capping agents, the different capping agents were placed on a carbon nanofiber supported Ru nanoparticle catalyst. The effect of the strength of the interaction of the capping agent with the Ru nanoparticles was investigated. The effect of the reaction medium for supported Ru nanoparticles in liquid phase FT is also investigated.

In Chapter 6, the effect of Rh particle size on the hydrogenation of phenylacetylene and 1-octene will be reported. The catalytic activity for phenylacetylene hydrogenation and 1-octene hydrogenation exhibits different trends with increasing Rh particle size. The possible explanations for this behaviour are discussed.

Chapter 7 illustrates an extreme example of the influence of the organic capping agent, where Rh nanoparticles stabilized by an imidazolium-based ionic-liquid (IL) act as an acid catalyst. The acid and hydrogenation function of the IL stabilized Rh nanoparticles was investigated using citral as the probe reactant. The origin of the acid function on such a catalyst is discussed.

References

- [1] K. Adler, in *Chem. Week*, **18 Sep 2002**.
- [2] *BP Statistical Review of World Energy 2012*, **2012**, BP, Retrieved 2 Mar 2013 from <http://www.bp.com/statisticalreview>
- [3] J. B. Klauda, S. I. Sandler, *Energy Fuels* **2005**, *19*, 459-470.
- [4] *Biomass Action Plan*, **2005**, Commission of the European Communities, Retrieved 2 Mar 2013 from http://ec.europa.eu/energy/res/biomass_action_plan/doc/2005_12_07_comm_biomass_action_plan_en.pdf
- [5] *Obama Announces Steps to Boost Biofuels and Clean Coal*, **2010**, Office of the Press Secretary, The White House, Retrieved 2 Mar 2013 from <http://www.whitehouse.gov/the-press-office/obama-announces-steps-boost-biofuels-clean-coal>
- [6] I. Chorkendorff, J. W. Niemantsverdriet, *Concepts of Modern Catalysis and Kinetics*, 2nd ed., Wiley, **2007**.
- [7] D. Voet, J. G. Voet, C. W. Pratt, *Fundamentals of Biochemistry: Life at the Molecular Level*, 2nd ed., Wiley, **2006**.
- [8] P. W. N. M. van Leeuwen, *Homogeneous Catalysis: Understanding the Art*, Kluwer Academic, **2004**.
- [9] R. A. van Santen, *Acc. Chem. Res.* **2009**, *42*, 57-66.
- [10] R. A. van Santen, M. Neurock, S. G. Shetty, *Chem. Rev.* **2010**, *110*, 2005-2048.
- [11] M. Boudart, *Adv. Catal.* **1969**, *20*, 153-166.
- [12] M. Boudart, *Chem. Rev.* **1995**, *95*, 661-666.
- [13] M. Boudart, *J. Mol. Catal.* **1985**, *30*, 27-38.
- [14] J. A. Dumesic, H. Topsøe, S. Khammouma, M. Boudart, *J. Catal.* **1975**, *37*, 503-512.
- [15] M. Boudart, A. Aldag, J. E. Benson, N. A. Dougharty, C. Girvin Harkins, *J. Catal.* **1966**, *6*, 92-99.
- [16] M. Boudart, L. D. Ptak, *J. Catal.* **1970**, *16*, 90-96.
- [17] D. R. Kahn, E. E. Petersen, G. A. Somorjai, *J. Catal.* **1974**, *34*, 294-306.
- [18] N. D. Spencer, R. C. Schoonmaker, G. A. Somorjai, *J. Catal.* **1982**, *74*, 129-135.
- [19] M. Che, C. O. Bennett, *Adv. Catal.* **1989**, *36*, 55-172.
- [20] T. Zambelli, J. Wintterlin, J. Trost, G. Ertl, *Science* **1996**, *273*, 1688-1690.
- [21] R. Imbihl, G. Ertl, *Chem. Rev.* **1995**, *95*, 697-733.
- [22] G. A. Somorjai, *Chem. Rev.* **1996**, *96*, 1223-1235.
- [23] G. A. Somorjai, C. Aliaga, *Langmuir* **2010**, *26*, 16190-16203.
- [24] R. A. van Santen, M. Neurock, *Molecular Heterogeneous Catalysis: A Conceptual and Computational Approach*, Wiley, **2006**.
- [25] J. K. Nørskov, T. Bligaard, J. Rossmeisl, C. H. Christensen, *Nature Chemistry* **2009**, *1*, 37-46.
- [26] B. Hammer, J. K. Nørskov, *Adv. Catal.* **2000**, *45*, 71-129.
- [27] I. M. Ciobica, R. A. van Santen, *J. Phys. Chem. B* **2003**, *107*, 3808-3812.
- [28] D. A. J. M. Ligthart, R. A. van Santen, E. J. M. Hensen, *J. Catal.* **2011**, *280*, 206-220.
- [29] J. Wei, E. Iglesia, *J. Catal.* **2004**, *225*, 116-127.
- [30] H. Song, R. M. Rioux, J. D. Hoefelmeyer, R. Komor, K. Niesz, M. Grass, P. Yang, G. A. Somorjai, *J. Am. Chem. Soc.* **2006**, *128*, 3027-3037.
- [31] G. L. Bezemer, J. H. Bitter, H. Kuipers, H. Oosterbeek, J. E. Holewijn, X. D. Xu, F. Kapteijn, A. J. van Dillen, K. P. de Jong, *J. Am. Chem. Soc.* **2006**, *128*, 3956-3964.

- [32] J. M. a. G. I. Carballo, J. Yang, A. Holmen, S. García-Rodríguez, S. Rojas, M. Ojeda, J. L. G. Fierro, *J. Catal.* **2011**, *284*, 102-108.
- [33] J. Kang, S. Zhang, Q. Zhang, Y. Wang, *Angew. Chem. Int. Ed.* **2009**, *48*, 2565-2568.
- [34] K. Honkala, A. Hellman, I. N. Remediakis, A. Logadottir, A. Carlsson, S. Dahl, C. H. Christensen, J. K. Nørskov, *Science* **2005**, *307*, 555-558.
- [35] A. M. Karim, V. Prasad, G. Mpourmpakis, W. W. Lonergan, A. I. Frenkel, J. G. Chen, D. G. Vlachos, *J. Am. Chem. Soc.* **2009**, *131*, 12230-12239.
- [36] Y. Xia, Y. J. Xiong, B. Lim, S. E. Skrabalak, *Angew. Chem. Int. Ed.* **2009**, *48*, 60-103.
- [37] G. A. Somorjai, J. Y. Park, *Top. Catal.* **2008**, *49*, 126-135.
- [38] G. A. Somorjai, A. M. Contreras, M. Montano, R. M. Rioux, *Proc. Natl. Acad. Sci.* **2006**, *103*, 10577-10583.
- [39] G. A. Somorjai, H. Frei, J. Y. Park, *J. Am. Chem. Soc.* **2009**, *131*, 16589-16605.
- [40] G. A. Somorjai, J. Y. Park, *Angew. Chem. Int. Ed.* **2008**, *47*, 9212-9228.
- [41] A. R. Tao, S. Habas, P. D. Yang, *Small* **2008**, *4*, 310-325.
- [42] N. Toshima, T. Yonezawa, *New J. Chem.* **1998**, *22*, 1179-1201.
- [43] X.-Y. Quek, Y. Guan, E. J. M. Hensen, *Catal. Today* **2012**, *183*, 72-78.
- [44] B. Chaudret, *C. R. Physique* **2005**, *6*, 117-131.
- [45] M. L. Kahn, A. Glaria, C. Pages, M. Monge, L. Saint Macary, A. Maisonnat, B. Chaudret, *J. Mater. Chem.* **2009**, *19*, 4044-4060.
- [46] R. Narayanan, M. A. El-Sayed, *J. Phys. Chem. B* **2004**, *108*, 8572-8580.
- [47] A. Beck, A. Horváth, A. Szűcs, Z. Schay, Z. E. Horváth, Z. Zsoldos, I. Dékány, L. Guczi, *Catal. Lett.* **2000**, *65*, 33-42.
- [48] D. Astruc, *Nanoparticles and Catalysis*, Wiley-VCH, **2008**.
- [49] G. S. Fonseca, A. P. Umpierre, P. F. P. Fichtner, S. R. Teixeira, J. Dupont, *Chem. Eur. J.* **2003**, *9*, 3263-3269.
- [50] R. Rioux, B. Hsu, M. Grass, H. Song, G. Somorjai, *Catal. Lett.* **2008**, *126*, 10-19.
- [51] S. H. Joo, J. Y. Park, J. R. Renzas, D. R. Butcher, W. Huang, G. A. Somorjai, *Nano Lett.* **2010**, *10*, 2709-2713.
- [52] A. J. Bruss, M. A. Gelesky, G. Machado, J. Dupont, *J. Mol. Catal. A: Chem.* **2006**, *252*, 212-218.
- [53] I. Lee, R. Morales, M. A. Albiter, F. Zaera, *Proc. Natl. Acad. Sci.* **2008**, *105*, 15241-15246.
- [54] S. Mostafa, F. Behafarid, J. R. Croy, L. K. Ono, L. Li, J. C. Yang, A. I. Frenkel, B. R. Cuenya, *J. Am. Chem. Soc.* **2010**, *132*, 15714-15719.
- [55] Y. Zhang, M. E. Grass, W. Huang, G. A. Somorjai, *Langmuir* **2010**, *26*, 16463-16468.
- [56] R. Xu, D. Wang, J. Zhang, Y. Li, *Chem. Asian J.* **2006**, *1*, 888-893.
- [57] J. Renzas, Y. Zhang, W. Huang, G. Somorjai, *Catal. Lett.* **2009**, *132*, 317-322.
- [58] E. van Steen, M. Claeys, *Chem. Eng. Technol.* **2008**, *31*, 655-666.
- [59] A. Y. Khodakov, W. Chu, P. Fongarland, *Chem. Rev.* **2007**, *107*, 1692-1744.
- [60] J. van de Loosdrecht, F. G. Botes, I. M. Ciobica, A. Ferreira, P. Gibson, D. J. Moodley, A. M. Saib, J. L. Visagie, C. J. Weststrate, J. W. Niemantsverdriet, *Comprehensive Inorganic Chemistry II, Vol. 7: Surface Inorganic Chemistry and Metal-Based Catalysis*, Elsevier, **2013**.
- [61] R. A. van Santen, I. M. Ciobica, E. van Steen, M. M. Ghouri, *Adv. Catal.* **2011**, *54*, 127-187.
- [62] R. A. van Santen, M. M. Ghouri, S. Shetty, E. J. M. Hensen, *Catal. Sci. Tech.* **2011**, *1*, 891-911.
- [63] M. Ojeda, R. Nabar, A. U. Nilekar, A. Ishikawa, M. Mavrikakis, E. Iglesia, *J. Catal.* **2010**, *272*, 287-297.
- [64] S. Shetty, A. P. J. Jansen, R. A. van Santen, *J. Am. Chem. Soc.* **2009**, *131*, 12874-12875.
- [65] R. C. Brady, R. Pettit, *J. Am. Chem. Soc.* **1981**, *103*, 1287-1289.
- [66] J. Gaube, H. F. Klein, *J. Mol. Catal. A: Chem.* **2008**, *283*, 60-68.
- [67] P. M. Maitlis, H. C. Long, R. Quyoum, M. L. Turner, Z.-Q. Wang, *Chem. Commun.* **1996**, 1-8.
- [68] H. Pichler, H. Schulz, *Chem. Ing. Tech.* **1970**, *42*, 1162-1174.
- [69] B. H. Davis, *Catal. Today* **2009**, *141*, 25-33.
- [70] M. Zhuo, K. F. Tan, A. Borgna, M. Saeys, *J. Phys. Chem. C* **2009**, *113*, 8357-8365.
- [71] C. J. Weststrate, H. J. Gericke, M. W. G. M. Verhoeven, I. M. Ciobică, A. M. Saib, J. W. Niemantsverdriet, *J. Phys. Chem. Lett.* **2010**, *1*, 1767-1770.
- [72] J. Schweicher, A. Bundhoo, A. Frennet, N. Kruse, H. Daly, F. C. Meunier, *J. Phys. Chem. C* **2010**, *114*, 2248-2255.
- [73] Q. Zhang, J. Kang, Y. Wang, *ChemCatChem* **2010**, *2*, 1030.
- [74] J. C. J. Bart, R. P. A. Sneed, *Catal. Today* **1987**, *2*, 1-124.
- [75] L. C. Grabow, M. Mavrikakis, *ACS Catal.* **2011**, *1*, 365-384.
- [76] G. Prieto, P. Concepcion, A. Martinez, E. Mendoz, *J. Catal.* **2011**, *280*, 274-288.
- [77] N. D. Subramanian, J. Gao, X. Mo, J. G. Goodwin, Jr., W. Torres, J. J. Spivey, *J. Catal.* **2010**, *272*, 204-209.

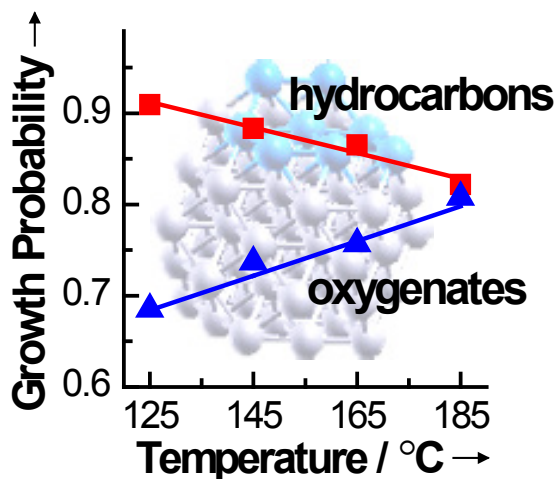
-
- [78] D. Mei, R. Rousseau, S. M. Kathmann, V.-A. Glezakou, M. H. Engelhard, W. Jiang, C. Wang, M. A. Gerber, J. F. White, D. J. Stevens, *J. Catal.* **2010**, *271*, 325-342.
- [79] M. A. Haider, M. R. Gogate, R. J. Davis, *J. Catal.* **2009**, *261*, 9-16.
- [80] N. Tien-Thao, M. H. Zahedi-Niaki, H. Alamdari, S. Kaliaguine, *J. Catal.* **2007**, *245*, 348-357.
- [81] H. Hamada, Y. Kuwahara, Y. Kintaichi, T. Ito, K. Wakabayashi, H. Iijima, K. Sano, *Chem. Lett.* **1984**, 1611-1612.
- [82] Y. Kintaichi, T. Ito, H. Hamada, H. Nagata, K. Wakabayashi, *J. Jpn. Pet. Inst.* **1998**, *41*, 66-70.
- [83] M. P. Andersson, E. Abild-Pedersen, I. N. Remediakis, T. Bligaard, G. Jones, J. Engbæk, O. Lytken, S. Hørch, J. H. Nielsen, J. Sehested, J. R. Rostrup-Nielsen, J. K. Nørskov, I. Chorkendorff, *J. Catal.* **2008**, *255*, 6-19.
- [84] G. Du, S. Lim, Y. Yang, C. Wang, L. Pfefferle, G. L. Haller, *J. Catal.* **2007**, *249*, 370-379.
- [85] J. J. Spivey, A. Egbeki, *Chem. Soc. Rev.* **2007**, *36*, 1514-1528.
- [86] J. Wang, P. A. Chernavskii, A. Y. Khodakov, Y. Wang, *J. Catal.* **2012**, *286*, 51-61.
- [87] Y.-T. Tsai, X. Mo, J. G. Goodwin Jr, *J. Catal.* **2012**, *285*, 242-250.
- [88] C. Wang, H. Zhao, H. Wang, L. Liu, C. Xiao, D. Ma, *Catal. Today* **2012**, *183*, 143-153.
- [89] X. B. Fan, Z. Y. Tao, C. X. Xiao, F. Liu, Y. Kou, *Green Chem.* **2010**, *12*, 795-797.
- [90] E. Durham, S. Zhang, C. Roberts, *Appl. Catal. A* **2010**, *386*, 65-73.
- [91] Y. G. Wang, B. H. Davis, *Appl. Catal. A* **1999**, *180*, 277-285.
- [92] E. Iglesia, S. L. Soled, R. A. Fiato, *J. Catal.* **1992**, *137*, 212-224.
- [93] O. Borg, P. D. C. Dietzel, A. I. Spjelkavik, E. Z. Tveten, J. C. Walmsley, S. Diplas, S. Eri, A. Holmen, E. Rytter, *J. Catal.* **2008**, *259*, 161-164.
- [94] G. Prieto, A. Martínez, P. Concepción, R. Moreno-Tost, *J. Catal.* **2009**, *266*, 129-144.
- [95] J. P. den Breejen, P. B. Radstake, G. L. Bezemer, J. H. Bitter, V. Froseth, A. Holmen, K. P. de Jong, *J. Am. Chem. Soc.* **2009**, *131*, 7197-7203.
- [96] A. Tuxen, S. Carencó, M. Chintapalli, C.-H. Chuang, C. Escudero, E. Pach, P. Jiang, F. Borondics, B. J. Beberwyck, A. P. Alivisatos, G. Thornton, W.-F. Pong, J. Guo, R. Perez, F. Besenbacher, M. Salmeron, *J. Am. Chem. Soc.* **2013**, *135*, 2273-2278.
- [97] D. I. Enache, B. Rebours, M. Roy-Auberger, R. Revel, *J. Catal.* **2002**, *205*, 346-353.
- [98] H. I. Karaca, O. V. Safonova, S. p. Chambrey, P. Fongarland, P. Roussel, A. Griboval-Constant, M. Lacroix, A. Y. Khodakov, *J. Catal.* **2011**, *277*, 14-26.

Chapter 2

Unprecedented Oxygenate Selectivity in Aqueous Phase Fischer-Tropsch Synthesis by Ruthenium Nanoparticles

Summary

An unprecedented 70% oxygenate selectivity in Fischer-Tropsch synthesis was achieved using a Ru nanoparticle catalyst in the aqueous phase. A kinetic analysis of the anomalous temperature dependence of the chain growth probability shows that hydrocarbons and oxygenates are formed on different sites. Oxygenates (hydrocarbons) form on sites with high (low) barrier for CO dissociation.



2.1 Introduction

Global demand for clean fuel and rapid depletion of available oil reserves has led to renewed interest in Fischer-Tropsch synthesis (FTS). In FTS, syngas (a mixture of CO and H₂) is converted into clean transportation fuels. Syngas can be obtained from fossil resources such as natural gas via steam reforming or from coal and biorenewable resources via gasification. Several group VIII metals (Co, Fe, Ru, Rh) are useful Fischer-Tropsch catalysts [1-2]. FTS occurs via polymerization of CH_x building blocks generated from syngas by CO dissociation followed by C hydrogenation. The product composition can be described by the Anderson–Schulz–Flory distribution [3]. Besides paraffins ranging from LPG to waxes [4-6], FTS also produces relatively small amounts of oxygenates such as alcohols, acids, esters, ketones and aldehydes [7]. Tuning the selectivity of FTS to oxygenates would provide an alternative source of these important intermediate chemicals [8]. Commercially, FTS is carried out in the gas or slurry phase. Recently, Xiao et al. showed that FTS can be carried out in the aqueous phase[9]. These authors found gasoline-range hydrocarbons with a Ru nanoparticle catalyst. Subsequent studies reported predominantly hydrocarbons and a maximum of 25% oxygenates for liquid phase FTS with Co [10-11] and Fe [11] colloids. In industry, Fe and Co are the preferred FTS catalysts because of cost reasons [2, 12-13]. Ru is the most active FTS catalyst and typically produces high molecular weight hydrocarbons without promoters [14-15]. Its activity strongly depends on the particle size [9, 16-20].

Herein we show that Ru nanoparticle catalysts dispersed in water convert syngas at low reaction temperatures with high selectivity into a mixture of oxygenates in the C₅-C₁₀ range. An unprecedented aldehyde selectivity up to 70 % is obtained for 2.2 nm Ru nanoparticles at 125 °C. The selectivity strongly depends on the reaction temperature. An anomalous chain growth behavior of oxygenates (increasing chain growth probability α with temperature) is reported, which is discussed in terms of the competition between CO dissociation and chain termination. The present data provide strong indications that oxygenates and hydrocarbons are formed on different reaction sites of the Ru nanoparticles.

2.2 Experimental Methods

2.2.1 Synthesis of Materials

Ru nanoparticles reduced by NaBH₄ (Ru-NaBH₄)

Ru nanoparticles were synthesized according to a previous published procedure [9]. In a typical synthesis, RuCl₃.nH₂O (11 mg, 46.5 μ mol) and PVP (31 mg, M_n = 58 000, molar

ratio PVP/Ru = 6) were dissolved in distilled water (3 mL). NaBH₄ (9 mg) dissolved in water (330 μ l) was added to the mixture under vigorous stirring at ambient conditions. The mixture was allowed to stir for another 5 min and the resultant black solution containing Ru nanoparticles was then used for reactions.

Ru nanoparticles reduced by ethylene glycol (Ru-EG)

RuCl₃.nH₂O (11 mg, 46.5 μ mol) and PVP (31 mg, M_n = 58 000, molar ratio PVP/Ru = 6) were dissolved in distilled water (1 mL) and ethylene glycol (4 mL). The mixture was then added drop wise to ethylene glycol (15 mL) preheated to 145 °C and refluxed under N₂ flow for 3 h. The resultant black mixture was washed with a mixture of acetone and diethyl ether and collected by centrifugation. The isolated Ru nanoparticles were then re-dispersed in distilled water (3.33 mL).

Ru nanoparticles reduced by NaBH₄ and H₂ (Ru-NaBH₄+H₂)

Ru nanoparticles (46.5 μ mol, Ru-NaBH₄) dispersed in water (3.33 mL) was added to the stainless steel autoclave. The autoclave was then pressurized to 20 bar with H₂, and the solution was reduced at 145°C for 3 h under vigorous stirring. The reaction was stopped by immersing the autoclave into an ice bath.

Ru nanoparticles re-oxidized by O₂ (Ru- O₂-65 / Ru- O₂-145)

Ru nanoparticles (46.5 μ mol, Ru-NaBH₄+H₂) dispersed in water (3.33 mL) was added to the stainless steel autoclave. The autoclave was then pressurized with O₂ and N₂ to 10 bar (O₂/N₂ = 1). The solution was then re-oxidized at 65°C or 145°C for 1 h under vigorous stirring. The reaction was stopped by immersing the autoclave into an ice bath.

2.2.2 Characterization

Transmission electron microscopy (TEM) was performed on FEI Tecnai 20 electron microscope at an acceleration voltage of 200 kV with a LaB6 filament. A small amount of the sample was mixed with ethanol, dispersed and dried over a carbon-coated Cu grid. Average particle size was calculated by measuring more than 120 particles.

CO adsorption Fourier-Transform Infrared (FTIR) spectroscopy was collected using a Nicolet Avatar 360 FTIR in transmittance mode. The isolate Ru nanoparticles were first dissolved in ethanol (100 μ l) and CH₂Cl₂ (3 mL) in a stainless steel autoclave. The autoclave

was flush with CO for three times before pressurizing to 10 bar. After stirring for 30 min at room temperature, the CO was vent and the colloidal solution was transfer to a KBr liquid cell (25×4 mm). The CO adsorption FTIR spectra then collected.

The X-ray photoelectron spectrometer (XPS) samples were prepared by drying the dispersed Ru nanoparticles on a silica wafer before introducing into a Kratos AXIS Ultra spectrometer equipped with a monochromatic Al K α X-ray source and a delay-line detector. Spectra were obtained using the aluminum anode (Al K α = 1486.6 eV) operating at 150 W. For survey and region scans, constant pass energies of 160 eV and 40 eV, respectively, were used. The background pressure was 2×10^{-9} mbar. Fitting was carried out with the CasaXPS program.

X-ray absorption spectroscopy (XAS) spectra were recorded in a home-built transmission cell for liquid samples. The liquid was placed between Kapton windows. In a typical experiment, 200 μ L of 140 μ mol Ru/mL H₂O of sample was transferred into the XAS cell. XAS spectra were collected in fluorescence mode at the Ru K edges at the Dutch Belgium Beamline (DUBBLE) of the European Synchrotron Radiation Facility (ESRF, Grenoble, France).

2.2.3 Catalytic Activity Measurements

Aqueous phase Fischer Tropsch synthesis (FTS) was carried out at 30 bar for 24 h in a 10 mL stainless steel autoclave. Ru nanoparticles (46.5 μ mol) dispersed in water (3.33 mL) was added to the autoclave. The autoclave was then flushed with CO for 3 times, before being pressurized with CO followed by H₂ to 30 bar (molar ratio H₂/CO = 2). The autoclave was sealed and the reaction was initiated by immersing the autoclave into an oil bath maintained at the reaction temperature. The reaction was terminated after 24 h by immersing the autoclave into an ice bath.

Heptanal hydrogenation was carried out at 30 bar for 24 h in a 10 mL stainless steel autoclave. Ru nanoparticles (46.5 μ mol) dispersed in water (3.33 mL) were added to the autoclave. The autoclave was then flushed with CO for 3 times, before being pressurized with CO followed by H₂ to 30 bar (molar ratio H₂/CO = 2), where it was stirred at ambient temperature for 0.5 h. The pressure was released and heptanal (71 μ mol) was added to the autoclave prior to flushing and re-pressurizing to 30 bar with syngas (molar ratio H₂/CO = 2). The autoclave was sealed and the reaction was initiated by immersing the autoclave into an

oil bath maintained at the reaction temperature. The reaction was terminated after 24 h by immersing the autoclave into an ice bath.

Gaseous products were analyzed with an Interscience Compact GC system, equipped with a Molsieve 5Å and Porabond Q column each with a thermal conductivity detector (TCD), and a Al₂O₃/KCl column with a flame ionization detector (FID). The outlet of the autoclave was connected to a mass flow controller and feed into the GC to analyze the gaseous products. The identification and quantification of gaseous products were done by using a gas cylinder containing known quantity of CH₄ and butane.

The liquid products were first extracted with diethyl ether containing *p*-cymene as an internal standard. The organic phase containing the FTS products was then analyzed by gas chromatograph-mass spectrometry (GC-MS, QP5050, Shimadzu) equipped with a CP-Sil 8CB capillary column (30 m × 0.32 mm, film thickness 0.5 μm) and/or gas chromatograph (GC, GC-17A, Shimadzu) equipped with a Rxi-5ms capillary column (30 m × 0.25 mm, film thickness 0.5 μm) and FID. Identification of linear alkanes (C₇ to C₁₉), alcohols (C₄ to C₁₂) and aldehydes (C₄ to C₁₂) were established by GC-MS and the retention time of authenticate samples. Quantitative analysis of the liquid products was established by using authenticate samples and *p*-cymene as the internal standard.

The turnover frequency (TOF) and selectivity was calculated based on the number of moles of carbon being formed as products according to the following formula:

$$\text{TOF} = \frac{\text{total mol C formed as products}}{(\text{mol Ru}_{\text{surface}}) \times \text{reaction time}}$$

$$\text{Selectivity to hydrocarbon or oxygenate} = \frac{\sum (\text{mol of C}_n^{\text{HC/oxy}} \times n)}{\text{total mol C formed as products}}$$

with the number of mol Ru_{surface} = mol Ru × D and D being the dispersion.

The dispersion (D) was calculated assuming spherical shapes and using the formula described by Scholten et al. [21]:

$$D = 10^{21} \times \frac{6 \times M \times \rho_{\text{site}}}{dp \times N \times \rho_{\text{metal}}}$$

with M being the atomic weight of Ru, ρ_{site} the surface density (16.3 Ru atom/nm²), ρ_{metal} the density of metal (12.3 g/cm³), N_{Av} Avogadro's number [22].

2.3 Results and Discussion

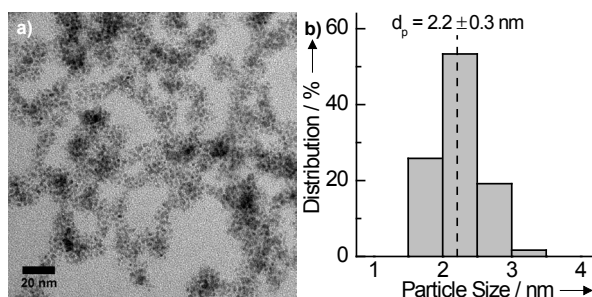


Figure 2.1: Ru nanoparticles reduced by NaBH_4 (a) electron micrograph, and (b) particle size distribution.

Ru nanoparticles encapsulated in Polyvinylpyrrolidone (PVP) with an average size of 2.2 ± 0.3 nm (Figure 2.1) were prepared by reducing $\text{RuCl}_3 \cdot n\text{H}_2\text{O}$ with NaBH_4 in water (PVP/Ru ratio = 6). The catalytic performance of these nanoparticles was investigated in the aqueous phase at a total pressure of 30 bar synthesis gas (H_2/CO ratio = 2) as a function of the reaction temperature. The turnover frequency (TOF) increases with the reaction temperature (Figure 2.2). The CO conversion is 0.7 % at 125 °C and 12.8 % at 185 °C (Figure 2.3). The TOF of 0.55 h^{-1} at 185 °C is similar to values ($0.3\text{--}1.2 \text{ h}^{-1}$) reported for a supported Ru catalyst in a slurry phase reactor at 200°C (Figure 2.3 insert) [23]. The product distribution strongly depends on temperature and is at strong variance with results of earlier work [9]. The aldehyde selectivity of ~70% at 125°C is exceptionally high. The alcohol/aldehyde ratio increases with temperature. Concomitantly, the total alkane/alkene selectivity increases at the expense of the oxygenate selectivity. The methane selectivity (<15 %) compares favorably to a supported Rh catalyst for alcohols synthesis used at 230 °C [24]. A separate experiment was performed with heptanal as co-reactant in the Fischer-Tropsch reaction. The only significant change in the product distribution was the formation of heptanol, indicating that the aldehyde is not involved in further chain growth nor in cracking reactions. At a temperature of 185 °C the oxygenate selectivity is ~30 %. The selectivity to olefins is negligible at 125°C and amounts to 15 % at 185°C. The selectivity to hydrocarbons and oxygenates is a weak function of the conversion (Figure 2.4).

The observation of aldehydes and alcohols as the dominant products in Fischer-Tropsch synthesis is new. Lower alcohols up to octanol have been reported for several catalysts such as supported Rh metal and CoMo sulfides [24-27]. For instance, Goodwin and co-workers obtained an oxygenate selectivity of 25 %, mainly methanol and ethanol, using Rh/SiO₂ at 230°C [26]. The strong dependence of the product composition on the reaction temperature for aqueous phase FTS as reported here points to a change in the dominant

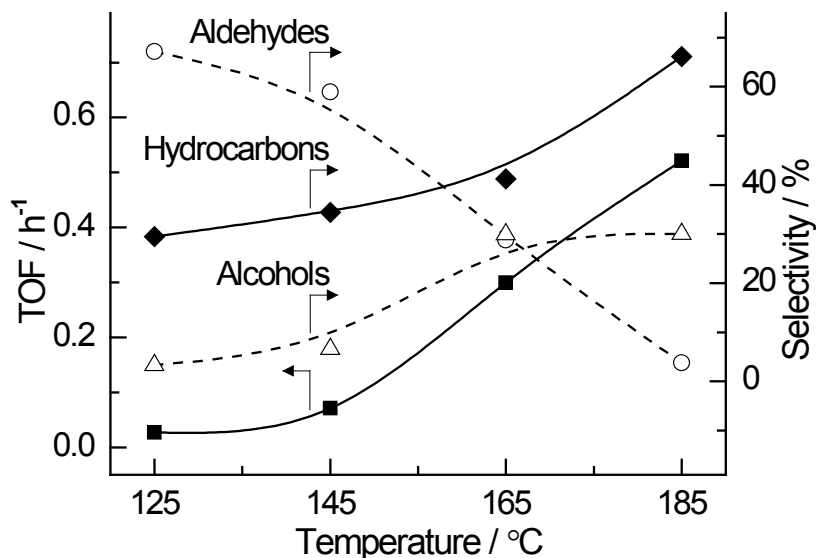


Figure 2.2: Ru catalysed aqueous phase FTS activity and product distribution.

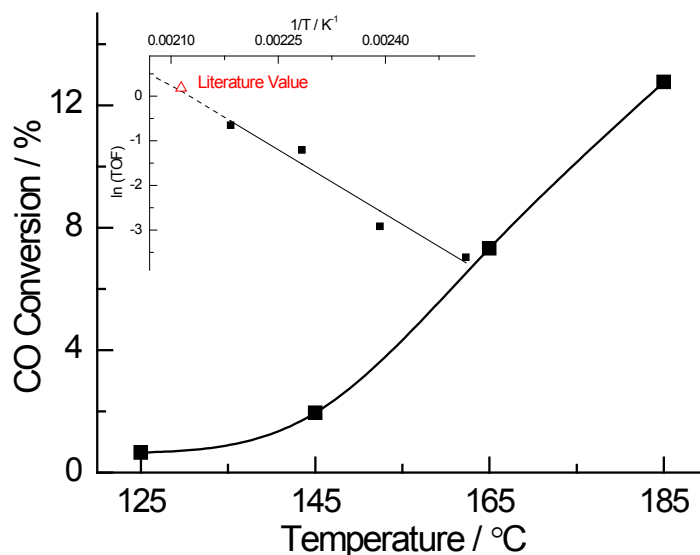


Figure 2.3: CO conversion for aqueous FTS catalyzed by Ru-NaBH₄ as a function of temperature, and insert Arrhenius plot (■ represents experimental data, △ represents literature data [23]).

mechanism of chain termination. Proposals for chain termination in FTS include H addition to the alkyl chain (alkane), β -H-elimination of the alkyl chain (olefin) and CO insertion into the alkyl chain (aldehyde). The predominant formation of oxygenates points to CO insertion as the main mechanism of termination at low reaction temperatures. A straightforward explanation for this difference is the higher surface coverage with CO at lower temperature combined with a relatively low rate of CO dissociation. An increase of the oxygenate selectivity with decreasing temperature has been reported before [28]. The average observed chain length is in the C₅ to C₁₀ range for all investigated temperatures (Figure 2.5) and the composition of the product mixture follows the Anderson-Schulz-Flory (ASF) distribution

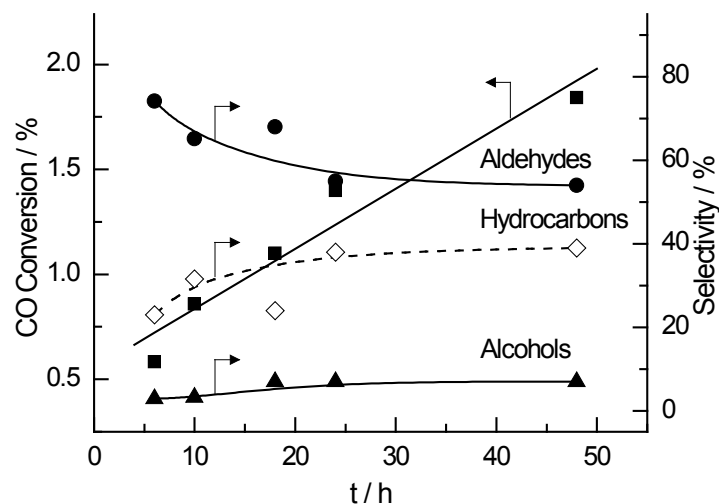


Figure 2.4: Time dependent study of FTS performed using Ru-NaBH₄ catalyst.

(Figure 2.6). As typically reported for FTS by Ru, Co and Fe [3, 19, 29-30], the chain growth probability α for hydrocarbons (α_{HC}) decreases with temperature (Figure 2.5d, Figure 2.6). A very peculiar observation is the increase of the molecular weight of the oxygenate products and thus α for oxygenates (α_{oxy}) with temperature. The chain lengths of the aldehyde and alcohol products are very similar with a slightly higher contribution of longer alcohols. This result suggest that hydrocarbons and oxygenates are formed on different active sites.

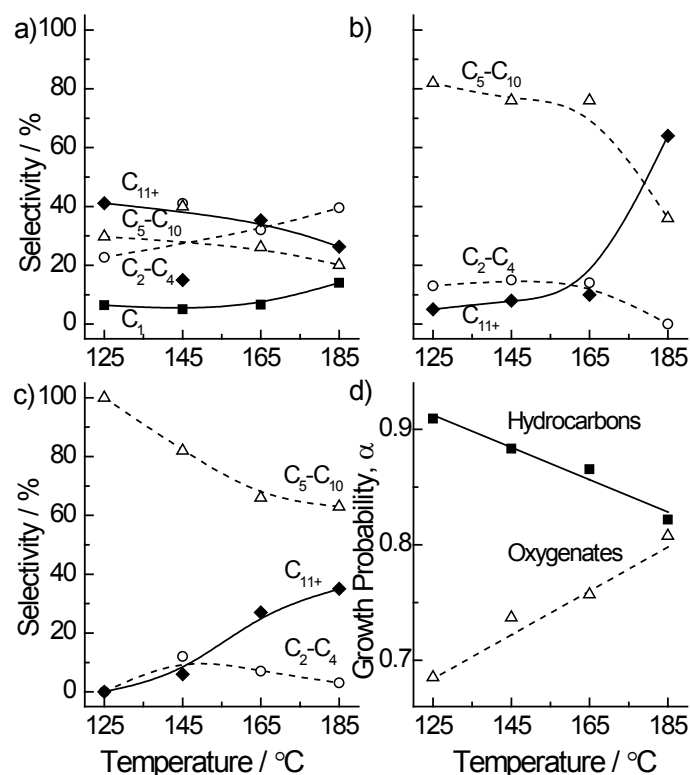


Figure 2.5: Product distribution during FTS of Ru nanoparticles for (a) hydrocarbons (b) aldehydes (c) alcohols and (d) chain growth probability of hydrocarbons and oxygenates as a function of temperature.

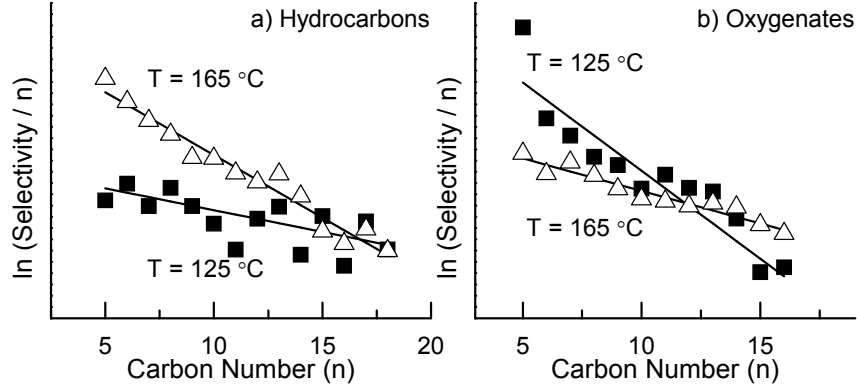


Figure 2.6: Anderson-Schulz-Flory distribution plot for aqueous phase FTS at 125°C and 165°C for (a) hydrocarbons and (b) oxygenates.

For the Fischer-Tropsch reaction, a kinetic interpretation can be given that, in order to maintain a high rate of chain growth, the rate of chain termination has to be slow and that of C-C coupling fast [31]. Within the generally accepted carbene chain growth mechanism involving CH_x building blocks [32-39] this implies that the rates of CO dissociation and CH_x formation have to be fast compared to the rate of chain termination (termination would be rate limiting). Since termination has the highest activation energy, increasing temperature would result in greatest increase the rate of termination leading to decrease in chain growth probability, as observed here for the hydrocarbon products of aqueous phase FTS (α_{HC}). On the contrary, α_{oxy} becomes larger with increasing temperature. This anomalous temperature dependence suggests competition between chain termination by CO insertion and rate of CO dissociation. When CO dissociation is slow, the surface concentration of CH_x intermediates to be inserted into the growing hydrocarbon chain is low, which leads to a decreased rate of chain growth.

An explicit expression for α can be derived from the Schulz-Flory assumption of independence of chain growth rate and rate of termination from product chain length

$$\alpha(C_i) = \frac{r_{\text{propagation}}(C_i)}{r_{\text{propagation}}(C_i) + r_{\text{termination}}(C_{i-1})}; i \geq 2 \quad (2.1)$$

where $r_{\text{propagation}}(C_i)$ is the rate of propagation of a hydrocarbon chain C_{i-1} with chain length $i - 1$ to a hydrocarbon chain C_i with chain length i , $r_{\text{termination}}(C_{i-1})$ the rate of termination of a hydrocarbon chain with length $i - 1$.

Since rate of propagation depends on the surface coverage of CH_x species, $\theta(\text{CH}_x)$, α can be rewritten as:

$$\alpha(C_i) = \frac{r_{prop.}(C_i) \cdot \theta(CH_X)}{r_{prop.}(C_i) \cdot \theta(CH_X) + r_{term.}(C_{i-1})} \quad (2.2)$$

By assuming that (i) O removal on the surface is fast, and (ii) hydrogenation steps are implicit (e.g., C hydrogenation to CH_x) and assumed to be fast. The expression for the steady state CH_x coverage on the surface of the catalyst is defined as:

$$\frac{d}{dt}\theta(CH_X) = r_{CO \text{ dissociation}} - r_{methanation} - \sum_{i \geq 2} r_{propagation}(C_i) \quad (2.3)$$

in which the terms on the right hand side reflect the rates of CO dissociation, methanation (CH_x hydrogenation) and propagations by C-C coupling of CH_x to all growing hydrocarbon chains C_{i-1} forming C_i , respectively.

$$0 = k_{CO \text{ diss.}} \cdot \theta(CO) \cdot \theta_{vacant} - r'_{meth.} \cdot \theta(CH_X) - \sum_{i \geq 2} r'_{prop.}(C_i) \cdot \theta(C_{i-1}) \cdot \theta(CH_X)$$

where $\theta_{vacant} = 1 - \theta(CO) - \theta(CH_X) - \sum_{i \geq 2} \theta(C_i)$

Hence

$$\theta(CH_X) = \frac{k_{CO \text{ diss.}} \cdot \theta(CO) \cdot (1 - \theta(CO) - \sum_{i \geq 2} \theta(C_i))}{k_{CO \text{ diss.}} \cdot \theta(CO) + \sum_{i \geq 2} r'_{prop.}(C_i) \cdot \theta(C_{i-1}) + r'_{meth.}} \quad (2.4)$$

Since the number of growing chain on the surface is expected to be low [40], we can assume that $\sum_{i \geq 2} \theta(C_i) \approx 0$. Hence steady state expression for $\theta(CH_X)$ can be written as:

$$\theta(CH_X) = \frac{k_{CO \text{ diss.}} \cdot \theta(CO) \cdot (1 - \theta(CO))}{k_{CO \text{ diss.}} \cdot \theta(CO) + \sum_{i \geq 2} r'_{prop.}(C_i) \cdot \theta(C_{i-1}) + r'_{meth.}} \quad (2.5)$$

By substituting $\theta(CH_X)$ into $\alpha(C_i)$, the chain growth probability, α , can then be described by the following equation:

$$\alpha = \frac{1}{1 + \frac{r_{term.}(C_{i-1})}{r_{prop.}(C_i)} \cdot \frac{1 + \kappa}{1 - \theta(CO)}} \quad (2.6)$$

The term containing κ explicitly depends on the coverage with CH_x building blocks via

$$\kappa = \frac{\sum_{i > 1} r_{prop.}(C_i) \cdot \theta(C_{i-1}) + r_{meth.}}{k_{CO \text{ diss.}} \cdot \theta(CO)} \quad (2.7)$$

κ depends on the rates of CO dissociation, chain growth and chain growth termination. Only when the rate of CO dissociation is very fast ($\kappa \rightarrow 0$ and $\theta(\text{CO}) \rightarrow 0$) as is conventionally assumed, α is found to be independent of the rate of CO dissociation. The condition of slow chain termination implies that the activation energy of this step is higher than that of chain growth and accordingly predicts a decrease of α with increasing temperature.

The rate of CO dissociation is strongly dependent on temperature, the surface topology and the CO coverage [41-42]. At low temperature, the CO coverage will be high and the rate of CO dissociation will become inhibited because of site blocking. In this case CO dissociation competes with chain termination and κ does not equal zero. With increasing temperatures CO will desorb, which creates vacancies. Hence, the apparent activation energy for CO dissociation will decrease with temperature. As long as with increasing temperature the rate of CO dissociation increases faster than the chain termination rate the relative rate of chain growth will increase. This implies an increase in the chain growth probability.

Table 2.1. FTS Performance of Different Ru nanoparticles. ^[a]							
Catalyst	d_p (%)	Ru^0 (%)	TOF ^[b] (h^{-1})	$X^{[c]}$ (%)	Selectivity ^[d] (%)		
					HC	RCHO	ROH
Ru-NaBH ₄	2.2	74 ^[e]	0.05	1.4	34	59	7
		50 ^[f]					
Ru-NaBH ₄ +H ₂	3.0	84 ^[e]	0.19	3.3	35	57	8
Ru-EG	2.1	60 ^[f]	0.09	2.3	40	45	15
Ru-O ₂ -65 ^[g]	3.3	75 ^[e]	0.10	1.6	25	66	9
Ru-O ₂ -145 ^[g]	3.2	46 ^[e]	0.03	0.5	31	64	5
[a] Reaction conditions: Ru nanoparticles (46.5 μmol), H ₂ O (3.33 mL), $P = 30$ bar (H_2/CO molar ratio = 2), $T = 145^\circ\text{C}$, $t = 24$ h. [b] mol CO (mol $\text{Ru}_{\text{surface}}^{-1}$) h^{-1} . [c] Conversion. [d] HC: paraffins and olefins, RCHO: aldehydes, ROH: alcohols. [e] XPS. [f] XANES. [g] Suffix indicates oxidation temperature in $^\circ\text{C}$.							

The dominance of oxygenates in the product pool at low temperature indicates that the rate of chain growth termination by CO insertion is fast compared to that of hydrocarbon formation. The increased rate of CO dissociation and decrease of CO coverage with temperature will shift the ratio of the rate of CO insertion chain termination versus that of termination to hydrocarbon formation. This will decrease the relative rate of oxygenate formation versus that of hydrocarbon formation with temperature in agreement with experimental observation. The observed slow rate of chain termination leading to

hydrocarbons at low temperature agrees with conventional temperature dependence of the α_{HC} . The rate of CO dissociation at low temperature is now always fast compared to the relatively slow rate termination. With increasing temperature the rate of chain termination to hydrocarbons increases faster than that of CO dissociation with a resulting decrease of α_{HC} .

According to the conventional view oxygenate and hydrocarbon formations are formed from the same intermediate growing hydrocarbon chains. The observation of very different kinetics for these two product classes in the present work implies that oxygenates and hydrocarbons are produced on different reaction sites. The structure sensitivity of CO dissociation is well understood [36-38]. Step-edge sites dissociate CO with a barrier less than 100 kJ/mol. On dense surfaces this barrier can be as high as 200 kJ/mol. Low barriers for CO dissociation will favour hydrocarbon formation, because the CO coverage is low and dissociation competes favourably with termination. Sites with a higher barrier for CO dissociation are candidates for termination by CO insertion, because of high CO coverage and competition of CO dissociation with termination. The anomalous chain growth parameter temperature is also consistent with a high barrier for CO dissociation. On such sites hydrogen assisted CO dissociation is the preferred pathway [36, 43].

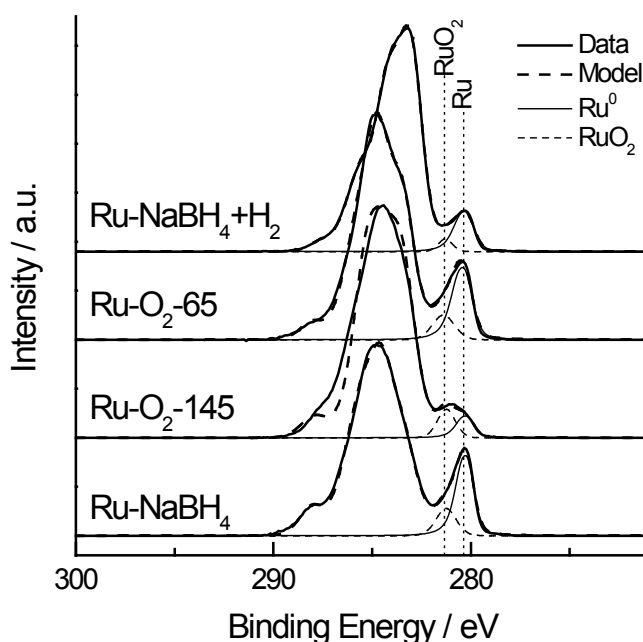


Figure 2.7: XP spectra in Ru 3d + C 1s region for re-oxidized Ru nanoparticles.

The FTS reaction requires metallic sites for CO dissociation and subsequent coupling reactions. The Ru^0 content of Ru nanoparticles reduced by NaBH_4 (Ru-NaBH_4) was found to be 74% by X-ray photoelectron spectroscopy (Figure 2.7, Table 2.1). When this catalyst was reduced in 20 bar H_2 at 145°C prior to reaction ($\text{Ru-NaBH}_4+\text{H}_2$), the catalyst was more active

but the product composition was similar. The higher activity may be due to the somewhat greater size of the particles (Figure 2.8) [20], but also because the surface became better reduced as evidenced by FTIR of adsorbed CO. The CO adsorption FTIR spectra in Figure 2.9 show a broad and strong band in the 1900-2036 cm^{-1} region and two bands at 2055 and 2125 cm^{-1} . The bands at 2010 cm^{-1} and 2125 cm^{-1} are absent for Ru-NaBH₄+H₂. The Ru-NaBH₄ spectrum exhibits an additional band at 2155 cm^{-1} . The assignment of the CO adsorption spectra follows Chin et al. [44]: bridge bonded CO at around 1950-2000 cm^{-1} , CO bonded to Ru⁰ surrounded by Ruⁿ⁺ at 2010 cm^{-1} , CO linearly bonded to Ru⁰ around 2025-2062 cm^{-1} and CO bonded to Ruⁿ⁺ around 2130-2155 cm^{-1} . Ru-NaBH₄+H₂ is considered to be more reduced than Ru-NaBH₄ due to the absence of peak at 2125 and 2155 cm^{-1} , assigned CO bonded to Ruⁿ⁺. TEM analysis of spent Ru-NaBH₄ indicated that the initially 2.2 nm particles had grown under reaction conditions to about 2.9 nm (Figure 2.10), which is quite similar to the size obtained after additional reduction of Ru-NaBH₄ in H₂.

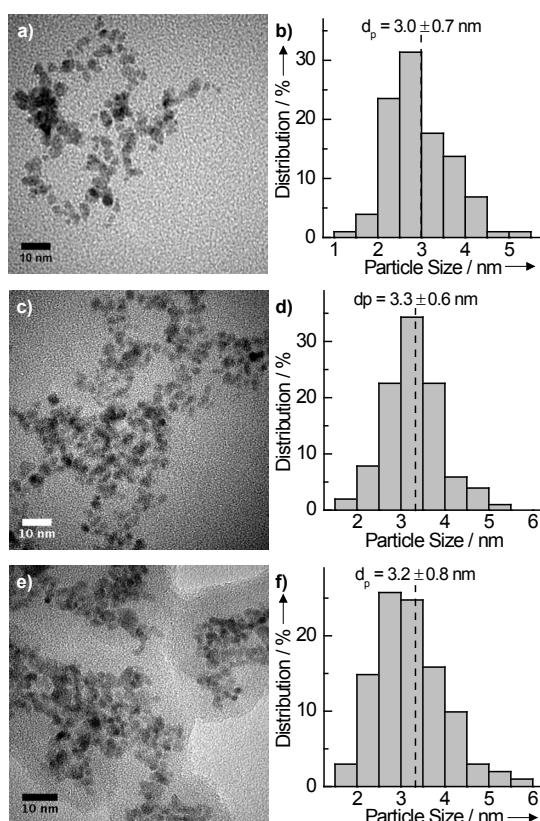


Figure 2.8: PVP stabilized Ru nanoparticles reduced by (a, b) NaBH₄ followed by H₂, and subsequently re-oxidized at (c, d) 65°C and (e, f) 145°C: (a, c, e) electron micrograph, (b, d, f) particle size distribution.

To further investigate the effect oxidation on activity and selectivity on aqueous phase FTS, the Ru-NaBH₄+H₂ catalyst were oxidized in O₂ at 65°C and 145°C. This result in the decrease of Ru⁰ content (Table 2.1: Ru-O₂-65 and Ru-O₂-145, TEM: Figure 2.8) and the

oxidation of the catalyst surface. Expectedly, the FTS activity decreased with the lower Ru^0 content, but with only minor effects on the product selectivity.

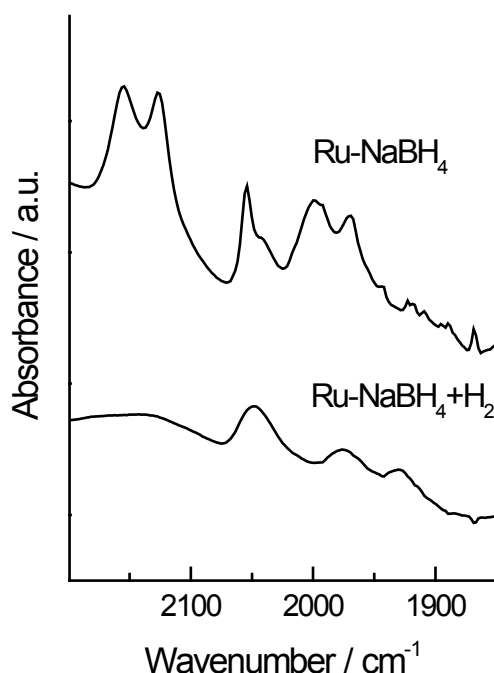


Figure 2.9: PVP stabilized Ru nanoparticles reduced by (a, b) NaBH_4 followed by H_2 , and subsequently re-oxidized at (c, d) 65°C and (e, f) 145°C : (a, c, e) electron micrograph, (b, d, f) particle size distribution.

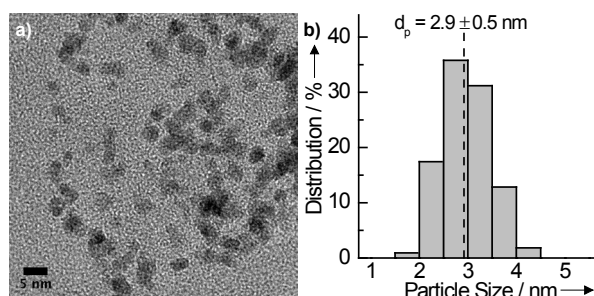


Figure 2.10: Ru-NaBH_4 after 24 h reaction (a) electron micrograph, (b) particle size distribution.

Both Na and B are known to affect the selectivity in FTS [45]. XPS survey scan for Ru-NaBH_4 shows that both Na and B are present. To exclude any promotion effect, Ru nanoparticles were prepared by reduction with ethylene glycol (Ru-EG , Table 2.1). The average particle size for Ru-EG was 2.1 ± 0.4 nm (Figure 2.11) which is comparable to the size of Ru-NaBH_4 . Higher FTS activity for Ru-EG than Ru-NaBH_4 could be due to higher Ru^0 content as determined by XANES (Table 2.1, Figure 2.12). However, only minor effect on the hydrocarbon and oxygenate selectivity was observed when catalyzed by Ru-EG and Ru-NaBH_4 . Hence, the promotion effect of Na and B is negligible on the product selectivity.

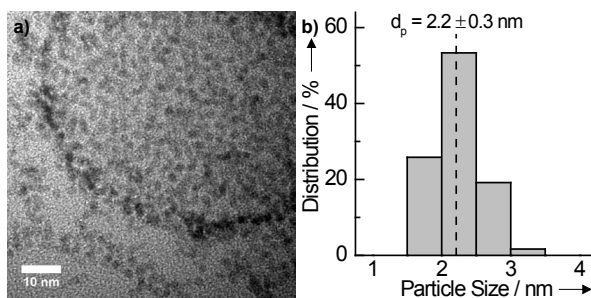


Figure 2.11: Ru nanoparticles reduced by ethylene glycol (a) electron micrograph, (b) particle size distribution.

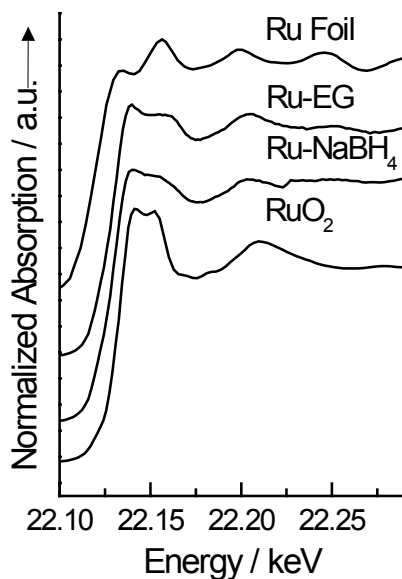


Figure 2.12: XANES spectra for Ru-NaBH₄ and Ru-EG.

2.4 Conclusion

In summary, we have shown that the total oxygenate selectivity in FTS can reach up to 70 % for Ru nanoparticles at low temperature with aldehydes as the dominant product. The reaction temperature strongly affects the relative rates of different termination mechanisms. The anomalous temperature dependence of α_{oxy} with temperature is consistent with the relatively high rate of CO insertion, a high CO coverage and the related high apparent activation energy of CO dissociation as compared to the activation energy of termination. An important corollary is that hydrocarbon formation and oxygenate formation must occur on different reaction sites of the Ru nanoparticles. Hydrocarbon formation occurs on sites with low barrier for CO dissociation. Candidate sites are the step-edge sites, whose stabilization requires larger particles [41-42]. We predict oxygenate formation on dense Ru surfaces. This is consistent with the observations of Hanaoka et al. [46], who observed for small Rh particles a steep decrease in the oxygenate yield with an increase of particle size. On larger

particles CO dissociation becomes possible because of the stabilization of step-edge sites leading to a higher rate of hydrocarbon formation.

References

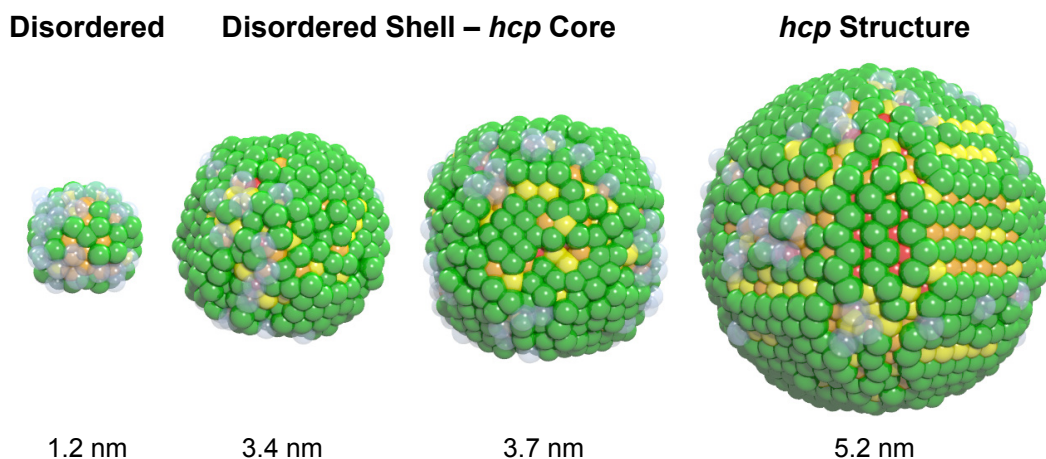
- [1] M. A. Vannice, *J. Catal.* **1975**, *37*, 449-461.
- [2] E. van Steen, M. Claeys, *Chem. Eng. Technol.* **2008**, *31*, 655-666.
- [3] G. P. Van der Laan, A. Beenackers, *Cat. Rev. Sci. Eng.* **1999**, *41*, 255-318.
- [4] Q. W. Zhang, X. H. Li, K. Asami, S. Asaoka, K. Fujimoto, *Catal. Today* **2005**, *104*, 30-36.
- [5] X. Dupain, R. A. Krul, C. J. Schaverien, M. Makkee, J. A. Moulijn, *Appl. Catal. B* **2006**, *63*, 277-295.
- [6] J. Kang, S. Zhang, Q. Zhang, Y. Wang, *Angew. Chem. Int. Ed.* **2009**, *48*, 2565-2568.
- [7] G. Henrici-Olivé, S. Olivé, *Angew. Chem. Int. Ed. Engl.* **1976**, *15*, 136-141.
- [8] K. G. Fang, D. B. Li, M. G. Lin, M. L. Xiang, W. Wei, Y. H. Sun, *Catal. Today* **2009**, *147*, 133-138.
- [9] C. X. Xiao, Z. P. Cai, T. Wang, Y. Kou, N. Yan, *Angew. Chem. Int. Ed.* **2008**, *47*, 746-749.
- [10] D. O. Silva, J. D. Scholten, M. A. Gelesky, S. R. Teixeira, A. C. B. Dos Santos, E. F. Souza-Aguiar, J. Dupont, *ChemSusChem* **2008**, *1*, 291-294.
- [11] X. B. Fan, Z. Y. Tao, C. X. Xiao, F. Liu, Y. Kou, *Green Chem.* **2010**, *12*, 795-797.
- [12] A. Y. Khodakov, W. Chu, P. Fongarland, *Chem. Rev.* **2007**, *107*, 1692-1744.
- [13] B. H. Davis, *Ind. Eng. Chem. Res.* **2007**, *46*, 8938-8945.
- [14] T. Komaya, A. T. Bell, Z. Wengsieh, R. Gronsky, F. Engelke, T. S. King, M. Pruski, *J. Catal.* **1994**, *150*, 400-406.
- [15] H. Schulz, *Appl. Catal. A* **1999**, *186*, 3-12.
- [16] C. S. Kellner, A. T. Bell, *J. Catal.* **1982**, *75*, 251-261.
- [17] E. Iglesia, S. L. Soled, R. A. Fiato, *J. Catal.* **1992**, *137*, 212-224.
- [18] H. H. Nijs, P. A. Jacobs, J. B. Uytterhoeven, *Chem. Commun.* **1979**, 1095-1096.
- [19] D. L. King, *J. Catal.* **1978**, *51*, 386-397.
- [20] G. L. Bezemer, J. H. Bitter, H. Kuipers, H. Oosterbeek, J. E. Holewijn, X. D. Xu, F. Kapteijn, A. J. van Dillen, K. P. de Jong, *J. Am. Chem. Soc.* **2006**, *128*, 3956-3964.
- [21] J. J. F. Scholten, A. P. Pijpers, A. M. L. Hustings, *Cat. Rev. Sci. Eng.* **1985**, *27*, 151-206.
- [22] A. J. Plomp, H. Vuori, A. O. I. Krause, K. P. de Jong, J. H. Bitter, *Appl. Catal. A* **2008**, *351*, 9-15.
- [23] M. Claeys, E. van Steen, *Catal. Today* **2002**, *71*, 419-427.
- [24] M. A. Haider, M. R. Gogate, R. J. Davis, *J. Catal.* **2009**, *261*, 9-16.
- [25] J. J. Spivey, A. Egbeki, *Chem. Soc. Rev.* **2007**, *36*, 1514-1528.
- [26] J. Gao, X. H. Mo, J. G. Goodwin, *J. Catal.* **2009**, *268*, 142-149.
- [27] A. Gotti, R. Prins, *J. Catal.* **1998**, *175*, 302-311.
- [28] G. V. d. Lee, V. Poncet, *Cat. Rev. Sci. Eng.* **1987**, *29*, 183 - 218.
- [29] T. J. Donnelly, C. N. Satterfield, *Appl. Catal.* **1989**, *52*, 93-114.
- [30] R. A. Dictor, A. T. Bell, *J. Catal.* **1986**, *97*, 121-136.
- [31] R. A. van Santen, I. M. Ciobica, E. van Steen, M. M. Ghouri, *Adv. Catal.* **2011**, *54*, 127-187.
- [32] A. Steynberg, M. Dry, *Fischer-Tropsch technology*, Elsevier, **2004**.
- [33] B. H. Davis, *Catal. Today* **2009**, *141*, 25-33.
- [34] I. M. Ciobica, G. J. Kramer, Q. Ge, M. Neurock, R. A. van Santen, *J. Catal.* **2002**, *212*, 136-144.
- [35] J. Cheng, P. Hu, P. Ellis, S. French, G. Kelly, C. Lok, *Top. Catal.* **2010**, *53*, 326-337.
- [36] I. M. Ciobica, R. A. van Santen, *J. Phys. Chem. B* **2003**, *107*, 3808-3812.
- [37] S. Shetty, A. P. J. Jansen, R. A. van Santen, *J. Am. Chem. Soc.* **2009**, *131*, 12874-12875.
- [38] S. Shetty, A. P. J. Jansen, R. A. van Santen, *J. Phys. Chem. C* **2008**, *112*, 14027-14033.
- [39] J. Cheng, P. Hu, P. Ellis, S. French, G. Kelly, C. M. Lok, *J. Phys. Chem. C* **2008**, *112*, 9464-9473.
- [40] R. A. van Santen, M. M. Ghouri, S. Shetty, E. J. M. Hensen, *Catal. Sci. Tech.* **2011**, *1*, 891-911.
- [41] R. A. van Santen, *Acc. Chem. Res.* **2009**, *42*, 57-66.
- [42] R. A. van Santen, M. Neurock, S. G. Shetty, *Chem. Rev.* **2010**, *110*, 2005-2048.
- [43] M. Ojeda, R. Nabar, A. U. Nilekar, A. Ishikawa, M. Mavrikakis, E. Iglesia, *J. Catal.* **2010**, *272*, 287-297.
- [44] S. Y. Chin, C. T. Williams, M. D. Amiridis, *J. Phys. Chem. B* **2006**, *110*, 871-882.
- [45] B. Chaudret, *C. R. Physique* **2005**, *6*, 117-131.
- [46] L. Liu, G. Sun, C. Wang, J. Yang, C. Xiao, H. Wang, D. Ma, Y. Kou, *Catal. Today* **2012**, *183*, 136-142.

Chapter 3

Structure Sensitivity in Ru Nanoparticles Catalyzed Fischer-Tropsch Synthesis: Catalyst Characterization

Summary

PVP-stabilized Ru nanoparticles between 1 to 5 nm were prepared by polyol reduction of Ru salts. The colloidal catalysts were characterized by transmission electron microscopy, FTIR of adsorbed CO, X-ray absorption spectroscopy and X-ray Diffraction combined with structural analysis. After a second reduction using high-pressure H₂ in an autoclave batch reactor, XANES shows that all catalysts were nearly completely reduced. The characterization data point to an increasing concentration of coordinatively unsaturated sites with decreasing particle size. The Ru-Ru distance of the first coordination shell obtained from XRD-PDF studies are similar to the Ru-Ru distance obtained from EXAFS. The XRD-PDF results indicate that the nanoparticles have a *hcp* structure. Their structural disorder increases with decreasing particle size. The complete structure of the nanoparticles was resolved by reversed Monte Carlo simulations of the XRD-PDF data. Comparison of the structures of differently sized nanoparticles shows a highly disordered surface structure, which is very different from the surfaces usually considered to simulate nanoparticles.



3.1 Introduction

A central focus in the study of catalytic reactions is to correlate the reactivity to a specific active site [1-6]. The presence of particular sites will strongly depend on the size of the metal particles. Structure sensitivity remains one of the most challenging topics to be understood in heterogeneous catalysis by metals.

Since Ertl and co-workers showed on single-crystal surfaces that step-edge sites are the active sites for NO dissociation [7], many studies have associated these sites with the active sites which govern catalytic reactivity. Despite their importance, identifying and quantifying step-edge sites on real nanoparticle catalysts remains a challenge. Step-edge sites consist of an ensemble of several surface metal atoms so that a surface step is created. These sites are very different from the edge, corner and terrace sites, which make up the surfaces of equilibrated metal nanoparticles. In recent years, attempts were made to correlate the catalytic reactivity to the number of step-edge sites on the catalyst. For instance, the activity for electro-oxidation of CO and methanol was correlated to the amount of step-edge sites determined by high resolution transmission electron microscopy (HRTEM) [5]. However, it is very difficult to identify step-edge sites by HRTEM because usually the resolution is not high enough. . This problem can be overcome by combining aberration-corrected scanning transmission electron microscopy (STEM) with discrete tomography [8]. Nevertheless, both methods probe only localized information and cannot analyze sufficient particles to make meaningful conclusion for real nanoparticle catalysts. Alternatively, a combination of characterization techniques can be applied to determine the number of step-edge sites, with an example being illustrated in the decomposition of NH_3 [6]. In this case, the metal nanoparticle was modeled using density functional theory (DFT) calculations in combination with experimental data from TEM, chemisorption and EXAFS. Typically, the models used for such calculations representing nanoparticle surfaces exhibit distinct crystal planes. Although inputs used to build the model particles were obtained from bulk techniques, DFT inherently assumes that the nanoparticles exhibit an ordered crystalline structure. Recent studies using high-energy X-ray diffraction (XRD) coupled with atomic Pair Distribution Function (PDF) analysis have shown that the 3D atomic arrangement of small metal nanoparticles deviates significantly from the ideal crystalline structure [9-11].

A central approach to determine the number of active sites on a catalyst, in particular step-edge sites, involves reconstructing the structure of the nanoparticles [6, 8]. In this study, Ru nanoparticles between 1 to 5 nm were prepared and characterized using TEM, CO

adsorption FTIR, XANES, EXAFS and XRD-PDF. Data obtained from XRD-PDF were evaluated with the information obtained from other characterization techniques. The 3D atomic structure of Ru particles was resolved by applying Reverse Monte Carlo (RMC) simulations to fit the XRD-PDF data. The properties of the Ru particles obtained will be used to explain activity and selectivity trends in the aqueous phase Fischer-Tropsch reactions in Chapter 4. The ultimate goal is to correlate change FT activity to the fraction of step-edge sites and shed light on the nature of active sites in the FT reaction.

3.2 Experimental Methods

3.2.1 Synthesis of Materials

Polyvinylpyrrolidone (PVP, $M_n = 10\,000$ g/mol, Sigma Aldrich) stabilized Ru nanoparticles were synthesized using 1,4-butanediol or H_2 as the reducing agent. Ruthenium(III) chloride hydrate ($RuCl_3 \cdot nH_2O$, Alfa Aesar) and ruthenium(III) acetylacetonate ($Ru(acac)_3$, Aldrich) were used as Ru precursors. The reduction by 1,4-butanediol was carried out in a similar manner as earlier described for Rh [12]. In a typical synthesis (PVP/Ru molar ratio of 20), 30 mg of $Ru(acac)_3$ and 0.17 g of PVP were dissolved in 2 mL of tetrahydrofuran (THF, Sigma Aldrich) and 3 mL of 1,4-butanediol (Sigma-Aldrich). The mixture was then added to 27 mL of 1,4-butanediol, which was preheated at 225 °C, followed by refluxing in a N_2 atmosphere for 2 h. The resulting black suspension was thoroughly washed with acetone and diethyl ether. After collecting the Ru nanoparticles by centrifugation, they were redispersed in 1.5 mL distilled water. In cases where reduction was carried out in hydrogen, first 40 mg of $RuCl_3 \cdot xH_2O$ and 0.22 g of PVP were dissolved in 1 mL of distilled water in a 10 mL autoclave. The autoclave was then pressurized with 20 bar H_2 followed by heating to 150 °C for 2 h under vigorous stirring. The resultant black suspension was washed, collected by centrifugation, and redispersed in 3 mL distilled water. Catalysts are denoted by Ru- x where x stands for the average particle size in nm.

3.2.2 Characterization

The concentration of the Ru nanoparticles was determined by inductively coupled plasma (ICP) analysis performed on a Goffin Meyvis SpectroCirus apparatus.

Transmission electron micrographs (TEM) were made with a FEI Tecnai 20 electron microscope equipped with a LaB6 filament and operating at an acceleration voltage of 200 kV. A small amount of the nanoparticles was mixed with ethanol, dispersed over a carbon-

coated Cu grid and finally dried in air. The average particle size and the standard deviation were determined by analysing at least 150 particles.

FTIR spectra of adsorbed CO were collected using a heated attenuated total reflectance (HATR) flow cell from Spectra-Tech ARK with a Si 45° crystal (cut-off at 1500 cm^{-1}) in a Nicolet Protégé 460 FTIR spectrometer equipped with a liquid-nitrogen cooled MCT detector. Prior to the IR measurement, the Ru nanoparticles dispersed in water were re-reduced in an autoclave at 150 °C with 20 bar H_2 for 2 h under vigorous stirring. The Ru particles were then spin-coated onto the Si crystal under N_2 atmosphere. The coated Si crystal was then mounted and sealed in the ATR cell under N_2 atmosphere. The sample was dried by flowing 5 mL/min of He at 80 °C for 30 min. Subsequently, CO was introduced in the cell at a flow of 2.5 mL/min. After an isothermal period at 50 °C for 0.5 h, the cell was heated to 150 °C. FTIR spectra were recorded 5 min after reaching 150 °C in absorbance mode at a resolution of 4 cm^{-1} . A total of 32 scans were measured in this way, followed by subtraction of the background spectrum of the Si crystal.

X-ray Absorption Spectra (XAS) were recorded in a home-built transmission cell for liquid samples at the Dutch Belgium Beamline (DUBBLE) of the European Synchrotron Radiation Facility (ESRF, Grenoble, France). A droplet of the liquid containing the Ru nanoparticles was placed between Kapton windows. XAS spectra were collected in fluorescence mode at the Ru K edges with a 9-channel solid-state detector. Energy selection was done by a double crystal Si(111) monochromator. EXAFS analysis was performed with EXCURVE931 on k^3 -weighted unfiltered raw data using the curved wave theory. Phase shifts were derived from ab initio calculations using Hedin-Lundqvist exchange potentials and Von Barth ground states as implemented in EXCUREVE98. In a typical experiment, 200 μL of 140 $\mu\text{mol Ru/mL H}_2\text{O}$ of sample was transferred into the XAS cell. The cells were then transferred to the beamline and the EXAFS spectra were recorded at room temperature.

High-energy X-ray diffraction (XRD) experiments were performed at the 11-ID--B beamline (Advanced Photon Source, Argonne National Laboratory) using X-rays of energy of 90.48 keV ($\lambda = 0.1372 \text{ \AA}$) [10]. Prior to the measurements, the Ru nanoparticles dispersed in water were re-reduced at 150 °C with 20 bar H_2 for 2 h in an autoclave under vigorous stirring. After reduction, the PVP-stabilized Ru particles were loaded on to carbon nanofibers by impregnation and dried overnight at 100 °C. The supported Ru particles were then loaded into a capillary column and measured at room temperature. Bulk Ru (from Alfa Aesar; 99.9% purity; crystallite grain size of $\sim 1000 \text{ nm}$) was used as the reference material. The processing

of XRD data and derivation of $G(r)$ values was performed using the RAD program [13]. The model PDF was generated using the PDFFIT program [14]. Reverse Monte Carlo (RMC) simulations was performed using the RMC++ program [15].

3.3 Results and Discussion

Table 3.1 summarizes the conditions used to synthesize Ru nanoparticles. The reduction method, reduction temperature and the Ru source were varied to control the size of Ru nanoparticles between 1.2 to 5.2 nm (Figure 3.1). In a standard synthesis using polyol reduction of RuCl_3 at 195 °C for 2 h, we obtained on average 2.3 nm Ru particles (Ru-2.3). By using $\text{Ru}(\text{acac})_3$ instead of RuCl_3 under otherwise similar conditions we obtained larger particles (Ru-3.7), suggesting that the ligand is important in determining the particle size. We found that increasing reduction temperatures for the polyol reduction of RuCl_3 precursor was an ineffective method to increase the Ru particle size. Ru particles size only increased slightly from 2.3 nm to 2.5 nm when the reduction temperature was increased from 195 to 225 °C. In contrast, by reduction at different temperatures of $\text{Ru}(\text{acac})_3$ with polyol we were able to obtain nanoparticle catalysts in a size range between 2.7 nm and 5.2 nm. Transmission electron micrographs (Figure 3.1) show that Ru particles between 1.2 nm and 3.4 nm are mostly spherical. Larger particles tend to be more faceted.

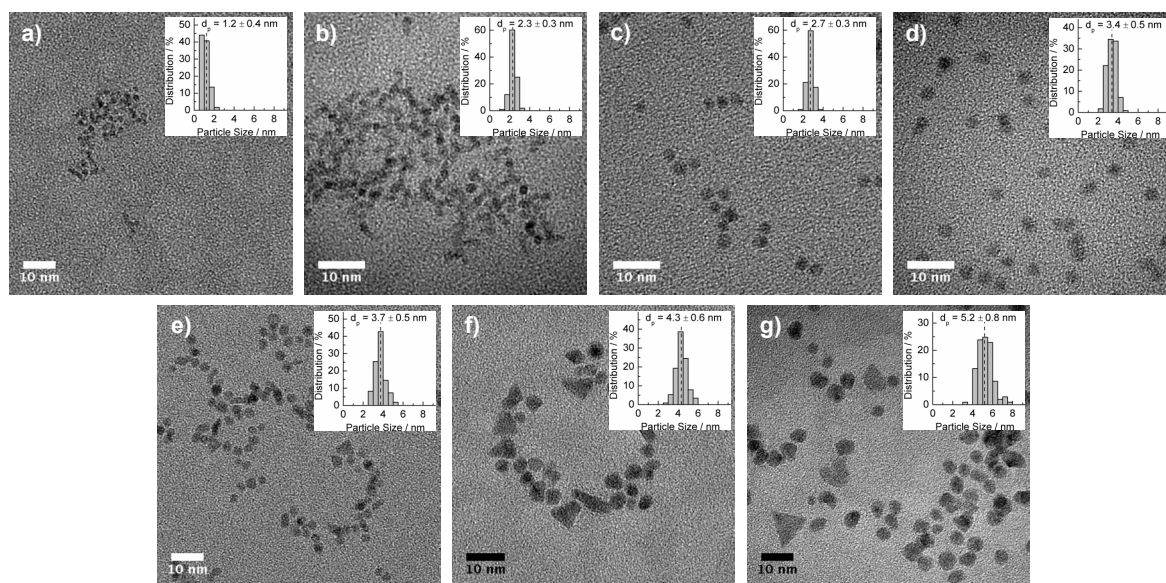


Figure 3.1: Electron micrograph and particle size distribution for (a) Ru-1.2, (b) Ru-2.3, (c) Ru-2.7, (d) Ru-3.4, (e) Ru-3.7, (f) Ru-4.3, and (g) Ru-5.2.

Table 3.1. Synthesis conditions and properties for Ru nanoparticles.^[a]

Catalyst	Reduction Method ^[b]	T (°C)	Ru Source	d_p ^[c] (nm)	Fraction Ru ⁰ ^[d] (%)	c_{Ru} ^[e] (μmol/mL)
Ru-1.2	H ₂	145	RuCl ₃	1.2 ± 0.4	90	35.6
Ru-2.3	Polyol	195	RuCl ₃	2.3 ± 0.3	85	35.8
Ru-2.7	Polyol	165	Ru(acac) ₃	2.7 ± 0.3	-	35.9
Ru-3.4	Polyol	175	Ru(acac) ₃	3.4 ± 0.5	80	34.1
Ru-3.7	Polyol	195	Ru(acac) ₃	3.7 ± 0.5	90	33.2
Ru-4.3	Polyol	215	Ru(acac) ₃	4.3 ± 0.6	-	29.0
Ru-5.2	Polyol	225	Ru(acac) ₃	5.2 ± 0.8	92	32.6

[a] Ru nanoparticles synthesis parameters: PVP/Ru molar ratio = 20, Mn(PVP) = 10 000, re-dispersed in 1.5 mL H₂O. [b] Polyol: 1,4-Butanediol as reducing agent, H₂: 20 bar H₂ as reducing agent. [c] Average particle size and standard deviation determined by TEM analysis. [d] Determined from XANES after second reduction with 20 bar H₂ at 150 °C. [e] Determined from ICP-AES for the synthesized Ru nanoparticles re-dispersed in 1.5 mL H₂O (theoretical concentration: 50 μmol/mL).

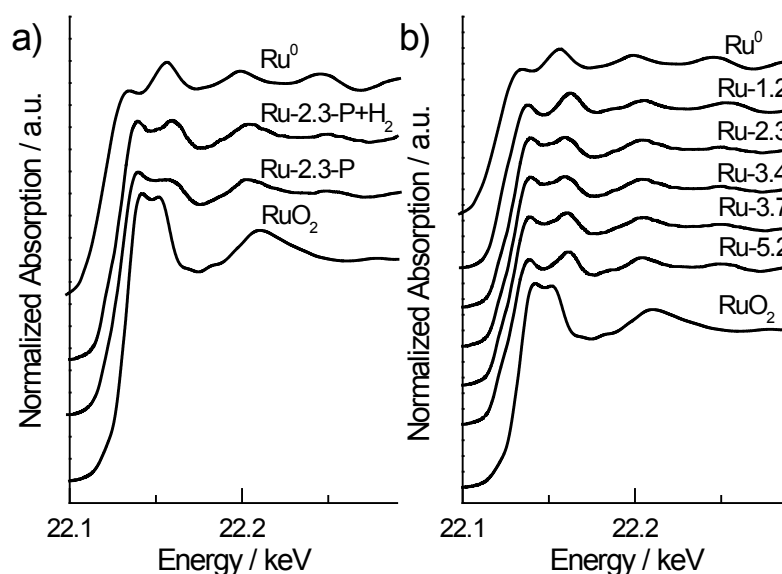
**Figure 3.2:** Ru *K*-edge XANES spectra for (a) Ru-2.3 reduced by different methods, and (b) Ru nanoparticles with different particle size.

Figure 3.2a shows the Ru *K*-edge XANES spectra for Ru-2.3 synthesized by polyol reduction (Ru-2.3-P) and after a second reduction with 20 bar H₂ (Ru-2.3-P-H₂). The spectra show that Ru-2.3-P and Ru-2.3-P-H₂ contain both metallic and oxidic Ru. The Ru⁰ content was determined by fitting the measured XANES spectra with linear combination of reference spectra of a metallic Ru foil and RuO₂ powder. Separate XPS analyses did not reveal the presence of chlorine, so the presence of cationic Ru should be due to RuO₂. The Ru⁰ content

for Ru-2.3-P and Ru-2.3-P-H₂ were 65 and 85 %, respectively. Similar to our previous study using NaBH₄ for reduction [16], the Ru nanoparticles reduced by polyol remain partially oxidic. The metallic Ru content for these particles is increased by a second reduction with 20 bar H₂ at 150 °C. The XANES spectra for differently sized Ru particles after the second reduction (Figure 3.2b) confirm the presence of oxidic and metallic Ru in all of the samples. The Ru⁰ content of the catalysts is listed in Table 3.1. Although small particles are more prone to oxidation than larger ones [17], our results indicate that, after the second reduction, the initial reduction method and particle size had only minor influence on the Ru⁰ content. The average Ru⁰ content was found to be 87 % with a deviation of 5 %.

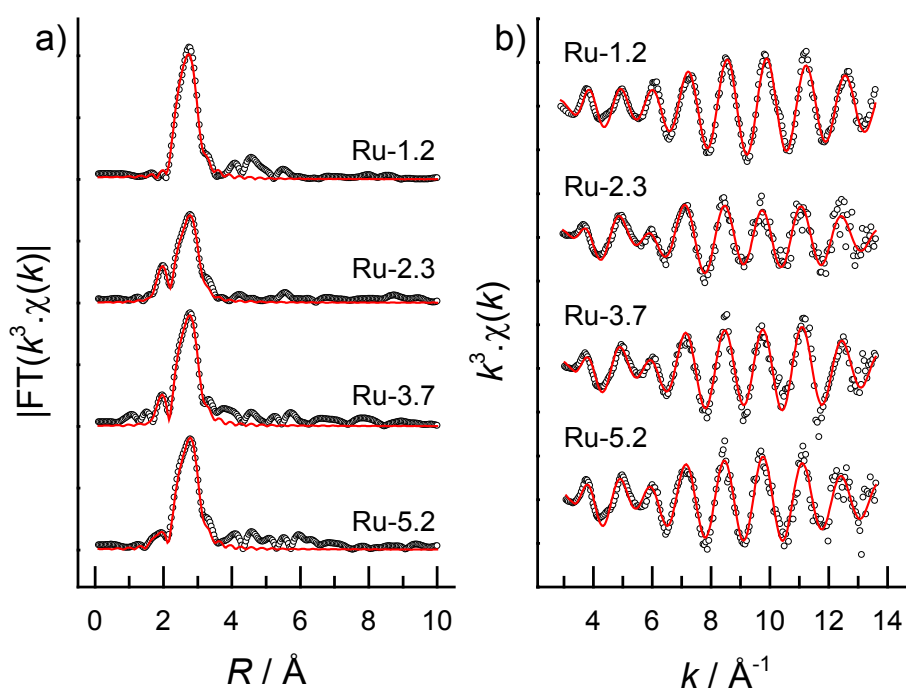


Figure 3.3: Experimental (O) and fitted model (red lines) for (a) FT EXAFS functions and (b) k^3 -weighted EXAFS oscillations of Ru-1.2, Ru-2.3, Ru-3.7 and Ru-5.2 after second reduction at 150°C with 20 bar H₂.

Figure 3.3 shows the experimental and fitted Fourier transformed k^3 -weighted EXAFS and $\chi(k) \cdot k^3$ functions for 4 Ru nanoparticle catalysts of increasing size (fit parameters in Table 3.2). The Fourier Transforms are dominated by a Ru–Ru shell with a small contribution of a Ru–O shell. The small Ru–O contribution indicates that the Ru particles are not completely reduced in agreement with the XANES analysis. The coordination number decreases with decreasing Ru particle size. All Ru particles exhibit Ru–Ru bond lengths comparable with that in bulk Ru (2.67 Å) with the exception of Ru-1.2 containing a slightly shorter Ru–Ru bond length of 2.64 Å.

Table 3.2. Fit parameters of k^3 -weighted EXAFS data of the Ru foil and Ru nanoparticle catalysts.					
Catalyst	EXAFS fit parameters ^[a]				
	Shell	N	R (Å)	$\Delta\sigma^2$ (Å ²)	E_0 (eV)
Ru foil	Ru-Ru	12	2.68	0.004	-7.9
Ru-1.2	Ru-Ru	6.1	2.64	0.005	-6.1
Ru-2.3	Ru-O	1.4	1.99	0.002	-0.5
	Ru-Ru	6.9	2.67	0.007	
Ru-3.7	Ru-O	1.1	1.97	0.002	-3.3
	Ru-Ru	7.5	2.67	0.006	
Ru-5.2	Ru-O	1.0	1.93	0.004	-2.6
	Ru-Ru	8.7	2.67	0.007	

[a] Only first Ru-O and Ru-Ru shells fitted; $\Delta k = 2.5\text{--}13.4 \text{ \AA}^{-1}$; estimated errors in R: $\pm 0.01 \text{ \AA}$, N: $\pm 20\%$, and $\Delta\sigma^2$: $\pm 10\%$.

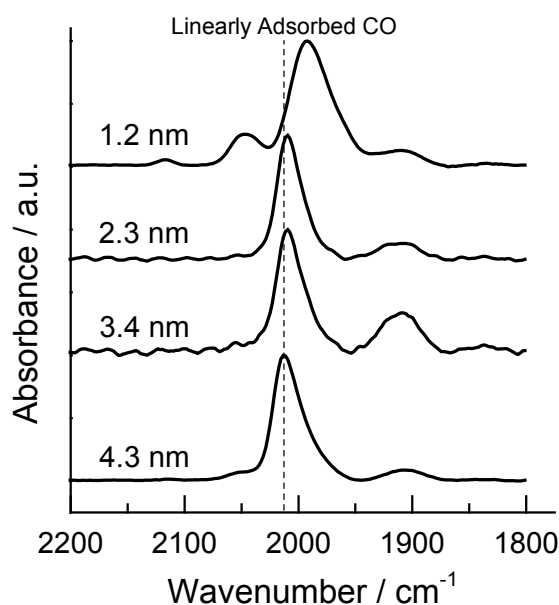


Figure 3.4: CO adsorption FTIR spectra measured at 150°C for Ru nanoparticles after second reduction.

Figure 3.4 presents the FTIR spectra of four Ru nanoparticle catalysts collected at 150 °C after drying and CO adsorption. Two main features can be observed in these spectra: a strong band centered at 1990-2015 cm^{-1} region with a shoulder at 2050 cm^{-1} and a weak broad band in the 1900-1950 cm^{-1} region. In addition, the IR spectrum for Ru-1.2 shows an additional band centered at 2116 cm^{-1} . For the assignment of the bands, we follow Chin et al. [18]: bridge-bonded CO at 1900 to 1950 cm^{-1} , linearly bonded CO at 1990-2015 cm^{-1} , dicarbonyl CO species adsorbed on Ru^0 at 2050 cm^{-1} and CO adsorbed on Ru^{n+} at 2116 cm^{-1} . A notable finding is that the band assigned to linearly adsorbed CO sites undergoes a red shift

with decreasing particle size in the range 4.3 to 1.2 nm. The red shift is largest when the average particle size decreases from 2.3 nm (2009 cm^{-1}) to 1.2 nm (1990 cm^{-1}). The CO is still linearly bonded when the band shift from 2009 to 1990 cm^{-1} , within the range usually observed linearly bonded CO range. Therefore, the shift is best explained by stronger adsorption of CO. It is also seen that a shoulder appears at 2050 cm^{-1} with decreasing particle size, which is due to Ru-dicarbonyl species. These surface complexes are likely due to CO adsorption on very low coordinated Ru surface atoms such as corner sites. The increase of this band is greatest when the particle size is decreased from 2.3 to 1.2 nm. This is consistent with decrease in coordination number for smaller particles as determined by EXAFS. The band at 2116 cm^{-1} is due to the presence of a small amount of oxidic Ru species on Ru-1.2.

Although EXAFS is able to provide structural information on the nearest neighbour arrangements, it is insensitive to long range atomic arrangement in the metallic nanoparticles. In contrast, high-energy X-ray diffraction (XRD) coupled with atomic Pair Distribution Function (PDF) has been shown to be a promising method to investigate the three-dimensional structure of nanosized objects [9-11]. XRD–PDF was performed for various Ru nanoparticle catalysts (Figure 3.5). The XRD pattern of bulk crystalline Ru (Figure 3.5a) shows well-defined Bragg peaks. Analysis of this XRD pattern gave the expected result that the atoms form an *hcp* structure. However, the XRD patterns for the Ru nanoparticles are very diffuse and cannot be analysed in the traditional way [10]. Henceforth, atomic PDF data analysis was employed. The atomic PDF $G(r)$ for polycrystalline Ru shown in Figure 3.5b can be fitted well by a *hcp* model (blue line) [19]. This indicates that the atomic PDF is able to reflect the 3D structure of crystalline Ru. However, fitting of the Ru nanoparticles data with the *hcp*-structure did not yield equally good fits (not shown). The low radial distance experimental atomic PDF $G(r)$ (Figure 3.5c) extracted from Figure 3.5b shows that the first coordination distance is approximately 2.68 Å for all particle sizes. This corresponds to the Ru–Ru bond length obtained from analysis of the EXAFS data (Table 3.2). In addition, the atomic PDFs show that a decrease in particle size leads to a shift in the position of the second and third coordination spheres (indicated by dashed lines). It can also be seen that the peaks of all coordination shells are broadened. The shift in the position of the coordination sphere indicates an increasing disorder when the particles become smaller [20]. The full width at half maximum (FWHM) of the first coordination sphere reflects both thermal and static disorder [20]. A larger difference between the FWHM of polycrystalline Ru and that of the nanoparticles at the same temperature reflects a stronger disorderliness [20]. Based on the

FWHM differences summarized in Table 3.3, it is observed that smaller particles exhibit stronger structural disorderliness compared to larger particles.

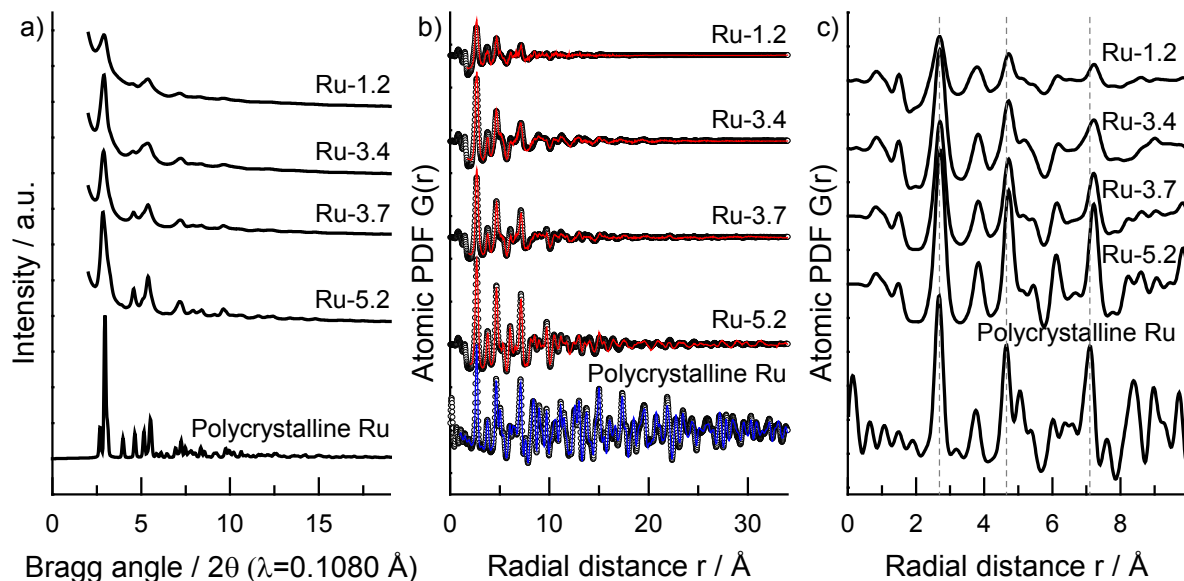


Figure 3.5: (a) High energy XRD pattern, (b) atomic PDFs: experimental data (○), *hcp* model fitting (blue), and RMC simulated model fitting (red), and (c) low radial distance PDFs, for Ru nanoparticles measured after second reduction.

Reverse Monte Carlo (RMC) simulations can be used to determine the structure from high-quality XRD data. As an example, Bedford et al. have recently found that Ru particles larger than 4 nm exhibit the *hcp* structure, whereas those smaller than 4 nm can only be described by a non-periodic atomic configuration (distorted structure) [10]. Therefore, RMC simulations were also employed here to fit the experimental atomic PDFs. The model PDFs computed from RMC refined atomic configurations (Figure 3.5b) show a good agreement between the experimental data and the model for all particle sizes. Representative models for average Ru nanoparticles obtained by RMC refinements are shown in Figure 3.6a. The Ru-5.2 nanoparticles predominantly exhibit the *hcp* structure with some structural disorder affecting different parts of the particles. The RMC-refined Ru particles in Ru-3.4 and Ru-3.7 contain a core with the *hcp* structure and a disordered surface shell. The diameter of the structured *hcp* core for Ru-3.4 and Ru-3.7 is 1.2 nm and 1.6 nm, respectively. From the Δ FWHM in Table 3.3, it follows that Ru-3.7 is more ordered than Ru-3.4. Given their very similar size, it may be suggested that Ru-3.7 has a larger *hcp*-core compared to Ru-3.4. In contrast to the larger particles, refinement of the Ru-1.2 PDF data shows that the whole structure of these nanoparticles is heavily disordered and cannot be described by the *hcp* structure. Based on the RMC models for the Ru nanoparticles, the average coordination

number are determined and presented in Table 3.3. The trends in the metal-metal coordination number with particles size are similar for the RMC-fitted XRD-PDF and the EXAFS data. However, the coordination numbers measured with EXAFS are lower than those obtained from the XRD data. This may be due to the use of only a single scattering path during EXAFS fitting. An indication of the partial overlapping of the first and second coordination shells in Ru particles is evident from the radial distribution functions for 3.4 and 3.7 nm particles (see Figure 3.5c).

Table 3.3. Properties of Ru nanoparticles obtained from XRD-PDFs measurements. ^[a]				
Catalyst ^[b]	CN _{avg.} ^[c]	CN _{surf. avg.} ^[d]	Atomic PDF of first coordination sphere	
			FWHM ^[e] (Å)	ΔFWHM ^[f] (Å)
Ru-1.2	8.2	4.5	0.45	0.15
Ru-3.4	9.7	5.6	0.42	0.12
Ru-3.7	10.0	5.9	0.38	0.08
Ru-5.2	10.4	6.0	0.33	0.03
Polycrystalline Ru	-	-	0.30	-
<p>[a] Atomic pair distribution function (PDF) extracted from high energy XRD data, and fitting performed by RMC. [b] Ru nanoparticles were re-reduced at 150°C under 20 bar H₂ for 2 h. [c] Average coordination number determined from the RMC model. [d] Average surface coordination number determined from the RMC model. [e] Full Width at Half Height (FWHM) of first coordination sphere from atomic PDF for Ru nanoparticles. [f] ΔFWHM = FWHM – FWHM_{polycrystalline Ru}.</p>				

As only the surface atoms of the nanoparticles are involved in the catalytic reaction, their coordination numbers (blue spheres in Figure 3.6a) were determined (blue bars in Figure 3.6b). The coordination numbers of the Ru nanoparticles obtained from a fit of the structure using the crystalline *hcp* structure, of the RMC-refined nanoparticles and of the surface atoms obtained from the latter are shown in Figure 3.6b-e. Since the first coordination distance for the neighbour reflected by the low-*r* part of the PDF *G(r)* is 3.4 Å (first minimum after the peak at 2.68 Å Figure 3.5c), the CN from the RMC model is determined by the number of metal atoms within a radius of 3.4 Å of each metal atom center. Ru atoms in the bulk have 12 first atomic neighbours. Due to the finite size of the Ru nanoparticles, the average coordination number is lower than 12. Compared to the distribution of coordination numbers of the simplest fit procedure, RMC refined nanoparticles show a wider spread in the number of first atomic neighbours. This is indicative of the non-ideal arrangement of the atoms in these nanoparticles. In Figure 3.6b-e, the coordination number of the surface atoms is seen to decrease when the particles get smaller. The average surface coordination number

are presented in Table 3.3. The average surface atom coordination number for Ru-1.2 (CN = 4.5) is significantly lower than that for Ru-3.4 (CN = 5.6). The significantly lower coordination number for Ru-1.2 is in agreement with the findings based on the IR studies of adsorbed CO.

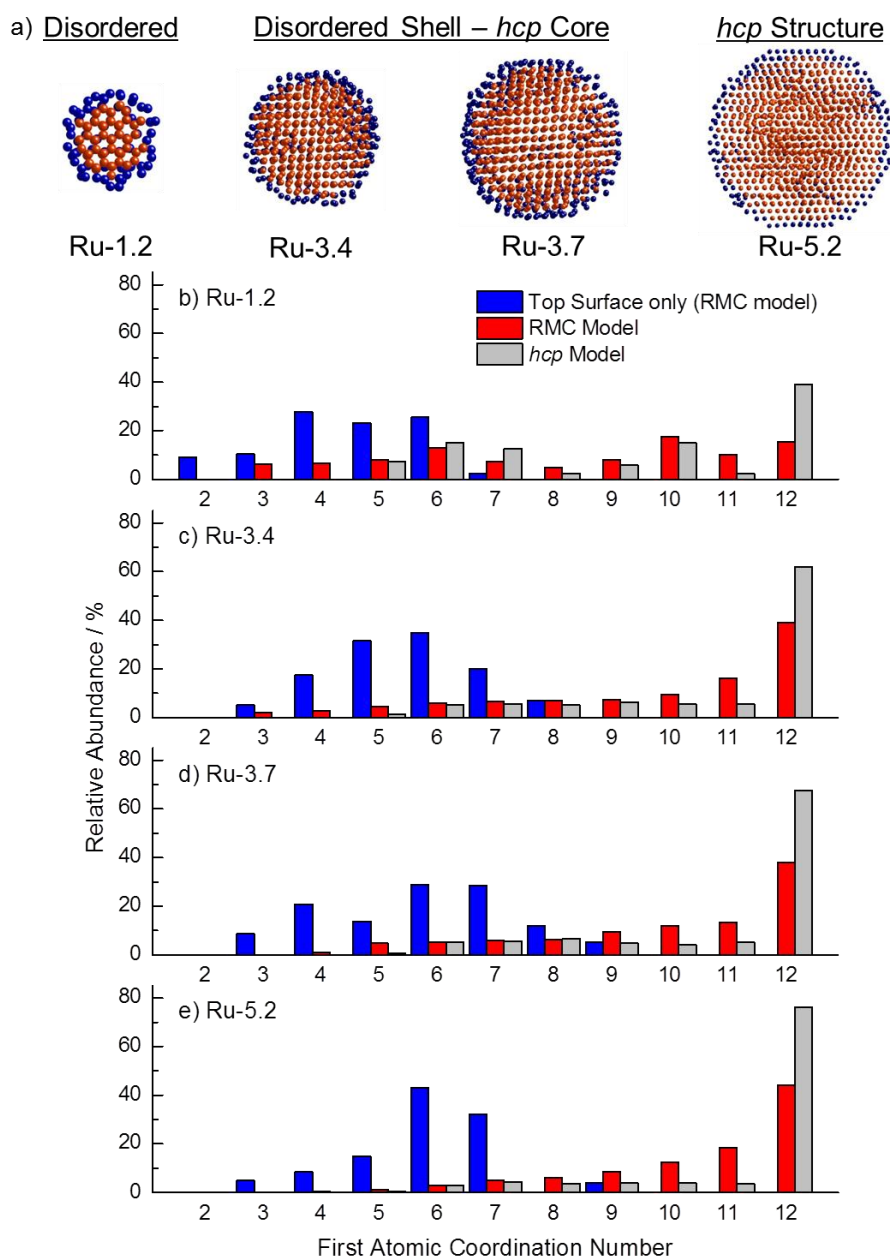


Figure 3.6: (a) Cross sections of RMC refined Ru nanoparticles structure (top surface atoms: blue spheres, internal atoms: red spheres), and coordination number distribution derived from hcp crystal structure, RMC refined Ru particles and top surface atoms of RMC refined Ru particles model for (b) Ru-1.2, (c) Ru-3.4, (d) Ru-3.7 and (e) Ru-5.2.

The surface atom coordination numbers (indicated by different colours) on the RMC-refined average particle representative model of the Ru nanoparticles are shown in Figure

3.7a. It is immediately clear from this figure that the surfaces of the representative model particles are highly disordered, even for the largest 5.2 nm Ru particle. To be more precisely, the surfaces of these models deviate significantly from the expected surfaces of an ideal nanoparticle enclosed by the most stable close-packed surfaces. Although the surface of the Ru-5.2 model is highly disordered, various well-defined surface topologies can be discerned. As shown in Figure 3.7b, close-packed and square planar sites, which resemble the *hcp*(0001) and *fcc*(100), are observed. Step-edge sites, similar to the *hcp*(11 $\bar{2}$ 1), can also be distinguished. In addition, more open surfaces containing so-named sawtooth sites are also seen. The sawtooth site bear some resemblance to the *hcp* (11 $\bar{2}$ 0) surface. Whilst more regular surface structures can be identified on the Ru-5.2 model, these are largely absent for the Ru-1.2, Ru-3.4 and Ru-3.7 models. The specific sites present at the surfaces of these nanoparticles and their coordination numbers are to be related to the trends in the catalytic activity in Chapter 4.

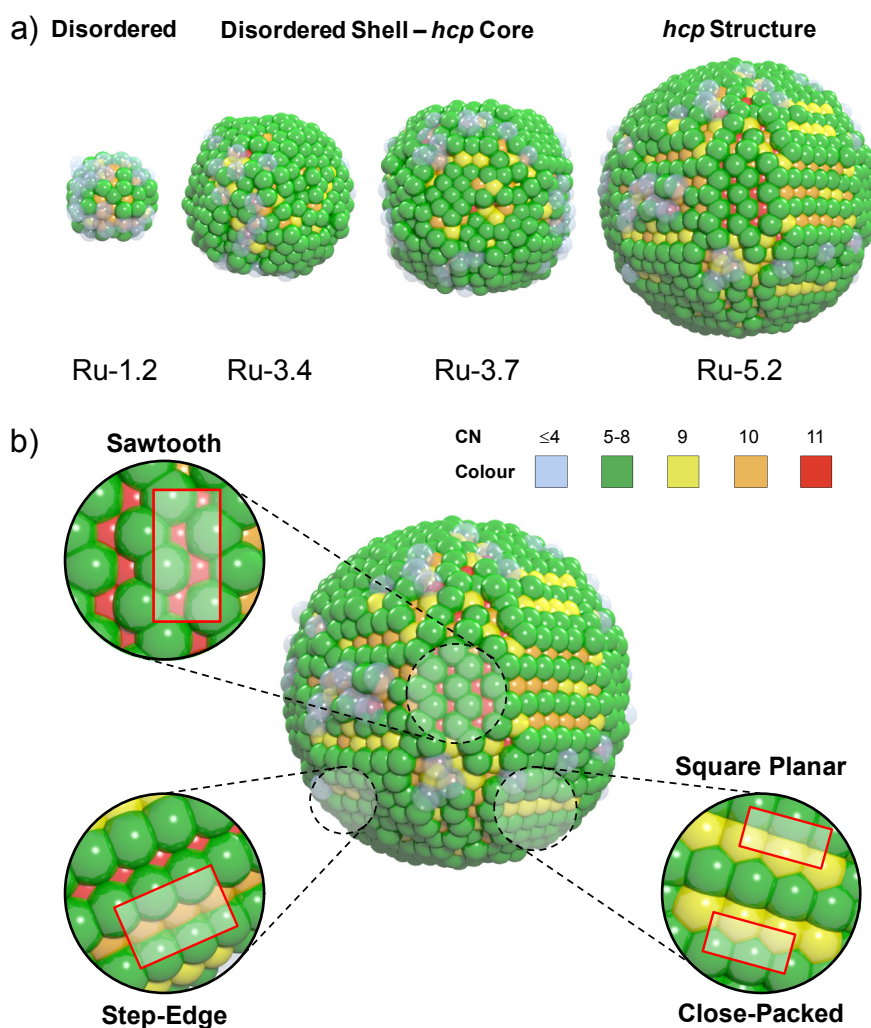


Figure 3.7: (a) Location of different coordination number on the RMC generated model for different Ru sizes, and (b) defined crystal surfaces identified on Ru-5.2.

3.4 Conclusion

Ru particles between 1 to 5 nm were prepared by liquid phase reduction of different Ru precursors at different temperature. These particles were characterized using TEM, CO adsorption FTIR, XANES, EXAFS and XRD-PDF. Ru particles between 1 to 5 nm were synthesized using polyol reduction. XANES shows that after a second reduction using high pressure H₂ in an autoclave batch reactor, the metallic Ru content for all catalyst are comparable. EXAFS and CO-adsorption FTIR studies revealed that the 1 nm Ru contain higher concentration of coordinatively unsaturated sites. The first coordination distance between Ru atoms obtained from XRD-PDF studies are similar to the Ru-Ru distance obtained from EXAFS. The XRD-PDF results also revealed that the nanoparticles exhibit the *hcp* crystalline structure with some structure disorder, which increases with decreasing particle size. By using Reverse Monte Carlo simulations, the 3D structure of different sized Ru particles were resolved and the coordination number distribution can be obtained for the Ru particles. The resolved structure of the Ru particles shows that the surface of the particles deviates significantly from the surface of an ideal Wulff nanoparticle. Although the surface of the 5.2 nm Ru model is also highly disordered, various well defined surfaces were identified on the resolved particle model.

References

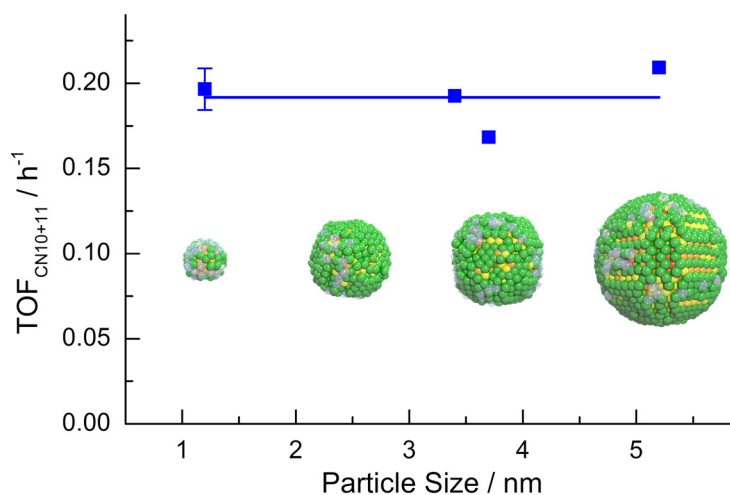
- [1] D. A. J. M. Ligthart, R. A. van Santen, E. J. M. Hensen, *J. Catal.* **2011**, *280*, 206-220.
- [2] G. A. Somorjai, C. Aliaga, *Langmuir* **2010**, *26*, 16190-16203.
- [3] K. Honkala, A. Hellman, I. N. Remediakis, A. Logadottir, A. Carlsson, S. Dahl, C. H. Christensen, J. K. Nørskov, *Science* **2005**, *307*, 555-558.
- [4] R. M. Rioux, B. B. Hsu, M. E. Grass, H. Song, G. A. Somorjai, *Catal. Lett.* **2008**, *126*, 10-19.
- [5] S. W. Lee, S. Chen, W. Sheng, N. Yabuuchi, Y.-T. Kim, T. Mitani, E. Vescovo, Y. Shao-Horn, *J. Am. Chem. Soc.* **2009**, *131*, 15669-15677.
- [6] A. M. Karim, V. Prasad, G. Mpourmpakis, W. W. Loneragan, A. I. Frenkel, J. G. Chen, D. G. Vlachos, *J. Am. Chem. Soc.* **2009**, *131*, 12230-12239.
- [7] T. Zambelli, J. Winterlin, J. Trost, G. Ertl, *Science* **1996**, *273*, 1688-1690.
- [8] S. Van Aert, K. J. Batenburg, M. D. Rossell, R. Erni, G. Van Tendeloo, *Nature* **2011**, *470*, 374-377.
- [9] V. Petkov, N. Bedford, M. R. Knecht, M. G. Weir, R. M. Crooks, W. Tang, G. Henkelman, A. Frenkel, *J. Phys. Chem. C* **2008**, *112*, 8907-8911.
- [10] N. Bedford, C. Dablenmont, G. Viau, P. Chupas, V. Petkov, *J. Phys. Chem. C* **2007**, *111*, 18214-18219.
- [11] V. Petkov, *Mater. Today* **2008**, *11*, 28-38.
- [12] X.-Y. Quek, Y. Guan, E. J. M. Hensen, *Catal. Today* **2012**, *183*, 72-78.
- [13] V. Petkov, *J. Appl. Crystallogr.* **1989**, *22*, 387-389.
- [14] T. Proffen, S. J. L. Billinge, *J. Appl. Crystallogr.* **1999**, *32*, 572-575.
- [15] G. Evrard, L. Pusztai, *J. Phys.: Condens. Matter* **2005**, *17*, S1.
- [16] X.-Y. Quek, Y. Guan, R. A. van Santen, E. J. M. Hensen, *ChemCatChem* **2011**, *3*, 1735-1738.
- [17] D. A. J. M. Ligthart, R. A. van Santen, E. J. M. Hensen, *Angew. Chem. Int. Ed.* **2011**, *50*, 5306-5310.
- [18] S. Y. Chin, C. T. Williams, M. D. Amiridis, *J. Phys. Chem. B* **2006**, *110*, 871-882.
- [19] H. E. Swanson, R. K. Fuyat, G. M. Ugrinic, *Natl. Bureau Stand. Circ. (U.S.)* **1955**, *359*, 1.
- [20] V. Petkov, "Pair Distribution Functions Analysis" in *Characterization of Materials*, John Wiley & Sons, Inc., **2012**.

Chapter 4

Structure Sensitivity in Ru Nanoparticles Catalyzed Fischer-Tropsch Synthesis: Catalytic Performance

Summary

The activity and selectivity of the Fischer-Tropsch reaction strongly depends on the Ru particle size, when varied between 1 to 5 nm. Low temperature data are reported for Ru particles suspended in the water phase. High oxygenates selectivity is found for small particles. The ASF chain growth parameter of oxygenates is lower than that of hydrocarbon for all particle sizes. The chain growth parameter for hydrocarbon formation is independent of particle size but is constant for oxygenates only for particles larger than 3 nm. The lower chain growth probability for oxygenates of small particles is related to the higher methane selectivity. Oxygenate and hydrocarbon formation occurs on different sites. The ASF chain growth parameter for oxygenate formation increases with temperature. This unusual temperature dependence is due the relatively slow rate of CO dissociation compared to the rate of C-C bond formation. Based on the resolved average representative model structure of the Ru particles, the changes in reactivity with particle size can be correlated with the density of atoms with coordination numbers of 10 and 11. The rate of CO consumption normalized to the fraction of such sites is found to be independent of particle size.



4.1 Introduction

Alternative carbon sources such as biomass, natural gas, and coal are increasingly considered as possible feedstock for the synthesis of liquid transportation fuels with the goal to reduce our dependence on crude oil reserves. A common and versatile chemical route to transportation fuels from these alternative feedstocks is their conversion by steam reforming or gasification into synthesis gas (a mixture of CO and H₂) followed by Fischer-Tropsch (FT) synthesis reaction [1-5]. Co, Fe and Ru are the typical transition metals that catalyze the FT reaction [2-4]. The rate of CO dissociation on less reactive transition metals such as Ni is too slow such that methane is the main product [6]. On metals such as Rh, Ir and Pt the rate of CO dissociation is also slow. Rh has intermediate reactivity and shows interesting selectivity to ethanol [1]. Here, we will present low temperature performance data of small nanoparticles that also exhibit high selectivity to oxygenates.

Among the various mechanisms proposed to account for the formation of long-chain hydrocarbons [7], the carbide one has found most support in literature. According to this mechanism, the building blocks for chain growth are CH_x surface intermediates [7-8]. The Fischer-Tropsch reaction comprises three main surface reaction steps: (i) CO dissociation and formation of CH_x intermediates, (ii) chain growth by CH_x insertion and subsequent hydrogen transfer steps, and (iii) termination to form the final product. On surfaces of low reactivity CO dissociation may proceed via an H-assisted pathway [9-10] as an alternative to direct CO dissociation [11]. For the chain growth step involving CH_x surface intermediates, different routes have been considered such as the Brady-Pettit alkyl [12] and the Gaube-Maitlis alkylidene/alkenyl [13] mechanisms. There are three different termination steps possible, namely H-addition, β -H elimination and CO insertion giving rise to paraffins, olefins and oxygenates, respectively.

Within the carbide mechanism, in order to form long chain products the rate of CO dissociation has to be fast and the rate of methane formation slow to provide sufficient CH_x intermediates to maintain a high rate of chain growth [7]. Also, the formation of long chain products requires the rate of termination to be slow compared to the rate of chain growth. This implies that in the carbide mechanism an increased rate of chain termination by CO insertion or through hydrogen transfer reactions would decrease the rate of chain growth, and, accordingly, the chain growth probability (α). When oxygenate formation and hydrocarbon formation is the result of competition for the same growing adsorbed hydrocarbon chain increased selectivity towards oxygenate formation implies that the intrinsic rate for chain

termination to oxygenates is faster than that for chain termination to hydrocarbon. The chain growth probabilities of both products would be the same. The main alternative proposal to the carbide mechanism for the FT reaction is the one formulated by Pichler and Schulz [14-15]. In this mechanism, it is proposed that CO inserts into the growing chain followed by C-O dissociation. Then the rate of CO activation can be slow compared to the rate of chain growth [7]. In this case high selectivity towards oxygenates reduces chain growth probability strongly for formation of hydrocarbons. High oxygenate production is only consistent with relatively low values of the chain growth probability.

Whereas for larger transition metal particles Fischer-Tropsch catalysis can be considered structure insensitive [16], for particles with dimensions below 10 nm the FT activity has been found to be a strong function of particle size [17-22]. Recent higher temperature SSITKA data for hydrocarbon production indicate that with decreasing size of the Ru nanoparticles the relative fraction of reactive sites decreases without change in intrinsic reactivity [22]. For Co particles, there are strong indications that also the intrinsic reactivity of the reactive center changes [20]. The critical particle size below which the CO consumption rate becomes structure sensitive is in the 7-10 nm range for Co [17-20] and 6-10 nm for Ru [21-22]. This structure sensitive behavior has been attributed to the decreasing stability of step-edge sites for smaller particles, which are essential for low-barrier CO dissociation, [7-8]. An alternative explanation is that CO or C atoms adsorb too strongly on small particles, thus poisoning part of the catalytic surface [17-20]. Salmeron et al. recently suggest that particle size affects in FT is due to difference in the rate of H₂ dissociation [23]. It was also reported that smaller particles produce more methane and have a lower C₅₊ selectivity [17, 22]. Apart from the particle size, the crystal structure of nanoparticles also affects their activity. Recent studies have found indications that *hcp*-Co is more active than *fcc*-Co [24-25].

In analogy with commercial practice, most laboratory studies on the FT reaction are carried out in fixed bed or slurry phase reactors. An interesting alternative approach involving FT reaction in the aqueous phase in a batch reactor was recently demonstrated by Xiao et al. [26]. In this pioneering work, the dominant reaction products were reported to be hydrocarbons. We have recently performed similar experiments focusing on the effect of the reaction temperature [27]. We found that Ru nanoparticle catalysts produced a mixture of long-chain hydrocarbons and oxygenates under these anomalous conditions (aqueous phase, temperatures below 200 °C). Exceptionally high selectivity towards long chain oxygenates (aldehydes and alcohols) was observed at relatively low temperatures [27]. Hydrocarbons

were suggested to be formed on sites with low barrier for CO dissociation, likely involving step-edge sites, whereas oxygenates were thought to be formed on sites with a higher barrier for CO dissociation. Recently, Wang et al. investigated the effect of ionic promoters on the Ru catalyzed FT reaction and also reported the formation of substantial amounts of oxygenates [28].

In this contribution, we focus on the effect of Ru nanoparticle size and reaction conditions on the activity and selectivity in the aqueous phase FT reaction. Polyvinylpyrrolidone (PVP) stabilized Ru nanoparticles in the 1 to 5 nm range were prepared and characterized for their bulk and surface structure. The catalytic performance in the FT reaction is correlated to the size and structure of the nanoparticles.

4.2 Experimental Methods

4.2.1 Catalytic Activity Measurements

Prior to reaction, an amount of catalyst (50 μmol Ru) was dispersed in 3 mL of deionized water and re-reduced in a 10 mL stainless steel autoclave at 150°C with 20 bar H_2 for 2 h under vigorous stirring. After reduction, the autoclave was cooled to room temperature in an ice bath before releasing the pressure. The liquid phase FT reaction was carried out at 30 bar for 24 h in the same autoclave. The autoclave was flushed 3 times with CO, before being pressurized with CO followed by H_2 to 30 bar (molar ratio $\text{H}_2/\text{CO} = 2$). The autoclave was sealed and the autoclave body was heated to the reaction temperature with a band heater controlled by a temperature controller. After 24 h, the reaction was terminated by immersing the autoclave into an ice bath.

The gas-phase products were analysed with an Interscience Compact GC system, equipped with an $\text{Al}_2\text{O}_3/\text{KCl}$ column and a flame ionization detector (FID). For analysis, the gas cap was flushed through a 6-way valve allowing injection onto a gas chromatograph. Methane, ethane, ethylene, propane and propylene were analysed against a standard gas mixture. For analysis of the liquid phase, an extraction was carried out with diethyl ether containing *p*-cymene as an internal standard. The organic phase containing the products was then analysed with a GC (QP5050, Shimadzu) equipped with a Rxi-5ms capillary column (30 m \times 0.25 mm \times 0.5 μm) and a flame ionization detector (FID). Identification and quantification of linear alkanes (C_6 to C_{16}), alcohols (C_4 to C_{12}) and aldehydes (C_4 to C_{12}) was established with reference compounds and *p*-cymene as the internal standard. GC response factors for other hydrocarbons (C_{17+}) and oxygenates (C_{13+}) were estimated by extrapolation.

The identity of the products was also verified with a GC-MS equipped (GC-MS, QP5050, Shimadzu) with a Rxi-5ms capillary column.

The rate of the FT reaction (r), turnover frequency (TOF), and selectivity were calculated based on the number of moles of carbon being formed in the products according to the following formula:

$$r = \frac{\text{total mol C formed in all products}}{\text{mass of Ru} \times \text{reaction time}}$$

$$\text{TOF} = \frac{\text{total mol C formed in all products}}{(\text{mol Ru}_{\text{surface atoms}}) \times \text{reaction time}}$$

$$\text{TOF}_{\text{CN10+11}} = \frac{\text{total mol C formed in all products}}{(\text{mol Ru}) \times x_{\text{CN10+11}} \times \text{reaction time}}$$

$$\text{Selectivity to hydrocarbon or oxygenate} = \frac{\sum(\text{mol of C}_n^{\text{HC/oxy}} \times n)}{\text{total mol C formed as products}}$$

with the $\text{mol Ru}_{\text{surface atoms}} = \text{mol Ru} \times D$, and $x_{\text{CN10+11}} = x_{\text{CN10}} + x_{\text{CN11}}$. Where x_{CN10} and x_{CN11} are the fraction of of Ru atoms with coordination number 10 and 11 respectively.

The dispersion (D) was calculated assuming spherical shapes by using the formula given by Scholten et al. [29]

$$D = 10^{21} \times \frac{6 \times M \times \rho_{\text{site}}}{d_p \times N_{\text{Av}} \times \rho_{\text{metal}}}$$

with M being the atomic weight of Ru, ρ_{site} the surface density (16.3 Ru atom/nm²), ρ_{metal} the density of metal (12.3 g/cm³), d_p the Ru particle size and N_{Av} the Avogadro's number. Hydrocarbon selectivity includes alkanes and alkenes and oxygenate selectivity aldehydes and alcohols.

4.2.2 Density Functional Theory Calculations

In order to compute the activation energy for CO dissociation on models representative for the surface of 5.2 nm Ru nanoparticles, Density Functional Theory (DFT) calculations were performed using the Vienna Ab initio simulation package (VASP). The projector-augmented wave (PAW) method was used in conjunction with a Perdew-Becke-

Ernzerhof (PBE) exchange-correlation functional. The kinetic cutoff energy for the plane waves was set to 500 eV. As such computations are prohibitively expensive for a 5.2 nm Ru nanoparticle, we extracted relevant parts out of the model nanoparticle (size roughly 1.5 nm, typically 150 atoms). Such particles were treated as a cluster. In order to retain as much as possible the original structure of the nanoparticle around the reaction center, the Ru atoms outside a sphere with a diameter of 1 nm around the Ru surface atom which binds the CO molecule were frozen. As the size of the periodic cell was approximately 20 Å in each direction, it was sufficient to only use the Γ -point in the calculations. In the calculations, all the degrees of freedom were optimized using the conjugate-gradient algorithm, as implemented in VASP. The transition states were found by optimizing the highest image, as found by a nudged elastic band calculation, by means of a quasi-Newton optimization scheme. In order to check the nature of the extrema on the potential energy surface, frequency calculations were performed using the finite difference technique. The initial and final states of the elementary reaction paths were found to be local minima, while the transition states were checked to have a single imaginary frequency with a corresponding eigenvector in the direction of the reaction path.

4.3 Results

4.3.1 Effect of Temperature

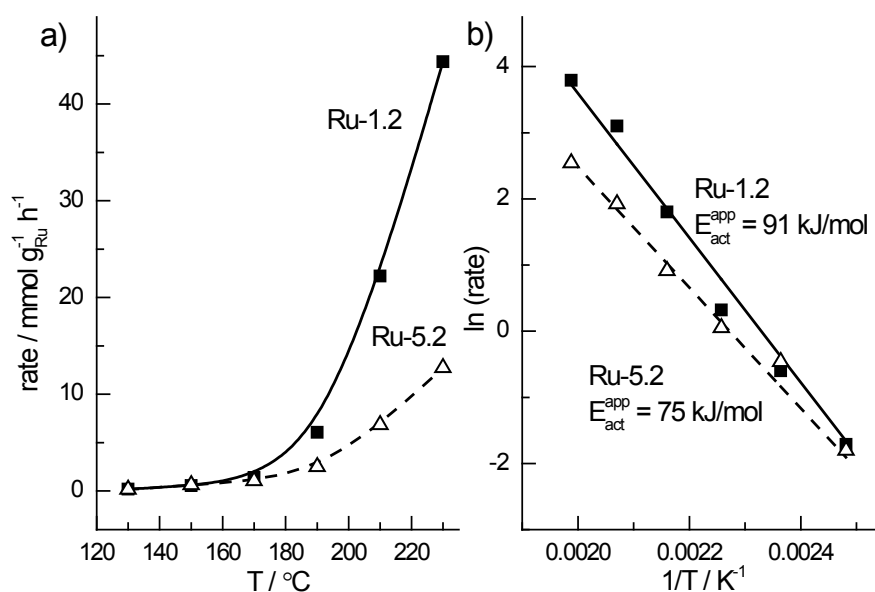


Figure 4.1: Effect of reaction temperature on activity for FT reaction catalyzed by Ru-1.2 and Ru-5.2: (a) rate, and (b) Arrhenius plot.

Figure 4.1 shows the effect of reaction temperature on the activity of aqueous phase FT synthesis for Ru-1.2 and Ru-5.2. With an increase of the reaction temperature from 130 to 230 °C, the CO consumption rate increases from 0.2 to 44.4 and from 0.2 to 12.7 mmol/g_{Ru}.h for Ru-1.2 and Ru-5.2, respectively (Figure 4.1). The apparent activation energies (E_{act}^{app}) calculated from these data (Figure 4.1b) are 91 (Ru-1.2) and 75 (Ru-5.2) kJ/mol. Within the carbide mechanism the activation energies relate to the apparent activation energies of the CH_x formation reaction from adsorbed CO [30]. The changes in apparent activation energies (E_{act}^{app}) with particle size are possibly due to the changes in selectivity of oxygenate versus hydrocarbon formation to be discussed in the next section. These values for E_{act}^{app} are in the same range as values (67-109 kJ/mol) reported for gas phase FT reaction using Ru catalysts [31].

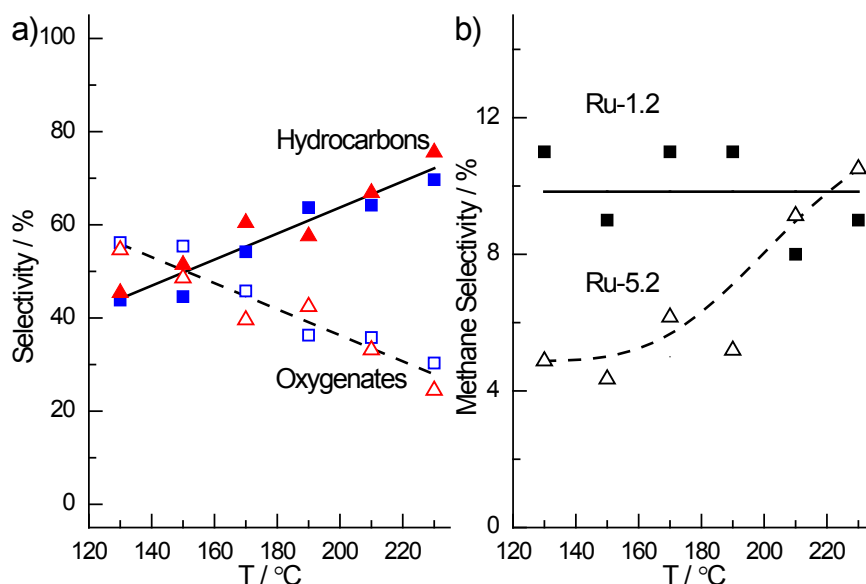


Figure 4.2: Effect of reaction temperature on FT reaction catalyzed by Ru-1.2 and Ru-5.2, (a) hydrocarbons and oxygenates selectivity (Hydrocarbons: ■, ▲, Oxygenates: □, △, Ru-1.2: ■, □ and Ru-5.2: ▲, △), and (b) methane selectivity.

Figure 4.2a shows the hydrocarbon and oxygenate selectivities for Ru-1.2 and Ru-5.2. Their general trend as a function of temperature is comparable to the one reported earlier by us for 2 nm Ru nanoparticles [27]: increasing the temperature results in a decrease of oxygenate selectivity. In the temperature range 130 to 230 °C, the oxygenate selectivity decreases similarly from 55 to 30 % (Figure 4.2a). Following the carbide mechanism, oxygenates are the product of termination by inserting CO into the growing chain on the surface. Simulations indicate that a high CO coverage is consistent with hydrocarbons as well as oxygenates formation [30]. The temperature dependence of oxygenates selectivity can

relate to (i) different CO activation barriers of the respective sites that form preferentially oxygenates or hydrocarbons or (ii) the activation energy for termination to hydrocarbons is higher than that to form oxygenates. Another observation from Figure 4.2a is that Ru-1.2 generally gives higher oxygenates selectivity compared to Ru-5.2. The effect of different particle size on FT reactivity will be discussed in the next section.

Table 4.1. Effect of C ₁₀ aldehyde or olefin addition to aqueous-phase FT reaction catalyzed by Ru-1.2. ^[a]						
Component	X ^[b] (%)	FT rate (mmol/g _{Ru} .h)	S _{HC} (%)	S _{OXY} (%)	α_{HC}	α_{OXY}
-	-	0.54	45	55	0.90	0.55
Decanal ^[c]	93	0.51	50	50	0.88	0.57
1-Decene ^[c]	77	0.58	50	50	0.87	0.59 / 0.72 ^[d]
[a] Reaction conditions: Co-addition component (1 μ mol), Ru nanoparticles (50 μ mol), H ₂ O (3 mL), P = 30 bar (H ₂ /CO molar ratio = 2), T = 150°C, t = 24 h. [b] Decanal or 1-decene conversion. [c] Contribution of decanal or decene was excluded from calculation of rate, selectivity and α . [d] α_{OXY} is 0.59 from C ₄ to C ₁₄ and changes to 0.72 above C ₁₄ .						

It has been shown before that secondary reactions of the reaction products of the FT reaction may have a significantly effect on the product distribution [32-34]. Relevant to the present work, Chen et al. reported the degradation of aqueous FT oxygenates to hydrocarbons under a H₂ pressure of 98 bar using a Ru catalyst [35-36]. The likely reaction pathway for deoxygenation is acid-catalyzed dehydration of the alcohol and hydrogenation to the paraffin [37]. It should be noted that the reaction mixture was slightly acidic in the work of Chen et al. due to the presence of organic acids in the solution [35-36]. To exclude the possibility that the selectivity changes as a function of temperature are caused by secondary reactions of aldehydes and alcohols, we carried out several reactions in the presence of decanal. We verified that the pH of the solution was neutral before and after the reaction. Table 4.1 shows that the addition of decanal does not affect either the FT rate nor the selectivities and chain growth probabilities. The only product from decanal is decanol. These results show that no preferential cracking of the oxygenated products during aqueous-phase FT occurs. These data also provide a strong indication that the chain growth reactions does not proceed via the Pichler-Schulz mechanism. Westrate et al. have recently shown that ethanol adsorbed on a Co(0001) single crystal surface can undergo C-O bond cleavage to produce C₂H_x and O surface intermediates [38]. This is an essential elementary reaction step in the Pichler-Schulz

mechanism. The present results clearly show that the adsorbed decanal or decanol will not undergo C-O bond cleavage to form an intermediate for further chain growth.

Another reaction pathway to be considered is the involvement of cationic Ru species in the formation of oxygenates. The Ru nanoparticle catalysts contain ~10% cationic Ru. The location of these cations is not clear, but it is not unreasonable to assume that they are present at the surface of the nanoparticles. However, we discard the possibility that cationic Ru on the nanoparticles causes oxygenates formation based on our previous study (Chapter 2, Table 2.1), showing that the concentration of such cationic Ru species has no significant effect on the product selectivities [27].

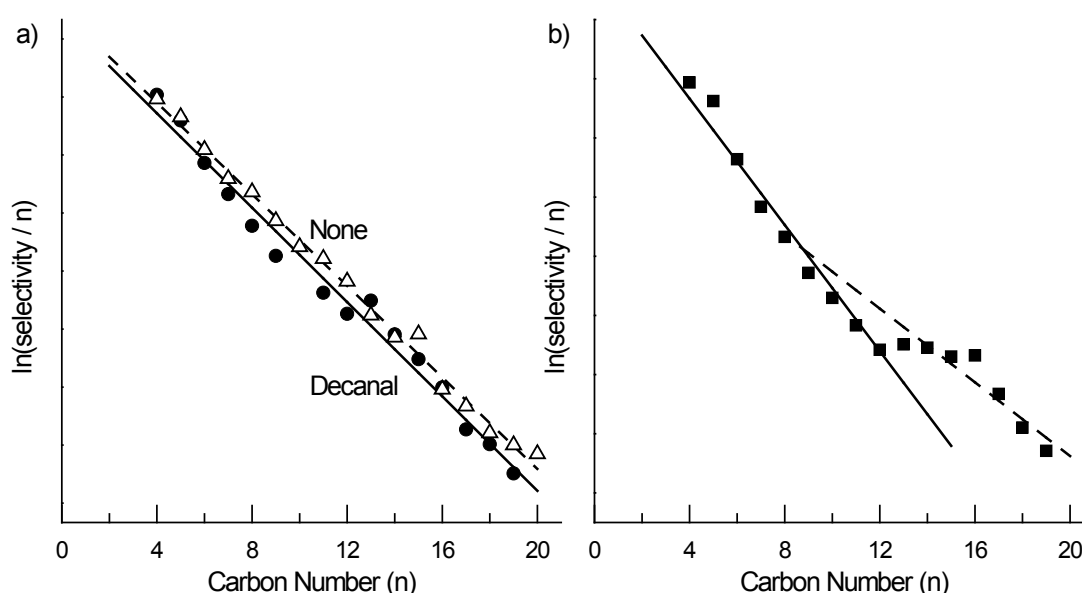


Figure 4.3: Oxygenates AFS plot for Ru-1.2 catalyzed FT reaction for (a) no co-addition and co-addition of decanal, and (b) co-addition of decene.

Related to this, it may be surmised that the oxygenates are formed via the secondary hydroformylation of product olefins. This reaction is typically catalyzed by homogeneous complexes and Ru is a very active catalyst for this purpose [39]. The possibility to carry out hydroformylation with metallic nanoparticles has also been reported recently [40]. To establish the relevance of hydroformylation in oxygenates formation, we carried out an additional experiment by adding 1-decene to the reaction mixture. Table 4.1 shows that its addition did not significantly affect the FT rate, the selectivities nor α_{HC} . 1-Decene was mainly converted to decane. It was found that the selectivity of C_{11} -oxygenates was 4%, which is only marginally higher than the selectivity of 2% for the experiment without addition of 1-decene. It is interesting to observe that addition of 1-decene resulted in an increase in α_{OXY} for oxygenated products longer than C_{11} , whilst the chain growth probability

for shorter oxygenates was unaffected (Table 4.1 and Figure 4.3). The chain growth probabilities for the hydrocarbons is unaffected. Note that n-decane was left out of these considerations, because it is the main reaction product from 1-decene hydrogenation. This result clearly shows that 1-decene is re-adsorbed on the catalytic surface and used in further chain growth of oxygenates and not of hydrocarbons. A main conclusion of these data is that oxygenates formation does not occur via hydroformylation of intermediate olefins. The finding that 1-decene participates in further chain growth of oxygenates may be taken as an indication that the surface intermediate for oxygenates chain growth is different from the one for hydrocarbons chain growth. This would decouple the mechanisms for formation of hydrocarbons and oxygenates.

Figure 4.2b shows that methane selectivity for both Ru-1.2 and Ru-5.2 are below 12% in the temperature regime 130 to 230 °C. Ru-1.2 gives substantially higher methane selectivity at lower temperature. The methane selectivity for the smallest particle size catalyst is independent of temperature. For Ru-5.2, the methane selectivity increases from 5 to 10%, when temperature increases. This difference in methane selectivity trend indicates that there is a change in the competition for CH_x to terminate as methane versus being incorporated into the growing chain as a function of particle size. The constant selectivity for methane on the small particle suggests a common intermediate with the growing hydrocarbon chains. When the activation energy of CO activation is high compared to that of methane formation, it results in higher methane selectivity [30].

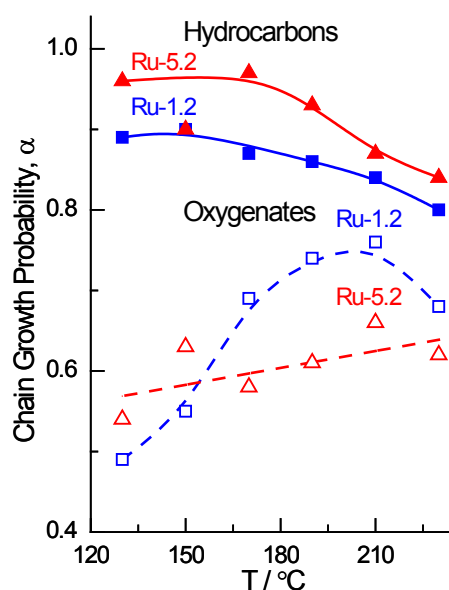


Figure 4.4: Effect of reaction temperature on chain growth probability for FT reaction catalyzed by Ru-1.2 and Ru-5.2 (Hydrocarbons: ■, ▲, Oxygenates: □, △, Ru-1.2: ■, □ and Ru-5.2: ▲, △).

The effect of temperature on the chain growth probability for Ru-1.2 and Ru-5.2 is shown in Figure 4.4. As the short chain oxygenates could not be measured in our experiments, the chain growth probabilities are calculated based on C₄₊ products only. It is important to note that similar to earlier work different chain growth probabilities are found for the chain length distribution of hydrocarbons (α_{HC}) and oxygenates (α_{OXY}) [27]. This difference has been attributed earlier to the presence of different reaction centers for formation of oxygenates and hydrocarbons on the Ru nanoparticle surface [27]. Upon increasing the reaction temperature from 130 to 230 °C, the hydrocarbon chain growth probability (α_{HC}) is found to decrease for both nanoparticle catalysts. This usually found behaviour [41-42] is consistent with the higher activation energy for chain termination compared to the overall rate of chain growth [7-8].

The chain growth parameters α_{OXY} for Ru-1.2 and Ru-5.2 show an anomalous temperature dependence compared to that of hydrocarbon formation. The initial increase of α_{OXY} for Ru-5.2 with temperature is comparable to what was found previously for 2 nm Ru nanoparticles [27]. For Ru-1.2, α_{OXY} goes through a maximum at 210 °C and decreases with a further increase in the reaction temperature. The increase in α_{OXY} is much more pronounced for Ru-1.2 compared to Ru-5.2. Trends for α will be further elaborated in the discussion section using kinetic considerations.

4.3.2 Effect of Particle Size

As is apparent from several recent reports [17-22], the FT reaction is structure sensitive. We investigated the effect of particle size in aqueous FT synthesis in more detail at a temperature of 150 °C. The particle size dependence of the FT activity is shown in Figure 4.5. The weight-based rate of the Ru nanoparticle catalysts shows a maximum around 2.3 nm for particles between 1.2 and 3.7 nm (Figure 4.5a). With a further increase of the Ru nanoparticle size the rate increases strongly. When the surface-atom normalized rates (TOF) are plotted against particle size (Figure 4.5b), it is seen that the activity increases with particle size with a plateau between 2.3 and 3.7 nm. These activity trends are in very good qualitative agreement with literature data for supported Ru nanoparticle catalysts [21-22]. Both Kang et al. [21] and Carballo et al. [22] found that the FT activity of Ru nanoparticles decreases below a critical size of 7-10 nm. Kang et al. investigated Ru nanoparticles sized between 3 and 10 nm supported on carbon nanotubes [21]. Carballo et al. studied Ru/Al₂O₃ with Ru nanoparticle sizes between 4 and 23 nm [22]. Neither contribution included Ru particles

smaller than 2 nm. Similar to our observations, the surface-atom normalized TOF reported by Kang et al. shows a region of structure insensitivity in the FT reaction between 2.5 and 4 nm and an increase in TOF for particles larger than 4 nm. Consistent with this, Carballo et al. found a similar increasing TOF for particles larger than 4 nm [22].

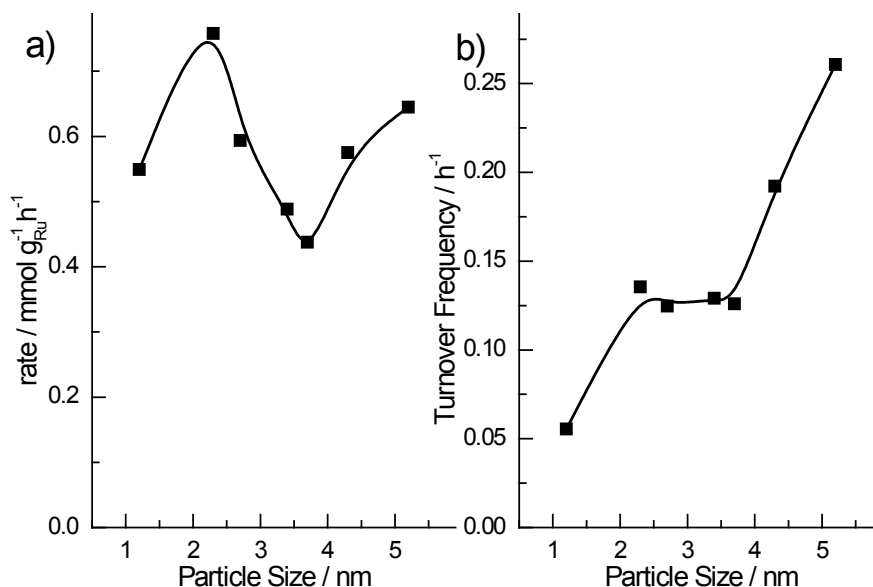


Figure 4.5: Effect of particle size on FT reaction: (a) Rate and (b) surface normalized Turnover Frequency (TOF).

Although the origin of the particle size dependence has not been elucidated yet, our data support the assumption that a minimum size of the nanoparticles is required to sustain step-edge sites needed for facile CO dissociation [7, 17]. In line with the early suggestions of Van Hardeveld [43], Honkala et al. reported that particles smaller than 2 nm do not contain step-edge sites [44]. On highly regular cuboctahedron particle the highest density of step-edge sites is predicted for 2 nm particles [44]. It has been argued that CO dissociation may preferentially occur via H-assisted pathways when step-edge sites are not available [9-10, 45-46]. Recent quantum-chemical calculations for Ru surfaces show that direct CO dissociation on step-edge sites is preferred over H-assisted CO dissociation [11]. In the absence of a clear method to determine the step-edge site density, we cannot firmly conclude on the reason for the activity trends as a function of particle size. It should be noted that the Honkala data are based on idealized ‘Wulff’ nanoparticles. Chorkendorff recently employed CO isotope scrambling on differently sized Ru nanoparticles (3-12 nm) and found that the scrambling activity increases with particle size [47]. The increasing activity was correlated to the increased density of step-edge sites for larger particles. Indeed, several further indications from literature strengthen the supposition that step-edge sites are also formed on terraces of

larger nanoparticles [48-53]. For instance, Nielsen et al. reported that large Ru particles have a different morphology with rougher surfaces than relatively small particles [48]. In another study, Karim et al. found that supported Ru with larger particle size form unusual shapes [49]. By combining EXAFS analysis with a theoretical model of the structure, they concluded that larger particles contain more step sites. Adsorbates can also cause roughening of smooth single crystal surfaces, giving rise to the formation of defects such as step-edge sites. Surface roughening of smooth single crystal surface induced by CO and H₂ has been reported for Pt and Rh [50] and Co [51-53]. Hence, we speculate that the surface planes on Ru nanoparticles greater than 4 nm are large enough to accommodate further layers of Ru giving rise to an increased density of step-edge sites.

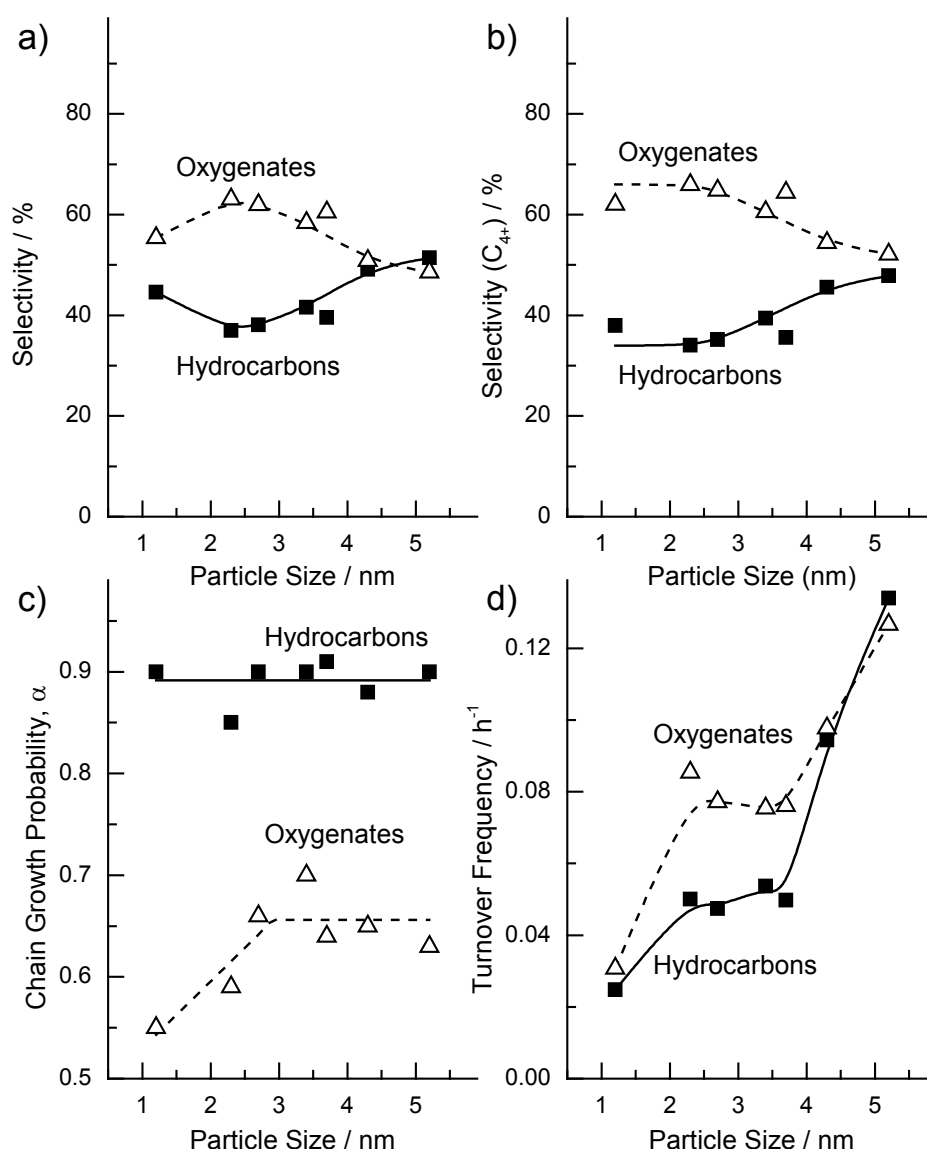


Figure 4.6: Effect of particle size on FT reaction: (a) selectivity, (b) selectivity for only C₄₊ products, (c) hydrocarbons and oxygenates chain growth probability, and (d) activity for hydrocarbons and oxygenates formation).

Figure 4.6a shows that the oxygenates selectivity decreases when the particle size increases from 2.3 to 5.2 nm, but increases when size increases from 1.2 to 2.3 nm. The lower oxygenates selectivity for the Ru-1.2 nm compared to the 2.3 nm particles is due to the higher selectivity towards methane as shown in Figure 4.7. The higher methane selectivity on the 1.2 nm is probably due the higher surface density of sites with higher barrier for CO dissociation, which favours methane formation [7]. We hypothesize that methane formation probably occurs on the oxygenates growth sites which we propose to have higher barrier for CO dissociation. With a higher concentration of sites with high barrier for CO dissociation, one would expect more methanol being formed. However due to experimental limitations, oxygenates with less than four carbon atoms were not analysed in our studies. In order to understand the effect of higher methane selectivity, we recalculated the selectivity by taking into account only C_{4+} products (denoted as C_{4+} -selectivity). Figure 4.6b shows that the C_{4+} -selectivity for oxygenates remains constant when the particle size is increased from 1 to 3 nm and decreases with further increase of the particle size. This indicates that the ratio of oxygenates to hydrocarbons growth sites remains constant for smaller particles. The decrease in oxygenates C_{4+} -selectivity above 3 nm could either imply that (i) the ratio of oxygenates to hydrocarbons growth sites decreases or (ii) the intrinsic rate of oxygenates formation decreases with respect to that of hydrocarbons formation. Recent SSITKA experiments have shown that the residence time for CH_x species is independent of Ru particle size [22]. If CH_x residence time on the catalytic surface remains unchanged, we would expect that the change in the intrinsic rate of oxygenates or hydrocarbons formation would affect α . However, as Figure 4.6c shows that both α_{OXY} and α_{HC} are not influenced by the increase in Ru particle size when the particles are larger than 3 nm, we conclude that there is no change in the intrinsic rate of oxygenates and hydrocarbons formation. Hence, the decrease in the C_{4+} -selectivity for oxygenates with particle size is primarily due to the decrease in the relative ratio of oxygenates to hydrocarbons growth sites.

Figure 4.6c shows that α_{HC} is independent of particle size, while α_{OXY} increases from 1 to 3 nm but remains constant above 3 nm. Hydrocarbons exhibit higher chain growth probability compared to oxygenates. This supports our earlier proposal that oxygenates and hydrocarbons are formed on two different catalytic reaction centers [27]. If oxygenates and hydrocarbons are formed on similar catalytic sites with only a different termination step, one would expect similar α , or at least similar trends in case one product would undergo more secondary reactions than the other, for oxygenates and hydrocarbons as a function of Ru

particle size. In addition, the lower value of α_{OXY} compared to that of α_{HC} is consistent with CO dissociation at oxygenates growth sites having a higher activation barrier, and the termination step to oxygenates having a lower activation barrier compared that for hydrocarbons as will follow from Eq. (4.6) and (4.7) in the discussion section.

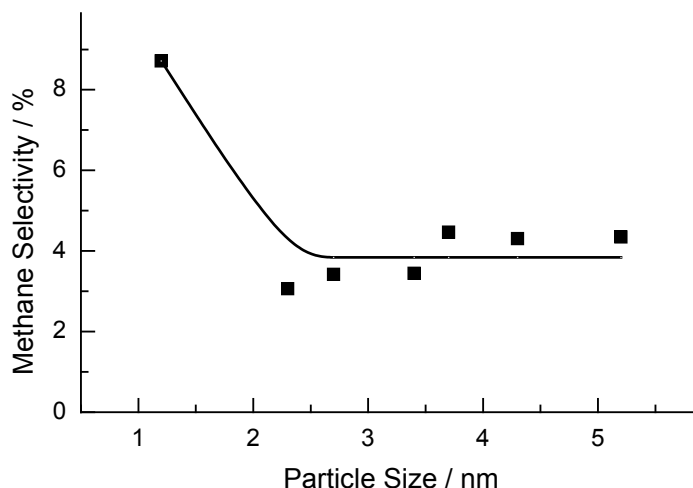


Figure 4.7: Effect of particle size on methane selectivity in FT reaction.

The surface atom normalized rates for hydrocarbon (TOF_{HC}) and oxygenate (TOF_{OXY}) formation as a function of the particle size are shown in Figure 4.6d. It can be seen that both TOFs increase with particle size. This trend is consistent with increasing step-edge density for larger particles. Figure 4.6c shows that, despite the increasing density of these sites for facile CO dissociation, the chain growth probabilities for hydrocarbons remain constant. A rationalization for this behaviour is that each site for CO dissociation is kinetically coupled to a chain growth site. Such a dual site model has been first proposed by Shetty et al. [54] and its kinetic implications have been recently developed [6]. It is also consistent with SSITKA experiments in which the residence time of CH_x species on the surface of a Ru catalyst was found to be independent of particle size [22]. Note that these latter measurements were carried out at temperatures where hydrocarbons formation is dominant. Since chain growth is predicted to be structure insensitive [55], a constant residence time for CH_x intermediates will lead to similar chain length and, hence, constant α_{HC} . Previous studies confirm that α_{HC} is independent of particle size for supported Ru and Co nanoparticle catalysts [41-42].

The kinetic observation for oxygenates formation are quite different from those for hydrocarbons formation. Two regions can be discerned. One with Ru nanoparticles in the range from 1 to 3 nm, and a second with Ru particles ranging from 3 to 5 nm. When the particle size is increased from 3 to 5 nm, TOF_{OXY} increases and α_{OXY} remains constant. This implies that more dissociated CO is converted into oxygenates, while the chain length

remains constant. This can be explained by an increase in the number of oxygenates growth sites. Similar to the hydrocarbons growth sites, each site for CO dissociation is coupled to one growth site for oxygenates formation for Ru particles larger than 3 nm. Since we have hypothesized that oxygenates are formed on planar sites with higher barrier for CO dissociation [27], the increase in TOF_{OXY} for Ru larger than 3 nm can be explained by the Ru particles having larger planar facets that accommodate more oxygenates growth sites. In contrast, increasing the Ru particle size from 1 to 3 nm (the first regime) results in an increasing TOF_{OXY} in parallel with an increasing α_{OXY} . This means that more and longer oxygenate chains are formed. This trend cannot be explained by an increase in the number of oxygenates growth sites only. The increase in α_{OXY} (Figure 4.6c) goes together with a decrease in the methane selectivity when the Ru particles size increases from 1 to 3 nm (Figure 4.7). We have earlier proposed that the sites for oxygenates formation are also favourable for methane formation due to the higher barrier for CO dissociation. The decrease in methane selectivity will lead to higher CH_x coverage near the oxygenates growth sites and, hence, more CH_x intermediates are available for oxygenates chain growth. Consequently, this leads to higher chain growth rate at the oxygenates growth sites and an increase in α_{OXY} .

4.4 Discussion

4.4.1 Effect of Temperature on FT Reaction

The anomalous trend of increasing α for oxygenates formation with temperature (Figure 4.4) is a consequence of the decreasing apparent activation barrier for CO dissociation [7-8], which effectively implies an increased apparent activation energy of chain growth versus that of chain termination. This can be deduced by deriving an expression for the chain growth probability.

By assuming that (i) O removal on the surface is fast and (ii) hydrogenation steps are implicit (e.g., C hydrogenation to CH_x) and assumed to be fast, the kinetic expression for CH_x coverage on the surface of the catalyst is defined as:

$$\frac{d\theta_{\text{CH}_x}}{dt} = r_{\text{CO diss}} - r_{\text{methane}} - \sum_{i=1}^{\infty} r_{\text{prop}}(C_i)$$

where $r_{\text{CO diss}}$ is the rate of CO dissociation, r_{methane} is the rate of methane formation and $r_{\text{prop}}(C_i)$ is the rate of propagation of a hydrocarbon chain C_i with chain length i to a hydrocarbon chain C_{i+1} with chain length $i + 1$.

Hence the steady state expression for CH_x coverage on the surface of the catalyst can be written as:

$$0 = k_{CO \text{ diss}} \cdot \theta_{CO} \cdot \theta_v - k_{meth} \cdot \theta_{CH_x} - k_{prop} \cdot \theta_{CH_x}^2 - k_{prop} \cdot \theta_{CH_x} \cdot \sum_{i=1}^{\infty} \theta_{C_i} \quad (4.1)$$

where $\theta_v = 1 - \theta_{CO} - \sum_{i=1}^{\infty} \theta_{C_i}$

Since the chain growth probability, α , is independent of chain length, $\alpha = \theta_{C_{i+1}} / \theta_{C_i}$ and

hence $\alpha^i = \theta_{C_{i+1}} / \theta_{CH_x}$. By applying Taylor approximation and $\theta_{C_{i+1}} = \theta_{CH_x} \cdot \alpha^i$,

$$\sum_{i=1}^{\infty} \theta_{C_i} = \sum_{i=0}^{\infty} \theta_{C_{i+1}} = \frac{\theta_{CH_x}}{1 - \alpha} \quad (4.2)$$

Substituting Eq. (4.2) into Eq. (4.1) gives

$$0 = k_{CO \text{ diss}} \cdot \theta_{CO} \cdot \left(1 - \theta_{CO} - \frac{\theta_{CH_x}}{1 - \alpha}\right) - k_{meth} \cdot \theta_{CH_x} - k_{prop} \cdot \theta_{CH_x}^2 \cdot \left(1 + \frac{1}{1 - \alpha}\right)$$

which can be further rewritten into

$$\theta_{CH_x} = \frac{(1 - \alpha) \cdot k_{CO \text{ diss}} \cdot \theta_{CO} \cdot (1 - \theta_{CO})}{k_{CO \text{ diss}} \cdot \theta_{CO} + (1 - \alpha) \cdot k_{meth} + k_{prop} \cdot \theta_{CH_x} \cdot (2 - \alpha)}$$

By assuming $k_{prop} \cdot \theta_{CH_x} \gg k_{CO \text{ diss}} \cdot \theta_{CO}$ and $k_{prop} \cdot \theta_{CH_x} \gg k_{meth}$ then the above equation can be simplified to

$$\theta_{CH_x} = \frac{(1 - \alpha) \cdot k_{CO \text{ diss}} \cdot \theta_{CO} \cdot (1 - \theta_{CO})}{k_{prop} \cdot \theta_{CH_x} \cdot (2 - \alpha)} \quad (4.3)$$

The classical expression for chain growth probability, α , is defined as [41]:

$$\alpha = \frac{k_{prop} \cdot \theta_{CH_x}}{k_{prop} \cdot \theta_{CH_x} + k_{term}} \quad (4.4)$$

By substituting Eq. (4.4) into Eq. (4.3) the following expression can be derived for θ_{CH_x} :

$$\theta_{CH_x} = \left(\frac{k_{term} \cdot k_{CO \text{ diss}} \cdot \theta_{CO} \cdot (1 - \theta_{CO})}{k_{prop}^2} \right)^{\frac{1}{3}} \quad (4.5)$$

Substituting Eq. (4.5) into Eq. (4.4), the will yield the following expression for α

$$\alpha = \left(1 + \left(\frac{k_{term}^2}{k_{prop} \cdot k_{CO\ diss} \cdot \theta_{CO} \cdot (1 - \theta_{CO})} \right)^{\frac{1}{3}} \right)^{-1} \quad (4.6)$$

Eq. (4.6) can be modified to describe the chain growth probability for oxygenates, α_{OXY} , by replacing k_{term} with $k_{term\ oxy} \cdot \theta_{CO}$. Hence

$$\alpha_{OXY} = \left(1 + \left(\frac{k_{term\ oxy}^2 \cdot \theta_{CO}}{k_{prop} \cdot k_{CO\ diss} \cdot (1 - \theta_{CO})} \right)^{\frac{1}{3}} \right)^{-1} \quad (4.7)$$

Table 4.2. Kinetic parameters to predict chain growth probabilities for oxygenates (OXY) and hydrocarbons (HC).		
Rate Constant	$A_o^{[a]}$ (s^{-1})	E_{act} (kJ/mol)
$k_{CO\ diss\ OXY}$	10^{13}	$110^{[d]}$
$k_{prop\ OXY}$	10^{13}	$60^{[c]}$
$k_{term\ OXY}$	10^{17}	$80^{[b]}$
$k_{CO\ diss\ HC}$	10^{13}	$50^{[f]}$
$k_{prop\ HC}$	10^{13}	$60^{[e]}$
$k_{term\ HC}$	10^{17}	$80^{[e]}$
[a] Pre-exponential factor taking into account partition functions of transition and ground states [30]. [b] From ref. [56]. [c] Since the chain growth was assumed to be faster than the termination step, the activation energy for chain growth was assumed to be lower than that for termination. [d] Values slightly lower than the energy calculated in Table 4.3 (sawtooth sites), to give α comparable to experimental values (Figure 4.4). [e] To make a meaningful comparison, the values used to model α_{OXY} will be used. [f] This work (Table 4.3, step-edge sites).		

The change in α_{OXY} with temperature was then modelled using Eq. (4.7) and the values used to compute the reaction rate constant are given in Table 4.2. The choice for the activation energies and pre-exponential factors is based on previously published DFT data [56] and entropy considerations accounting for partition functions of transition and ground states [30]. The surface CO coverage was estimated by a straightforward method using the Van 't Hoff equation and assuming θ_{CO} to be 0.8 at 130 °C with E_{CO}^{ads} of 130 kJ/mol. Figure 4.8 shows that α_{OXY} increases with temperature, similar to our experimental findings in Figure 4.4. Figure 4.8 also show that the values of $E_{CO\ diss}^{act}$, E_{prop}^{act} and E_{term}^{act} significantly

affect α_{OXY} . An increase in $E_{\text{CO diss}}^{\text{act}}$ and/or $E_{\text{prop}}^{\text{act}}$ leads to a decrease of α_{OXY} . Conversely, an increase in $E_{\text{term}}^{\text{act}}$ increases α_{OXY} . When $E_{\text{CO diss}}^{\text{act}} < E_{\text{prop}}^{\text{act}} < E_{\text{term}}^{\text{act}}$, the rate of CO dissociation is very fast and termination occurs very slowly. In this case, α_{OXY} approaches unity. However, when the rate of CO dissociation is high, the surface coverage of CO will be low and probability to terminate by CO insertion is low. In contrast, for $E_{\text{prop}}^{\text{act}} < E_{\text{term}}^{\text{act}} \ll E_{\text{CO diss}}^{\text{act}}$, there is insufficient CH_x for chain growth. In this particular case, even when termination is slow, α_{OXY} approaches 0. This implies that only methane and methanol will be formed. Based on this analysis, for the formation of long chain oxygenates we can conclude that $E_{\text{CO diss}}^{\text{act}}$ should not be too low to maintain sufficient CO on the surface near the oxygenates growth site for termination by CO insertion. High $E_{\text{CO diss}}^{\text{act}}$ has to be accompanied by low $E_{\text{prop}}^{\text{act}}$ and high $E_{\text{term}}^{\text{act}}$ to allow chain growth.

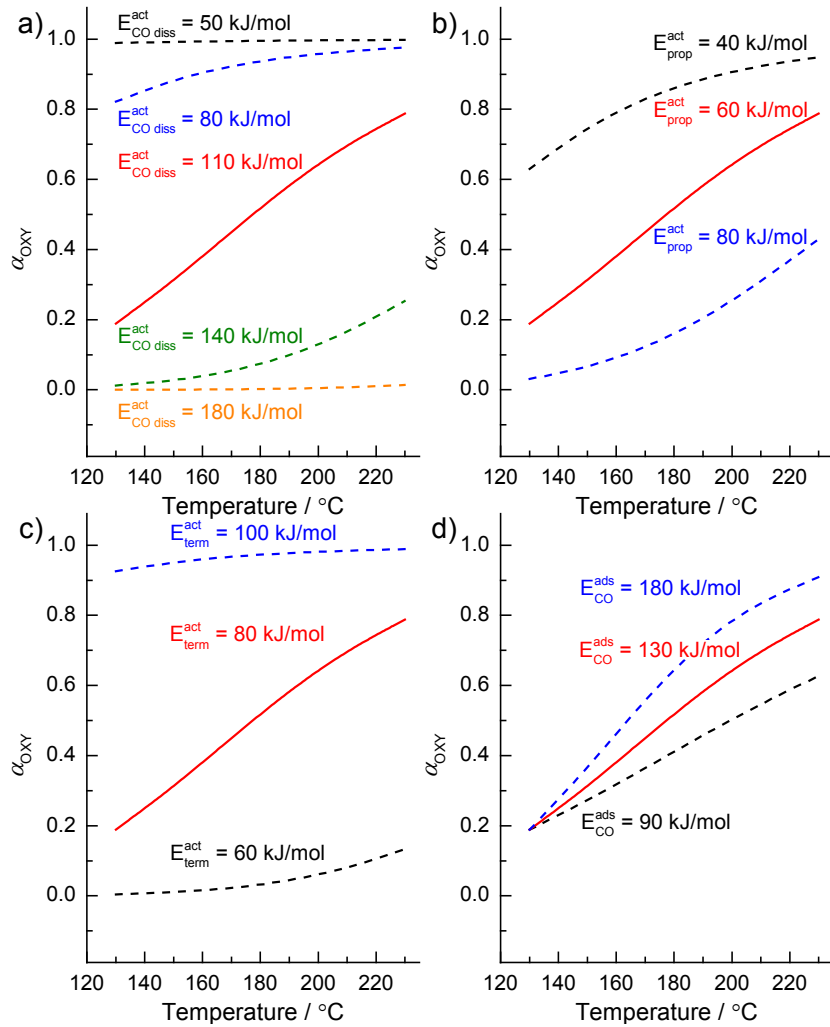


Figure 4.8: Simplified kinetics model for oxygenates chain growth probability with varying activation energy for (a) CO dissociation, (b) propagation, (c) termination, and (d) CO adsorption energy.

The change in α_{HC} is modelled using Eq. (4.6). To make a meaningful comparison, the values used to model α_{OXY} in Table 4.2 will be used, except that in this case $E_{\text{CO diss}}^{\text{act}}$ will be set at 50 kJ/mol. From Figure 4.9, the conventional dependence of decreasing α with increasing temperature is evident. This is in agreement with our results for α_{HC} in Figure 4.4 and also those reported in literature [41-42]. Similar to the trends mentioned for α_{OXY} , an increase in $E_{\text{CO diss}}^{\text{act}}$ and/or $E_{\text{prop}}^{\text{act}}$ decreases α_{HC} , and an increase in $E_{\text{term}}^{\text{act}}$ increases α_{HC} . Hence, to maintain high chain growth rates for hydrocarbons, $E_{\text{CO diss}}^{\text{act}}$ and $E_{\text{prop}}^{\text{act}}$ should be as low as possible and $E_{\text{term}}^{\text{act}}$ should be high.

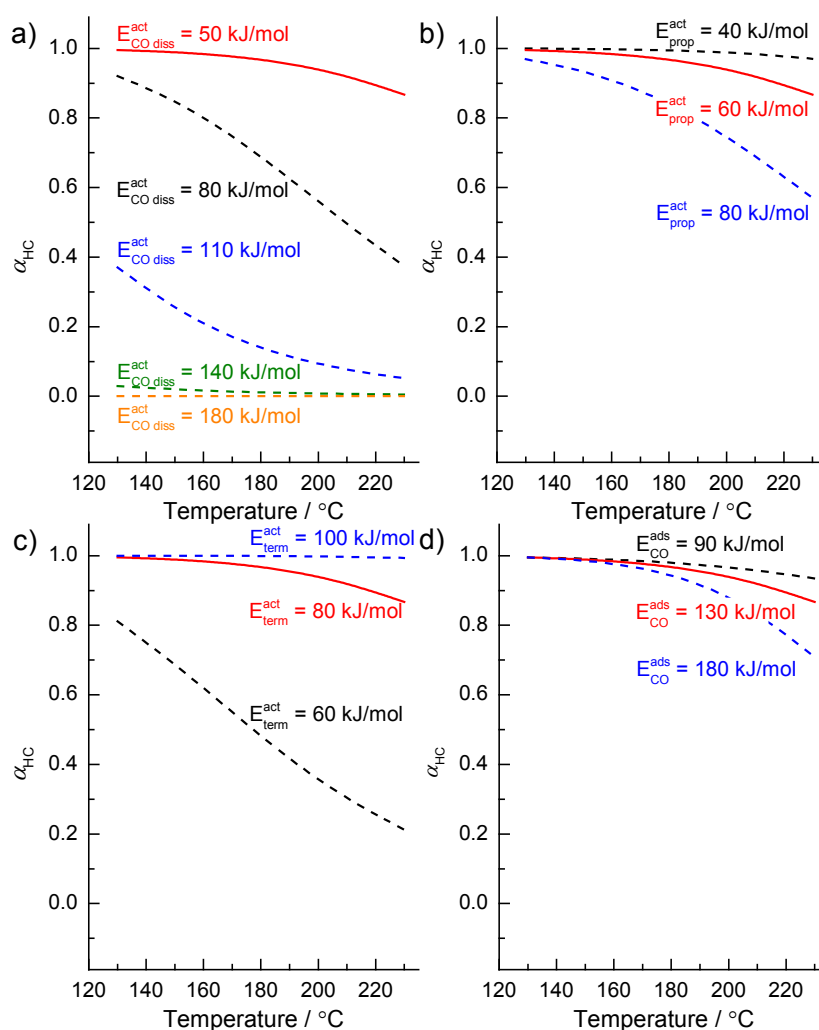


Figure 4.9: Simplified kinetics model for hydrocarbons chain growth probability with varying activation energy for (a) CO dissociation, (b) propagation, (c) termination, and (d) CO adsorption energy.

Figure 4.8d and 4.9d show that the change in $E_{\text{CO}}^{\text{ads}}$ affects α_{OXY} and α_{HC} very differently. Higher $E_{\text{CO}}^{\text{ads}}$ leads to higher α_{OXY} but lower α_{HC} . However, both for α_{OXY} and α_{HC} , higher $E_{\text{CO}}^{\text{ads}}$ leads to more rapid changes in α with temperature. This relates to the

dependence of the overall rate of CO dissociation on the desorption barrier of CO as observed from Eq. (4.8)

$$E_{app, CO\ diss}^{act} = E_{CO\ diss}^{act} - (1 - 2\theta_{CO}) \cdot E_{CO}^{ads} \quad (4.8)$$

On the oxygenates formation sites, the activation barrier for CO dissociation is high and θ_{CO} is also high. This means that in order for CO dissociation to occur a vacancy needs to be available requiring CO desorption. This will lead to $E_{app, CO\ diss}^{act} > E_{CO\ diss}^{act}$ when θ_{CO} approaches 1. Accordingly, higher CO adsorption energy will lead to higher $E_{app, CO\ diss}^{act}$, and the rate of CO dissociation will increase more rapidly with temperature, resulting in higher α_{OXY} . In contrast, on the hydrocarbons growth site where the barrier for CO dissociation is low and θ_{CO} is low, the adsorption of CO will lower $E_{app, CO\ diss}^{act}$. In this case, $E_{app, CO\ diss}^{act} < E_{CO\ diss}^{act}$, when θ_{CO} approach 0. Accordingly, higher CO adsorption energy will lead to lower $E_{app, CO\ diss}^{act}$, and the rate for CO dissociation will increase much slower compared the rate of termination with temperature resulting in lower α_{HC} .

Finally, it is important to consider that with increasing temperature the oxygenates (hydrocarbons) selectivity decreases (increases) (Figure 4.2). Overall, this implies that the apparent activation energy for oxygenates formation should be lower than that for hydrocarbons formation. The analysis above for the carbide mechanism implies that the rate controlling steps for formation of these two product classes are different. CO dissociation is controlling the rate for oxygenate formation, termination the rate of hydrocarbons formation. High chain growth probabilities are possible in both cases as long as the rate of chain growth is high. The apparent activation energy for CO dissociation will be strongly temperature dependent via the CO surface coverage. We did not discuss the possibility that, when CO surface coverage becomes lower at higher temperatures, the chains growing at the oxygenates growth sites will also terminate as hydrocarbons. Although this may be the case, the results for the experiments involving addition of 1-decene to the reaction mixture do not provide evidence that this is the case at 150 °C.

The anomalous temperature dependence of α_{OXY} is inconsistent with the alternative Pichler-Schulz CO insertion mechanism for chain growth. The expression for α according to the Pichler-Schulz mechanism is:

$$\alpha_{PS} = \frac{k_{prop} \cdot \theta_{CO}}{k_{prop} \cdot \theta_{CO} + k_{term}} \quad (4.9)$$

In contrast to Eq. (4.6), now k_{term} will always have a higher activation energy compared to the insertion of CO and the RC-O dissociation for high α .

From the methane selectivity (Figure 4.2b) and α_{OXY} (Figure 4.4), Ru-1.2 and Ru-5.2 behave differently. This indicates that the chemical nature of the active sites is different for these two catalysts. From the trends in Figure 4.2b and 4.4, two important observations are made, namely (i) constant methane selectivity for Ru-1.2 is accompanied by a steep increase in α_{OXY} , and (ii) increasing methane selectivity for Ru-5.2 is accompanied by gradual increase in α_{OXY} . These trends can be explained based on Eq. (4.1) and (4.4). Increasing methane selectivity with temperature for Ru-5.2 indicates methane formation has a higher barrier than for Ru-1.2, which becomes more important at high temperature for Ru-5.2. Based on Eq. (4.1), the consumption of CH_x towards methanation would result in less CH_x available for the C-C coupling chain growth step. Hence, when more CO dissociates for Ru-5.2 with increasing temperature, there would be an increase in competition for CH_x species between methanation and oxygenates chain growth. In comparison, for Ru-1.2, constant methane selectivity indicates that the relative rate of methanation remains unchanged. When more CH_x species are being formed, they are predominately being utilized for chain growth. Consequently, this leads to a more pronounced increase in α_{OXY} for Ru-1.2 compared to Ru-5.2. These results also imply that methane formation for Ru-1.2 is due the low rate of CO dissociation, but for Ru-5.2 methane formation is controlled by the activation energy for methanation. Another contributing factor to the faster increase in α_{OXY} could be the strength of CO adsorption. As observed from CO ATR-IR studies and the dependence of the surface coordination number on Ru nanoparticle size as determined by XRD-PDF, smaller particles will bind CO more strongly than larger ones. As discussed earlier and also shown Figure 4.8d, higher E_{CO}^{ads} will increase α_{OXY} more rapidly.

4.4.2 Structure-Activity Relationships

In an attempt to understand the unusual particle size dependence as shown in Figure 4.5, we correlated the FT activity to the structural data derived from the combination of XRD-PDF and RMC simulations presented in Chapter 3. The disorderliness increases with decreasing particle size. RMC simulations reveal that the structure of Ru-5.2 nanoparticles can be described by a *hcp* structure, whereas those of Ru-3.4 and Ru-3.7 are best represented by a *hcp*-type core and a disordered shell. In contrast, the structure of Ru-1.2 was found to be strongly distorted as compared to *hcp* and *fcc* structures. The activity of the catalyst with the

smallest particle size (Ru-1.2) is very low. Intermediate activities are observed for nanoparticles with a *hcp*-core-disordered-shell structure. The increase in FT activity above 4 nm is accompanied with the formation of *hcp*-ordered nanoparticles (Ru-5.2). A transition in structure between (partially) disordered and ordered nanoparticles around 4 nm was also reported by Bedford et al. [57]. The proposed relation between FT activity and 3D atomic arrangement of Ru draws similarity to previously reported observations for Co-*fcc* and Co-*hcp* nanoparticle catalysts for the FT reaction [24-25].

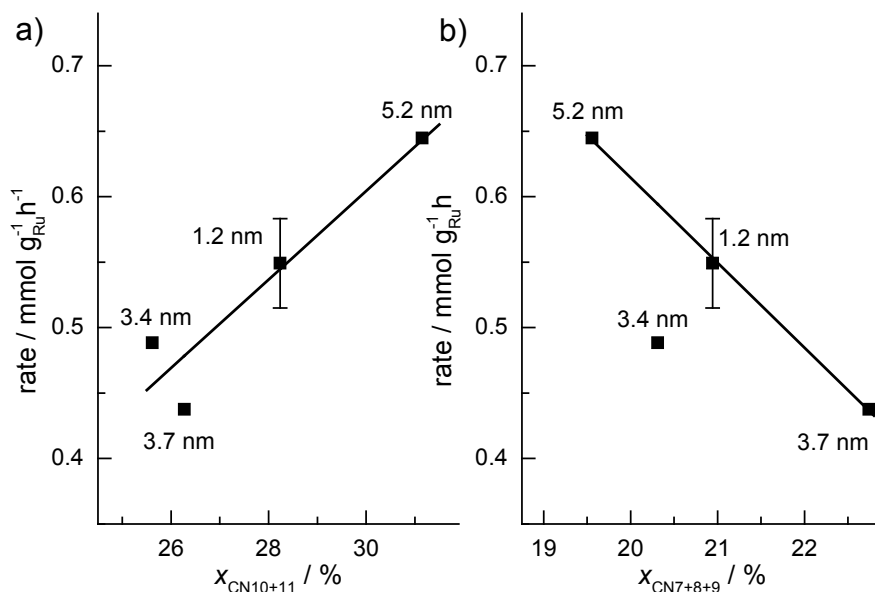


Figure 4.10: Weight-based rate for aqueous phase FT reaction correlated to the fraction of Ru atoms with (a) CN 10 and 11, and (b) CN 7, 8 and 9.

These considerations are only of qualitative nature. In an attempt to derive a quantitative correlation between the FT activity and catalyst structure, the fraction of step sites on the Ru particles was approximated from the fraction of metals atoms with coordination numbers (CN) of 10 and 11 in the RMC-generated average Ru particle representative models. We identify step-edge sites through the metals atom at the bottom of the step with CN of 10 or 11, which have a CN between bulk Ru (CN 12) and the maximum CN for a surface plane (CN 9). Figure 4.10a shows that the weight-based rate for aqueous-phase FT reaction increases linearly with the fraction of atoms with CN 10 and CN 11 on the particle ($x_{CN10+11}$). This results demonstrates clearly that the FT activity closely relates to the presence of surface atoms with CN of 10 and CN 11. Correlating the activity for aqueous-phase FT reaction to other CN's did not yield similar relationship except for the sum of fraction of Ru atoms with CN 7, 8 and 9 on the particle ($x_{CN7+8+9}$). Unlike the trend observed for CN 10 and 11, Figure 4.10b shows that the rate for FT is inversely proportional to the

fraction of Ru with CN 7, 8 and 9. This is consistent with the conclusion that the active sites are step-edge sites. Since atoms in a square-planar and close-packed surface have a CN of 8 and 9 respectively, we speculate that $x_{CN7+8+9}$ is an estimate for the fraction of planar sites. If this would be true, our results suggest that CO dissociation on planar sites has only a minor contribution to the overall FT activity.

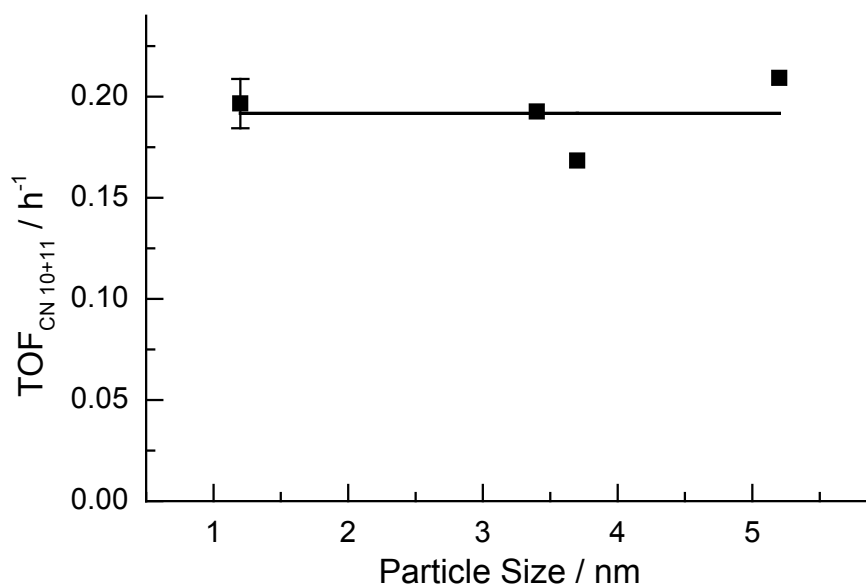


Figure 4.11: Influence of Ru particle size on activity for aqueous phase FT reaction normalized to the fraction of CN 10 and CN 11 atoms.

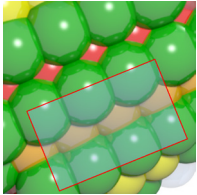
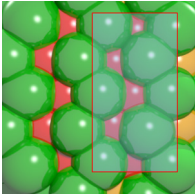
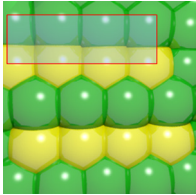
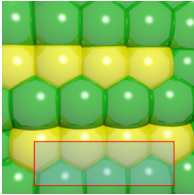
Figure 4.11 shows the TOF for aqueous phase FT normalized to $x_{CN10+11}$ ($TOF_{CN10+11}$) is independent to the change in Ru particle size. This implies that the change in FT activity with particle size observed in Figure 4.5 is mainly caused by the different concentration of sites with CN is 10 and 11. This implies that the chemical nature of the active sites for CO conversion remains unchanged for different particle sizes. In contrast, the variation in methane selectivity and α_{OXY} led us to propose before that the chemical nature of the active sites changes. Changes in the chemical nature of the active sites affect the C-C coupling and methane formation step but not the CO dissociation step in the FT reaction as follows from the constant $TOF_{CN10+11}$. According to the carbide mechanism, the overall consumption rate is determined by the rate of CO activation [30]. In the C-C coupling and methanation step, effects of coordinative saturation of the surface atoms are expected to be more dominant, since these reactions involve σ -bond formation or cleavage which occur over a single metal atom [55, 58]. However, for the CO dissociation involving activation of a π -bond, the geometric arrangement of the metal atoms, specifically their arrangement into step-edge sites, is more important [55, 58]. The change in particle size has a significant influence on the

coordinative unsaturation of the surface atoms, as supported by XRD-PDF and CO adsorption studies. In contrast, all nanoparticles contain the active step-edge sites for CO dissociation. Note that CO dissociation is not rate controlling except for oxygenate growth on the smallest particle size. Attempts to normalize the FT rate at 230 °C for Ru-1.2 and Ru-5.2 with $x_{CN10+11}$ did not result in reasonable correlations. Further studies have to be performed for more particle sizes at various temperatures to understand the temperature effect.

DFT calculations were performed for limited number of candidate sites on the RMC generated average particle representative model of Ru-5.2 in order to verify that atoms adjacent to CN 10 and 11 are able to dissociate CO with low barrier. The representative atomic arrangements are taken from RMC-refined average nanoparticle representative model given in Chapter 3 (Figure 3.7a).

Four typical candidate sites were identified: (i) step sites adjacent to atoms with CN 10 (B_5 sites), (ii) open surfaces neighbouring CN 11 (sawtooth sites), (iii) square planar sites, and (iv) close packed sites. DFT calculations were performed by first extracting and freezing different parts of the RMC generated Ru-5.2 model corresponding to the four candidate sites. The geometries of these sites were then optimized before studying CO dissociation. Table 4.3 summarizes the calculated barriers for CO dissociation on these sites. The B_5 and sawtooth sites exhibit relatively low barriers for CO dissociation of 49 and 135 kJ/mol, respectively. For the square planar and close-packed sites, the barriers for CO dissociation were found to be 174 and 232 kJ/mol, respectively. These calculations indicate that CO dissociation is possible on the B_5 and sawtooth sites, but not likely to occur on the square planar and close packed sites. These findings are in agreement with the trends for the FT reaction presented in Figure 4.10, where weight-based rate increases with $x_{CN10+11}$ but decreases with $x_{CN7+8+9}$.

Table 4.3. DFT calculated activation energy for CO dissociation on different sites identified on Ru-5.2 RMC model.^[a]

	B_5	Sawtooth	Square Planar	Close-Packed
				
$E_{CO\,diss}^{act}$	49 kJ/mol	135 kJ/mol	174 kJ/mol	232 kJ/mol
[a] DFT calculations were performed by first extracting parts of the RMC generated Ru-5.2 model (size roughly 1.5 nm, typically 150 atoms). In order to retain the original structure, part of the extracted structure was frozen during optimization.				

4.5 Conclusion

We have shown that in aqueous-phase FT the chain growth probabilities of oxygenates and hydrocarbons exhibit different trends with respect to temperature and particle size. This indicates that two different sites are responsible for their formation. With increasing temperature, the decrease in α_{HC} is consistent with the common notion in FT synthesis that the termination step is controlling the reaction rate. Conversely, increasing temperature leads to an increase in α_{OXY} . We propose that the increase in α_{OXY} is caused by the high apparent activation energy of CO dissociation, which is due to a high CO coverage. This essentially hinders CO dissociation, since the rate of chain termination by CO insertion is relatively fast. Results were analysed with a kinetic model and are consistent with the carbide mechanism. The increasing α_{OXY} and decreasing oxygenate selectivity with temperature cannot be explained within the Pichler-Schulz mechanism. An increase in Ru particle size leads to a decrease in the oxygenate selectivity, indicating that the relative ratio of oxygenates to hydrocarbons growth sites decreases. The kinetic parameters point to an increasing density of active sites for hydrocarbons and oxygenates formation with increasing particle size. The relative ratio of oxygenates to hydrocarbons growth sites becomes smaller for larger particles. Based on predicted surface topologies for the Ru nanoparticles, it is possible to correlate the FT rate to sites with geometries close to step-edge sites. These sites contain atoms with coordination numbers of 10 and 11. DFT calculations show that the local structure around such sites is conducive to low barrier CO dissociation. They represent amongst others step-edge sites at the surface of the nanoparticles. The FT rate normalized to the density of such sites is independent from particle size.

References

- [1] J. J. Spivey, A. Egbebi, *Chem. Soc. Rev.* **2007**, 36, 1514-1528.
- [2] E. van Steen, M. Claeys, *Chem. Eng. Technol.* **2008**, 31, 655-666.
- [3] A. Y. Khodakov, W. Chu, P. Fongarland, *Chem. Rev.* **2007**, 107, 1692-1744.
- [4] Q. Zhang, J. Kang, Y. Wang, *ChemCatChem* **2010**, 2, 1030.
- [5] B. H. Davis, *Ind. Eng. Chem. Res.* **2007**, 46, 8938-8945.
- [6] A. J. Markvoort, R. A. van Santen, P. A. J. Hilbers, E. J. M. Hensen, *Angew. Chem. Int. Ed.* **2012**, 51, 9015-9019.
- [7] R. A. van Santen, I. M. Ciobica, E. van Steen, M. M. Ghouri, *Adv. Catal.* **2011**, 54, 127-187.
- [8] R. A. van Santen, M. M. Ghouri, S. Shetty, E. J. M. Hensen, *Catal. Sci. Tech.* **2011**, 1, 891-911.
- [9] I. M. Ciobica, R. A. van Santen, *J. Phys. Chem. B* **2003**, 107, 3808-3812.
- [10] M. Ojeda, R. Nabar, A. U. Nilekar, A. Ishikawa, M. Mavrikakis, E. Iglesia, *J. Catal.* **2010**, 272, 287-297.
- [11] S. Shetty, A. P. J. Jansen, R. A. van Santen, *J. Am. Chem. Soc.* **2009**, 131, 12874-12875.
- [12] R. C. Brady, R. Pettit, *J. Am. Chem. Soc.* **1981**, 103, 1287-1289.
- [13] J. Gaube, H. F. Klein, *J. Mol. Catal. A: Chem.* **2008**, 283, 60-68.
- [14] H. Pichler, H. Schulz, *Chem. Ing. Tech.* **1970**, 42, 1162-1174.
- [15] B. H. Davis, *Catal. Today* **2009**, 141, 25-33.

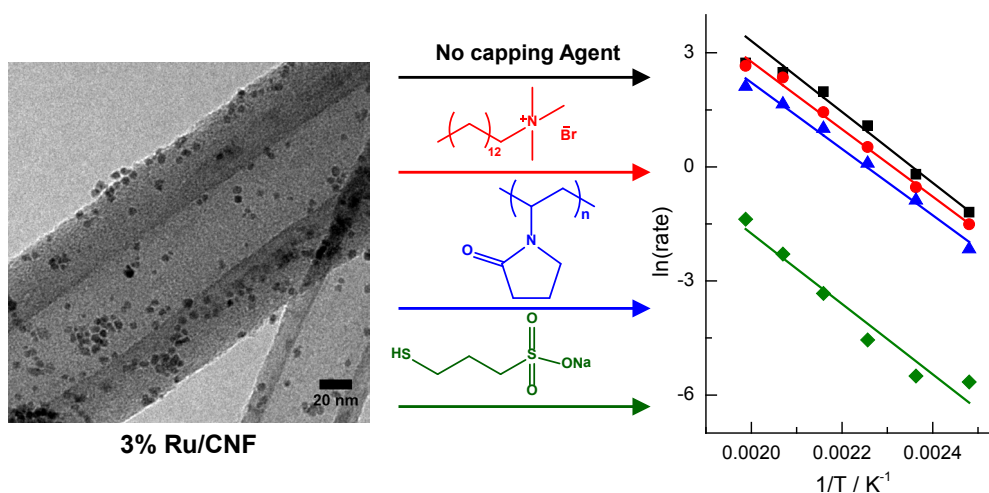
- [16] E. Iglesia, S. L. Soled, R. A. Fiato, *J. Catal.* **1992**, *137*, 212-224.
- [17] G. L. Bezemer, J. H. Bitter, H. Kuipers, H. Oosterbeek, J. E. Holewijn, X. D. Xu, F. Kapteijn, A. J. van Dillen, K. P. de Jong, *J. Am. Chem. Soc.* **2006**, *128*, 3956-3964.
- [18] O. Borg, P. D. C. Dietzel, A. I. Spjelkavik, E. Z. Tveten, J. C. Walmsley, S. Diplas, S. Eri, A. Holmen, E. Ryttera, *J. Catal.* **2008**, *259*, 161-164.
- [19] G. Prieto, A. Martínez, P. Concepción, R. Moreno-Tost, *J. Catal.* **2009**, *266*, 129-144.
- [20] J. P. den Breejen, P. B. Radstake, G. L. Bezemer, J. H. Bitter, V. Froseth, A. Holmen, K. P. de Jong, *J. Am. Chem. Soc.* **2009**, *131*, 7197-7203.
- [21] J. Kang, S. Zhang, Q. Zhang, Y. Wang, *Angew. Chem. Int. Ed.* **2009**, *48*, 2565-2568.
- [22] J. M. a. G. I. Carballo, J. Yang, A. Holmen, S. García-Rodríguez, S. Rojas, M. Ojeda, J. L. G. Fierro, *J. Catal.* **2011**, *284*, 102-108.
- [23] A. Tuxen, S. Carenco, M. Chintapalli, C.-H. Chuang, C. Escudero, E. Pach, P. Jiang, F. Borondics, B. J. Beberwyck, A. P. Alivisatos, G. Thornton, W.-F. Pong, J. Guo, R. Perez, F. Besenbacher, M. Salmeron, *J. Am. Chem. Soc.* **2013**, DOI: 10.1021/ja3105889.
- [24] D. I. Enache, B. Rebours, M. Roy-Auberger, R. Revel, *J. Catal.* **2002**, *205*, 346-353.
- [25] H. I. Karaca, O. V. Safonova, S. p. Chambrey, P. Fongarland, P. Roussel, A. Griboval-Constant, M. Lacroix, A. Y. Khodakov, *J. Catal.* **2011**, *277*, 14-26.
- [26] C. X. Xiao, Z. P. Cai, T. Wang, Y. Kou, N. Yan, *Angew. Chem. Int. Ed.* **2008**, *47*, 746-749.
- [27] X.-Y. Quek, Y. Guan, R. A. van Santen, E. J. M. Hensen, *ChemCatChem* **2011**, *3*, 1735-1738.
- [28] C. Wang, H. Zhao, H. Wang, L. Liu, C. Xiao, D. Ma, *Catal. Today* **2012**, *183*, 143-153.
- [29] J. J. F. Scholten, A. P. Pijpers, A. M. L. Hustings, *Cat. Rev. Sci. Eng.* **1985**, *27*, 151-206.
- [30] R. A. van Santen, A. J. Markvoort, M. M. Ghouri, P. A. J. Hilbers, E. J. M. Hensen, *J. Phys. Chem. C* **2013**.
- [31] Y.-W. Chen, J. Goodwin, Jr., *React. Kinet. Catal. Lett.* **1984**, *26*, 453-459.
- [32] E. Iglesia, S. C. Reyes, R. J. Madon, *J. Catal.* **1991**, *129*, 238-256.
- [33] R. J. Madon, S. C. Reyes, E. Iglesia, *J. Phys. Chem.* **1991**, *95*, 7795-7804.
- [34] J. G. Ekerdt, A. T. Bell, *J. Catal.* **1980**, *62*, 19-25.
- [35] L. Chen, Y. Zhu, H. Zheng, C. Zhang, Y. Li, *J. Chem. Technol. Biotechnol.* **2012**, *87*, 1089-1097.
- [36] L. Chen, Y. Zhu, H. Zheng, C. Zhang, B. Zhang, Y. Li, *J. Chem. Technol. Biotechnol.* **2012**, *87*, 112-122.
- [37] X. Y. Quek, Y. Guan, R. van Santen, E. Hensen, *ChemSusChem* **2010**, *3*, 1264-1267.
- [38] C. J. Weststrate, H. J. Gericke, M. W. G. M. Verhoeven, I. M. Ciobîcă, A. M. Saib, J. W. Niemantsverdriet, *J. Phys. Chem. Lett.* **2010**, *1*, 1767-1770.
- [39] R. Franke, D. Selent, A. Börner, *Chem. Rev.* **2012**, *112*, 5675-5732.
- [40] A. J. Bruss, M. A. Gelesky, G. Machado, J. Dupont, *J. Mol. Catal. A: Chem.* **2006**, *252*, 212-218.
- [41] G. P. Van der Laan, A. Beenackers, *Cat. Rev. Sci. Eng.* **1999**, *41*, 255-318.
- [42] R. A. Dictor, A. T. Bell, *J. Catal.* **1986**, *97*, 121-136.
- [43] R. van Hardeveld, A. van Montfoort, *Surf. Sci.* **1966**, *4*, 396-430.
- [44] K. Honkala, A. Hellman, I. N. Remediakis, A. Logadottir, A. Carlsson, S. Dahl, C. H. Christensen, J. K. Nørskov, *Science* **2005**, *307*, 555-558.
- [45] M. P. Andersson, E. Abild-Pedersen, I. N. Remediakis, T. Bligaard, G. Jones, J. Engbæk, O. Lytken, S. Hørch, J. H. Nielsen, J. Sehested, J. R. Rostrup-Nielsen, J. K. Nørskov, I. Chorkendorff, *J. Catal.* **2008**, *255*, 6-19.
- [46] G. A. Morgan, D. C. Sorescu, T. Zubkov, J. T. Yates, *J. Phys. Chem. B* **2004**, *108*, 3614-3624.
- [47] C. Strebel, S. Murphy, R. M. Nielsen, J. H. Nielsen, I. Chorkendorff, *PCCP* **2012**, *14*, 8005-8012.
- [48] R. M. Nielsen, S. Murphy, C. Strebel, M. Johansson, I. Chorkendorff, J. H. Nielsen, *J. Nanopart. Res.* **2010**, *12*, 1249-1262.
- [49] A. M. Karim, V. Prasad, G. Mpourmpakis, W. W. Lonergan, A. I. Frenkel, J. G. Chen, D. G. Vlachos, *J. Am. Chem. Soc.* **2009**, *131*, 12230-12239.
- [50] G. A. Somorjai, K. S. Hwang, J. S. Parker, *Top. Catal.* **2003**, *26*, 87-99.
- [51] J. J. C. Geerlings, J. H. Wilson, G. J. Kramer, H. Kuipers, A. Hoek, H. M. Huisman, *Appl. Catal. A* **1999**, *186*, 27-40.
- [52] J. Wilson, C. Degroot, *J. Phys. Chem.* **1995**, *99*, 7860-7866.
- [53] G. A. Beitel, C. P. M. de Groot, H. Oosterbeek, J. H. Wilson, *J. Phys. Chem. B* **1997**, *101*, 4035-4043.
- [54] S. G. Shetty, I. M. Ciobica, E. J. M. Hensen, R. A. van Santen, *Chem. Commun.* **2011**, *47*, 9822-9824.
- [55] R. A. van Santen, *Acc. Chem. Res.* **2009**, *42*, 57-66.
- [56] I. A. W. Filot, E. J. M. Hensen, R. A. van Santen, **2013**, in preparation.
- [57] N. Bedford, C. Dablenmont, G. Viau, P. Chupas, V. Petkov, *J. Phys. Chem. C* **2007**, *111*, 18214-18219.
- [58] R. A. van Santen, M. Neurock, S. G. Shetty, *Chem. Rev.* **2010**, *110*, 2005-2048.

Chapter 5

Effect of the Organic Capping Agent on Ru-Nanoparticle Catalyzed Aqueous Phase Fischer-Tropsch Synthesis

Summary

The influence of the organic capping agent on the performance of Ru nanoparticles in aqueous phase Fischer-Tropsch synthesis was investigated. The three organic capping agents used were trimethyl(tetradecyl)ammonium bromide (TTAB), polyvinylpyrrolidone (PVP) and sodium 3-mercapto-1-propanesulfonate (SMPS). To exclude effects of particle size, the capping agents were placed on carbon nanofiber supported Ru nanoparticles of 3.4 nm. The activity in the FT reaction increases in the order Ru-SMPS \ll Ru-PVP $<$ Ru-TTAB $<$ Ru. Kinetic data suggest that the FT mechanism is largely unaffected by the presence of capping agents, so that their binding to active centers can explain the activity trends. It is also found that replacing water with n-hexadecane as the solvent results in an increase of the rate of formation and a decrease in the chain growth probability for hydrocarbons, whilst the oxygenates production is unaffected. This trend is consistent with the proposal that hydrocarbons are formed on reaction centers involving facile CO dissociation and termination being rate controlling. For oxygenates, CO dissociation is proposed to be the rate controlling step.



5.1 Introduction

Recent advancements in nanoscience allows more effective control of the size and morphology of metallic nanoparticles with potential applications in the field of catalysis [1-8]. Due to the well-defined structure of these colloidal nanoparticles, they are commonly applied as model catalysts to investigate the intrinsic effect of structure on catalytic behaviour. An additional advantage is that the effect of the support can be excluded. In the absence of a carrier material to prevent particle aggregation, colloidal nanoparticle catalysts are usually stabilized by organic capping agents. It is known that the type of organic capping agent can influence the size and shape of the nanoparticles, likely because their growth behaviour is different [7-11]. Evidently, the presence of these organic capping agents on the surface of the particles will affect their catalytic behaviour. Previous studies have found that activities tend to decrease with an increase of the coordination strength of organic capping agents with the metal surface. Examples are available for hydrogenation [12-14], CO oxidation [12, 15] and Suzuki coupling reactions [16-18]. In addition, several studies have shown that removal of the organic capping agent results in an increase of the catalytic activity for CO oxidation [15] and hydrogenation reactions [19]. The use of different organic capping agent may also affect the selectivity in catalytic reactions [20]. For instance, the carbon chain length of the organic capping agent used to prepare bimetallic PtCo nanoparticles dictates the hydrogenation of C=C or C=O bond on cinnamaldehyde and citral [20]. However, many of these studies used different organic capping agent during the synthesis of the nanoparticles [13, 15-18, 20], and activity differences cannot be solely attributed to the effect of the organic capping agent.

An important example of a chemical reaction catalyzed by metal nanoparticles is the Fischer-Tropsch (FT) reaction. In FT synthesis reaction, syngas (a mixture of CO and H₂) is converted into hydrocarbons. Co, Fe and Ru are the typical transition metals that catalyze the FT reaction to produce long chain hydrocarbons [21-23]. On metals such as Rh and Cu where the barrier for CO dissociation is higher, oxygenates are formed [24]. Two main opposing mechanisms have been proposed to rationalize the formation of hydrocarbons and oxygenates in the FT reaction [25]. The mechanism most supported by scientific literature is the carbide mechanism. This mechanism comprises three main steps and assumes surface CH_x to be building block for chain growth [25]. The first step involves the dissociation of CO to form CH_x species, then chain growth proceeds via insertion of CH_x followed by termination of the growing chain to form the final product. In the carbide mechanism, the termination step will

determine the type of product being formed. Termination by H-addition or β -H elimination leads to the formation of hydrocarbons, while termination by CO insertion leads to the formation of oxygenates. An alternative mechanism is the CO-insertion mechanism proposed by Pichler and Schulz [26-27]. In this mechanism, CO is the building block, which is inserted into the growing chain. The subsequent step involves a competition between (i) termination to oxygenates, and (ii) the dissociation of the C-O bond in the intermediate for further chain growth or termination as a hydrocarbon.

Although industrial FT catalysts are usually metal nanoparticles dispersed on a support, the application of colloidal nanoparticles catalyst has also been demonstrated [28-34]. Kou and co-worker pioneered the study of FT reaction using colloidal nanoparticles in a batch reactor leading to formation of long-chain hydrocarbons [28-29]. We have recently performed similar experiments using colloidal Ru nanoparticles and found that the product mixture also contains a significant fraction of long-chain oxygenates [33-34]. Exceptionally high selectivity towards long chain oxygenates (aldehydes and alcohols) was observed at low temperatures [33-34]. Based on trends for chain growth probability for hydrocarbons (α_{HC}) and oxygenates (α_{OXY}), we have proposed that hydrocarbons and oxygenates are formed on different catalytic sites. Hydrocarbons are argued to be formed on sites with low barrier for CO dissociation, whereas oxygenates are postulated to be formed on sites with higher barrier for CO dissociation. We have excluded the contribution of oxidic Ru species and/or promoters (such as Na and B), which might have favoured the formation of oxygenates [33]. However, the influence of the organic capping agent on the colloidal Ru particles and the reaction solvent in the formation of oxygenates was not determined yet.

In the present study, we evaluate the influence of different water-soluble organic capping agents on Ru nanoparticles used for the aqueous phase FT reaction. The results will be compared to a Ru reference catalyst without capping agent. Previous studies investigating the effect of organic capping agents have varied the capping agent during the synthesis of the metal particles [13, 15-18]. This will strongly affect the size and morphology of the nanoparticles. This is a problem for the FT reaction which is strongly structure sensitive, especially when the metal particles are smaller than 10 nm [35-37]. In order to ensure a systematic evaluation of the capping agent, our approach is to first prepare uniformly sized Ru nanoparticles on carbon nanofibers (CNF) by the polyol reduction method, followed by adsorption of different organic capping agents. This approach will also avoid the need to remove the organic capping agent from the Ru particles for comparison with the bare Ru

catalyst. A cumbersome method to remove organic capping agents is by UV-ozone treatment [38-40], which does not guarantee complete removal of the capping agent. The three different water soluble organic capping agents used in this study are trimethyl(tetradecyl)ammonium bromide (TTAB), polyvinylpyrrolidone (PVP) and sodium 3-mercapto-1-propanesulfonate (SMPS). The effect of the reaction solvent used in liquid phase FT reaction will also be studied.

5.2 Experimental Methods

5.2.1 Synthesis of Materials

Carbon nanofibers (>98%, Aldrich) were treated in concentrated nitric acid (65%, Merck) to remove amorphous carbon and metal impurities and to introduce surface functional groups, which facilitate the interaction between the metal precursor and the support [41]. 6 g of CNF and 600 ml of nitric acid was refluxed at 110°C for 2 h. The treated CNF was then filtered, washed with deionized water and dried overnight at 110°C.

A 3% Ru/CNF catalyst was prepared by liquid phase reduction with 1,4-butanediol, similar to a previously published procedure used to prepare colloidal Ru nanoparticles [34]. 0.485 g of dried CNF was added to 23.5 ml of 1,4-butanediol. The mixture was sonicated for 10 min to form a homogeneous suspension. 60 mg of ruthenium (III) acetylacetonate ($\text{Ru}(\text{acac})_3$, Alfa Aesar) dissolved in 1.5 ml of THF and 1.5 ml of 1,4-butanediol were added dropwise to the CNF suspension under vigorous stirring. The catalyst was reduced by heating the mixture to 170°C and refluxed under N_2 flow for 4 h. After reduction, the catalyst was filtered, washed with deionized water and dried overnight at 110°C. This bare 3% Ru/CNF is denoted as Ru-CNF.

TTAB, PVP and SMPS was deposited onto the bare Ru-CNF (denoted as Ru-TTAB, Ru-PVP and Ru-SMPS respectively) with a capping agent to Ru molar ratio of 50. To this end, the dried Ru-CNF and the organic capping agent were dispersed in deionized water by sonication for 10 min. The resultant mixture was then stirred at 80°C for 24 h. The catalyst was then recovered by filtration, washing and drying overnight at 110°C.

5.2.2 Characterization

The Ru loading on the catalyst was determined by inductively coupled plasma atomic emission spectroscopy (ICP-AES) analysis performed on a Goffin Meyvis SpectroCirus

apparatus. A small amount of sample was melted with KNO_3 and KOH . The melt was then dissolved in 2 M KOH and then diluted in HCl solution.

Transmission electron micrographs (TEM) were made with a FEI Tecnai 20 electron microscope equipped with a LaB_6 filament and operating at an acceleration voltage of 200 kV. A small amount of the nanoparticles was mixed with ethanol, dispersed over a carbon-coated Cu grid and finally dried in air. The average particle size and the standard deviation were determined by analysing at least 150 particles.

X-ray photoelectron spectrometer (XPS) spectra were measured with a Thermo Scientific K-Alpha XPS equipped with a monochromatic $\text{Al K}\alpha$ X-ray. For survey and region scans, constant pass energies of 160 eV and 40 eV, respectively, were used. The background pressure was $2 \cdot 10^{-9}$ mbar. Fitting was carried out with the CasaXPS program.

5.2.3 Catalytic Activity Measurements

Prior to reaction, 100 mg of catalyst was dispersed in 3 mL of solvent, sonicated for 10 min and re-reduced in a 10 mL stainless steel autoclave at 150°C with 20 bar H_2 for 2 h under vigorous stirring. Deionized water was used as the solvent for all experiments except in the investigation of solvent effect, where n-hexadecane was used instead. After reduction, the autoclave was cooled to room temperature in an ice bath before releasing the pressure. The liquid phase FT reaction was carried out at 30 bar for 24 h in the same autoclave. The autoclave was flushed 3 times with CO , before being pressurized with CO followed by H_2 to 30 bar (molar ratio $\text{H}_2/\text{CO} = 2$). The autoclave was sealed and the autoclave body was heated to the reaction temperature with a band heater controlled by a temperature controller. After 24 h, the reaction was terminated by immersing the autoclave into an ice bath.

The gas phase products were analysed with an Interscience Compact GC system, equipped with an $\text{Al}_2\text{O}_3/\text{KCl}$ column and a flame ionization detector (FID). For analysis, the gas cap was flushed through a 6-way valve allowing injection onto a gas chromatograph. Methane, ethane, ethylene, propane and propylene were analysed against a standard gas mixture. For analysis of the liquid phase, an extraction was carried out with diethyl ether containing *p*-cymene as an internal standard. The organic phase containing the products was then analysed with a GC (QP5050, Shimadzu) equipped with a Rxi-5ms capillary column ($30 \text{ m} \times 0.25 \text{ mm} \times 0.5 \text{ }\mu\text{m}$) and a flame ionization detector (FID). Identification and quantification of linear alkanes (C_6 to C_{16}), alcohols (C_4 to C_{12}) and aldehydes (C_4 to C_{12}) was established with reference compounds and *p*-cymene as the internal standard. The identity of

the products was also verified with a GC-MS equipped (GC-MS, QP5050, Shimadzu) with a Rxi-5ms capillary column.

The rate of the FT reaction (r) and selectivity were calculated based on the number of moles of carbon being formed in the products according to the following formula:

$$r = \frac{\text{total mol C formed in all products}}{\text{mass of Ru} \times \text{reaction time}}$$

$$\text{Selectivity to hydrocarbon or oxygenate} = \frac{\sum(\text{mol of } C_n^{\text{HC/oxy}} \times n)}{\text{total mol C formed as products}}$$

5.3 Results and Discussion

5.3.1 Catalytic Activity Measurements

Figure 5.5.1a shows a representative TEM micrograph for Ru-CNF. The average particle size for Ru-CNF is 3.4 nm. The Ru particles are homogeneously dispersed over the CNF surface. The average particle size is very similar to the particle size when they are prepared in the presence of PVP under otherwise similar conditions [34]. Analysis of TEM micrographs for Ru-TTAB (Figure 5.1b), Ru-PVP (Figure 5.1c) and Ru-SMPS (Figure 5.1d) show that introducing the organic capping agent to Ru-CNF does not result in changes in the particle size. The average particle sizes and standard deviations for all catalyst are summarized in Table 5.1.

Table 5.1. Properties of 3% Ru/CNF nanoparticles catalyst. ^[a]			
Notation	Capping Agent	$d_p^{[b]}$ (nm)	Loading ^[c]
Ru-CNF	-	3.4 ± 0.7	$2.8 \pm 0.1\%$
Ru-TTAB	TTAB	3.4 ± 0.7	$2.8 \pm 0.1\%$
Ru-PVP	PVP	3.2 ± 0.8	$2.7 \pm 0.1\%$
Ru-SMPS	SMPS	3.2 ± 0.6	$2.0 \pm 0.1\%$
[a] Ru supported on CNF was prepared by polyol reduction of Ru(acac) ₃ in the presence of CNF at 175°C. Organic capping agents were introduced in a subsequent step onto this Ru/CNF catalyst. [b] Average particle sizes and the standard deviations were calculated by measuring at least 150 particles. [c] Determined from ICP-AES.			

Table 5.1 also lists the Ru loading determined by ICP-AES analysis. The metal loading for Ru-CNF was found to be 2.8%. The introduction of the organic capping agent did not change the Ru content for Ru-TTAB and Ru-PVP, but the loading with Ru-SMPS led to a slight decrease of the metal loading to 2%. This is probably caused by the strongly

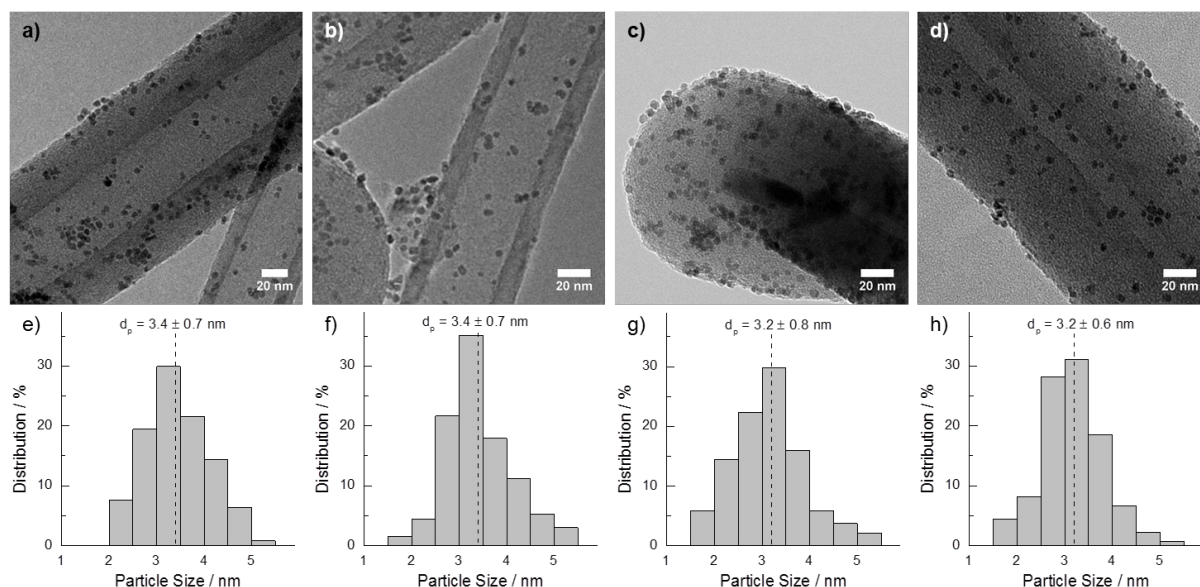


Figure 5.1: Electron micrographs (a-d) and particle size distributions (e-h) for Ru-CNF (a, e), Ru-TTAB (b, f), Ru-PVP (c, g), and Ru-SMPS (d, h).

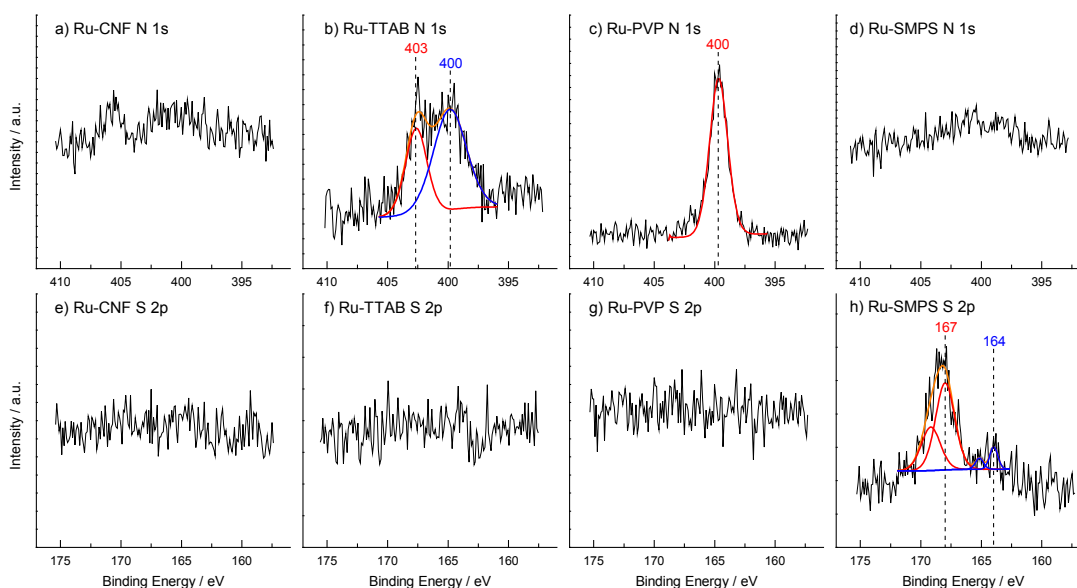


Figure 5.2: X-ray photoelectron spectra in the N 1s (a-d) and S 2p (e-h) regions for Ru-CNF (a, e), Ru-TTAB (b, f), Ru-PVP (c, g), and Ru-SMPS (d, h).

coordinating nature of the sulphur containing groups on the SMPS capping agent, which results in some Ru leaching during the washing step.

In order to verify that the capping agent was introduced onto the catalyst, X-ray photoelectron (XP) spectra of the modified catalysts were recorded. Figure 5.2 shows that no peaks were observed in the N 1s region for Ru-CNF and Ru-SMPS. For the Ru-TTAB, two peaks were observed in the N 1s region. Previous studies have also identified two peaks of

which one is assigned to TTAB with the ammonium group pointing towards the particle surface and the other peak to an ammonium group pointing away from the surface [42]. Since the N 1s peak for ammonium salts is reported to be between 401 to 403 eV, the peak at 403 eV most likely corresponds the ammonium group pointing away from the surface of the Ru particle. In contrast, for Ru-PVP only one peak is observed in the N 1s region. Expectedly, the XP spectra do not show observable peaks in the S 2p region for Ru-CNF, Ru-TTAB and Ru-PVP. For Ru-SMPS, two peaks are seen for S 2p_{3/2}, which corresponds to the thiol (164 eV) and sulfonate (167 eV) groups. From these results, we can conclude that TTAB, PVP and SMPS have been successfully introduced and remained on the Ru/CNF surface after washing. The modification of the Ru nanoparticles with these capping agents does not result in significant changes in the Ru particle size. Hence, these catalyst can be used to investigate the effect of the organic capping agent on the FT reaction without having to take into account changes in the Ru particle size.

5.3.2 Effect of Organic Capping Agent

Figure 5.3a shows the effect of the organic capping agent on the FT rate for Ru nanoparticles as a function of temperature. The FT rate increases exponentially for all catalyst, except for Ru-SMPS where the increase in activity was too low to be reflected in the plot. Typically, the FT rate decreases in the order Ru-CNF > Ru-TTAB > Ru-PVP >> Ru-SMPS. This decreasing trend is attributed to the increasing interaction of the organic capping agent with the Ru particles surface. SMPS interacts strongly with the surface of the Ru particles through the thiol and sulfonate groups forming strong metal-sulphur bond and metal-sulfonate bonds. These groups poison the catalyst surface. This is consistent with the notion that sulphur is a significant poison to FT catalysts [43-44]. It is usually assumed that PVP interacts with the surface of metal nanoparticles through the carbonyl group [45], while TTAB interacts with such surfaces via the ammonium cation [46]. Clearly, the effect of PVP on the FT rate is stronger than that of TTAB. The higher FT activity for Ru-TTAB compared to the other capping agents may be linked to the relatively weak binding between TTAB and Ru [12, 15]. It might also be that less sites are being blocked by TTAB than in the case of PVP because more capping agent has been removed by washing. It is still observed that the activity of Ru-TTAB is lower than that of the parent Ru-CNF.

Figure 5.3b shows that the apparent activation energy for the FT reaction remains unaffected upon varying the capping agent. Apparent activation energy for the FT reactions were found to be 77 (Ru-CNF), 74 (Ru-TTAB), 73 (Ru-PVP) and 77 (Ru-SMPS) kJ/mol.

This suggests that the mechanism for FT does not change by addition/variation of the organic capping agent to the Ru nanoparticles. In addition, it can be said that the binding of the organic capping agent to the surface of the Ru nanoparticles did not impose any possible effects such as of electronic nature. The difference between Ru-CNF, Ru-TTAB, Ru-PVP and Ru-SMPS is caused by the extent to which the capping agents hinder adsorption of reactants on the active sites. This is influenced by the strength of interaction between the capping agent and the Ru particles. In contrast to the studies by Park et al.[15] where different organic capping agents were found to change the activity by less than 30% for CO oxidation, our studies showed that FT activity for Ru-SMPS is more than 90% lower than Ru-CNF at 230°C.

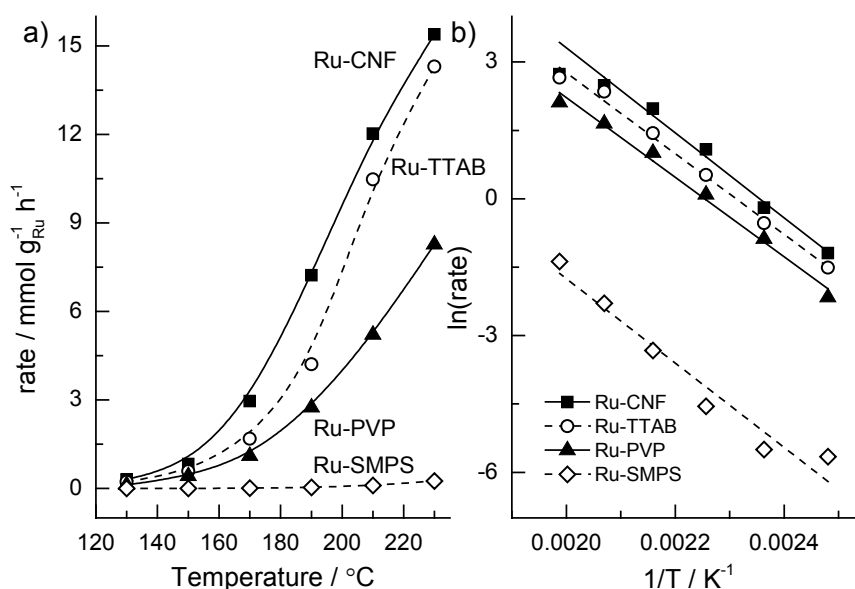


Figure 5.3: Effect of reaction temperature on Ru/CNF for various capping agents in the FT reaction, with H_2/CO ratio of 2 and 3 ml of H_2O : (a) rate and (b) Arrhenius plot.

Figure 5.4 shows that oxygenates selectivity decreases with temperature for all catalysts. This result is in agreement with our previous studies using PVP-stabilized colloidal Ru particles [33-34]. We have proposed that the temperature dependence of oxygenates selectivity relates to either (i) different CO activation barriers of the respective sites that form preferentially oxygenates or hydrocarbons and/or (ii) the activation energy for termination to hydrocarbons is higher than that to form oxygenates [34]. Ru-CNF, Ru-TTAB and Ru-PVP exhibit very similar oxygenates and hydrocarbons selectivity trends. However, Ru-SMPS gave much lower oxygenates selectivity compared to the other catalysts. At 170°C, Ru-SMPS did not produce any oxygenates, while oxygenates selectivity was still above 40% at this temperature for the other catalysts. It is also seen that oxygenates selectivity decreases with

increasing strength of interaction between the organic capping agent and the Ru particles (Ru-TTAB > Ru-PVP > Ru-SMPS). A very straightforward explanation is that CO has to compete with the capping agent for adsorption on the Ru nanoparticles. With lower CO coverage, the rate of CO termination will be decreased and hence oxygenates selectivity.

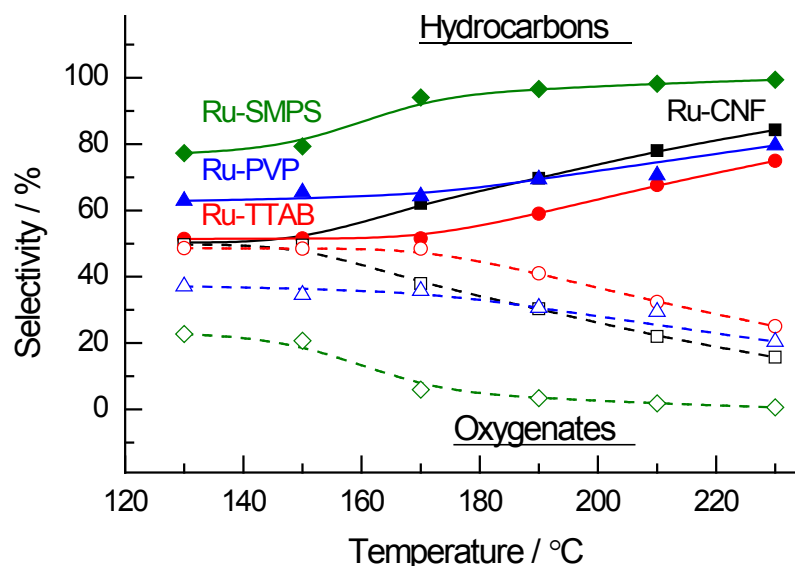


Figure 5.4: Effect of reaction temperature on the hydrocarbons and oxygenates selectivity in FT reaction, with H_2/CO ratio of 2 and 3 ml of H_2O , for Ru/CNF containing different capping agents.

The effect of temperature on the chain growth probabilities for hydrocarbons (α_{HC}) and oxygenates (α_{OXY}) are shown in Figure 5.5a and 5b, respectively. It is important to note that similar to our earlier work, different trends for α_{HC} and α_{OXY} are found [33-34]. This difference is attributed to the presence of different reaction centers for formation of oxygenates and hydrocarbons on the Ru nanoparticle surface [33-34]. We have proposed that hydrocarbons are formed on sites with low barrier for CO dissociation, whereas oxygenates are formed on sites with high barrier for CO dissociation [33-34]. Figure 5.5a shows that when the reaction temperature is increased from 130 to 230°C, α_{HC} decreases for Ru-CNF and Ru-TTAB. The values are always higher than 0.8, even at the highest temperature of 230°C. This behaviour is in line with literature [47-48] and consistent with the higher activation energy for chain termination compared to the one for chain growth [25, 49]. α_{HC} for Ru-SMPS did not decrease with temperature and was found to be much lower than α_{HC} for the other catalysts. Mainly, short chain hydrocarbons with less than 7 carbon atoms were formed in this case. The low hydrocarbon chain growth probability for Ru-SMPS can be due to (i) low chain growth rate or (ii) high termination rate. It is not likely that in the presence of a capping agent, the rate of termination is increased so that it is reasonable to conclude that

the rate of chain growth has been significantly decreased by the presence of SMPS. This may be due to poisoning of the active sites for CO dissociation, which reduces the rate of formation of the CH_x intermediates causing a low rate of chain growth. The α_{HC} trend for Ru-PVP is very different compared to the other catalysts. For Ru-PVP, α_{HC} increases from 130 to 185°C contrary to the trend for Ru-CNF and Ru-TTAB, and decreases with further temperature increase. The decrease in α_{HC} when temperature increases for Ru-CNF, Ru-TTAB and for Ru-PVP above 185°C is in agreement with the higher activation energy for chain termination compared to that for chain growth. The increase in α_{OXY} is explained by the low rate of CO dissociation [33-34]. Therefore, we argue that possibly the different behaviour is due to PVP blocking the active centers for CO dissociation of the hydrocarbons formation sites. This inhibiting effect diminishes with increasing temperature, because of desorption of PVP from these surface sites. It should be noted that the increase in α_{HC} below 185°C was not observed in our previous study [33]. The main difference with the present work is the much higher PVP/Ru ratio of 50 employed here than before [33-34].

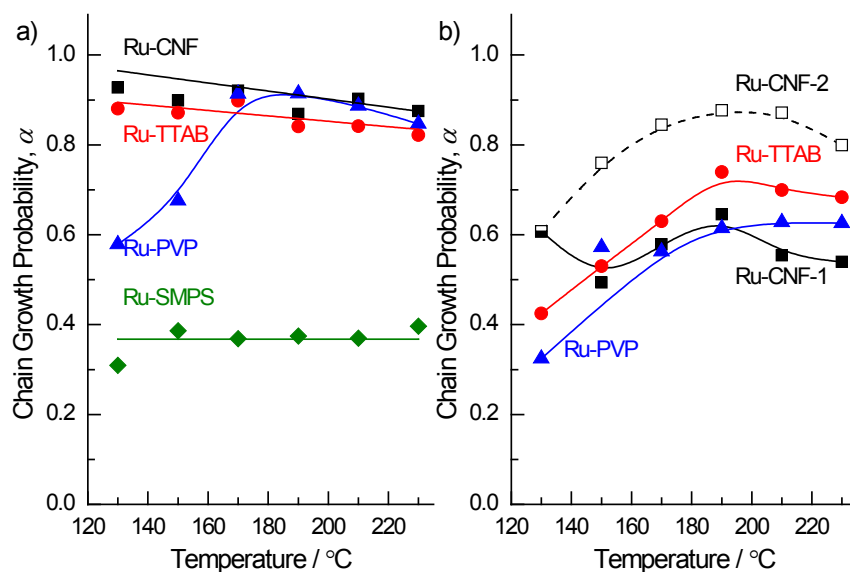


Figure 5.5: Effect of reaction temperature on the chain growth probability in the FT reaction, with H_2/CO ratio of 2 and 3 ml of H_2O , for: (a) Hydrocarbons and (b) Oxygenates.

Figure 5.5b shows that oxygenates chain growth probabilities (α_{OXY}) increases with temperature for Ru-CNF, Ru-TTAB and Ru-PVP. These results are in agreement with our previous study on FT synthesis using colloidal Ru nanoparticle catalysts [33-34]. We have proposed that oxygenates are formed on sites with relatively high barrier for CO dissociation [33]. This is necessary to maintain a sufficiently high CO coverage on the surface of the catalyst needed for termination by CO insertion [33-34]. However, the barrier for CO

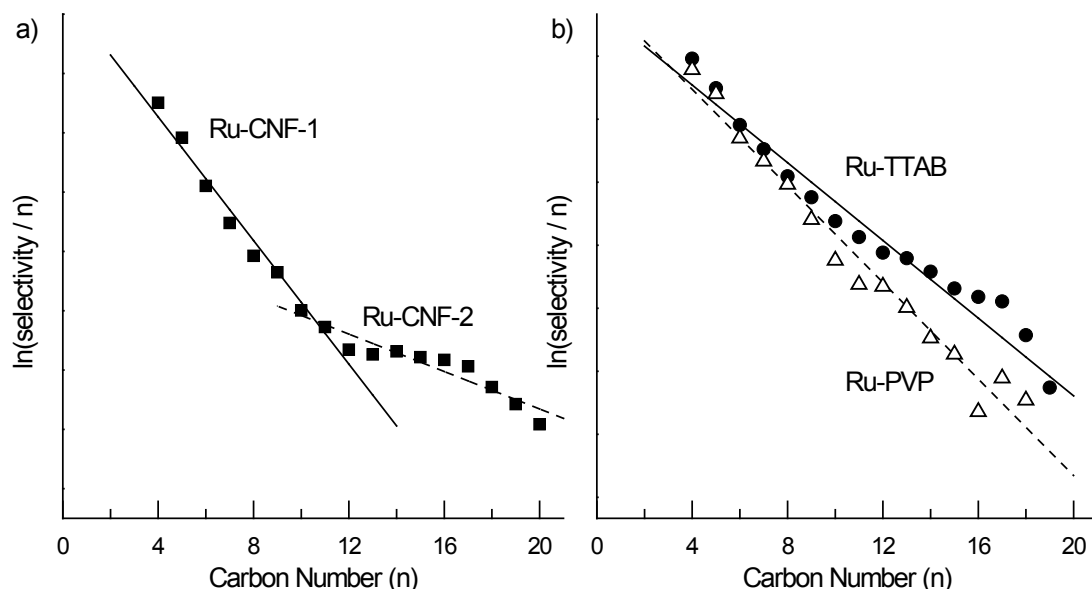


Figure 5.6: Oxygenates AFS distribution in the FT reaction at 175 °C on: (a) Ru-CNF, and (b) Ru-TTAB and Ru-PVP.

dissociation must not be too high in order to form sufficient CH_x intermediates for chain growth. In addition, to form long chain oxygenates, the rate for chain growth must be faster than the rate for chain termination [34]. Since the barrier for CO dissociation is expected to be high on oxygenates growth sites compared to chain growth and termination [34], the rate of CO dissociation increases more strongly than the rates of the other steps with temperature. Consequently, higher surface CH_x coverage will lead to an increase in α_{OXY} with temperature. For Ru-SMPS, only oxygenates with 4 carbon atoms were observed in the product mixture. Shorter-chain oxygenates could not be analysed here, so that α_{OXY} for Ru-SMPS cannot be determined. Figure 5.6a shows that Ru-CNF exhibits two different α_{OXY} for oxygenates chain below and above C_{12} . This behaviour is also observed for Ru-TTAB, but to a lesser extent. In contrast, this behaviour is absent for Ru-PVP (Figure 5.6b). Such behaviour has been previously reported for Fe-based FT [50-51]. Secondary reactions [50] and the presence of different reactive centers due to the use of promoters [51] were proposed to be the cause for the dual chain growth probability. In a previous study [34], we have concluded that the only secondary reaction that aldehyde products undergo is their hydrogenation to alcohol. The change in α_{OXY} at C_{12} is observed at all temperatures. It is seen in Figure 5.5b that there are two very different α_{OXY} values for Ru-CNF, a low one below C_{12} and a much higher one above C_{12} . The lower value is also found for Ru-TTAB and Ru-PVP. Tentatively, we attribute this to the difference in solubility of the products. Short oxygenates may be better soluble in water, which will favour their termination over further chain growth.

With increasing hydrophobicity for longer growing chain, the solubility will strongly decrease so that chain growth is favoured. The observation that this effect becomes less significant in the presence of capping agents is consistent with this as they provide an environment of uniform hydrophilicity/hydrophobicity around the reactive centers.

5.3.3 Effect of Reaction Solvent

The use of an apolar solvent instead of water was also investigated for Ru/CNF. Table 5.2 shows that the use of n-hexadecane instead of water resulted in higher FT activity. In addition, the oxygenates selectivity decreased by approximately 15%. Table 5.2 shows that the rate of oxygenates formation (r_{OXY}) is independent of the solvent used in contrast to the rate of hydrocarbons formation (r_{HC}), which was found to be higher with n-hexadecane as the solvent. Importantly, these data suggest that the high oxygenates selectivities reported in water in the present and our earlier studies are not caused by suppression of hydrocarbons formation in aqueous medium. The finding that the use of an apolar solvent as n-hexadecane increases the rate is consistent with the rate of termination being rate controlling for hydrocarbons formation. The desorption of the product into an apolar medium, which is much more closer in nature to real FT conditions, is favoured entropically over the case of desorption into a polar medium. Consistent with an increased rate of termination, it is found that α_{HC} decreases when n-hexadecane is used instead of water. In contrast, α_{OXY} does not change significantly when water is replaced by n-hexadecane, which is consistent with our proposal that CO dissociation is rate limiting in this temperature regime for oxygenates formation.

Table 5.2. Effect of solvent on the liquid phase FT reaction. ^[a]							
Solvent	r_{total} (mmol/g _{Ru} .h)	r_{HC} (mmol/g _{Ru} .h)	r_{OXY} (mmol/g _{Ru} .h)	S_{HC}	S_{OXY}	α_{HC}	α_{OXY}
Water	0.74	0.35	0.39	47%	53%	0.93	0.49
n-hexadecane	0.96	0.59	0.37	62%	38%	0.78	0.46
[a] Reaction conditions: Ru-CNF (0.1 g), Solvent (3 mL), P = 30 bar (H ₂ /CO molar ratio = 2), T = 150°C, t = 24 h.							

5.4 Conclusion

We have investigated the effect of the type of organic capping agents on Ru nanoparticles supported on a carbon nanofiber support in the FT reaction. To avoid changes in size and morphology of the initial Ru particles, the organic capping agents were introduced

to a Ru/CNF catalyst. The following three different organic capping agents with expected increasing strength of interaction with the metal were used: trimethyl(tetradecyl)ammonium bromide (TTAB) < polyvinylpyrrolidone (PVP) < sodium 3-mercapto-1-propanesulfonate (SMPS). The catalysts were characterized by TEM and ICP before and after the reaction. The presence of the organic capping agent was verified using XPS. The activity for FT reaction was found to decrease with the strength of interaction between the organic capping agent and the Ru surface. The Ru nanoparticle catalyst without capping agent exhibits the highest FT activity. SMPS severely poisons the catalyst. Despite the activity differences, the apparent activation energy for all four catalyst are similar, implying no change in the reaction mechanism. Organic capping agents with weaker interaction with the Ru particles tend to give slightly higher oxygenates selectivity. Introducing SMPS on to the Ru-CNF catalyst suppresses the formation of oxygenates. Oxygenates and hydrocarbons chain growth probabilities are shown to exhibit different trends with increasing temperature for all catalyst, suggesting that they are formed on different reactive centers. The rate of hydrocarbon formation and hydrocarbon chain growth probability for liquid phase FT is strongly influenced by the type of solvent consistent with chain growth termination being rate limiting.

References

- [1] G. A. Somorjai, J. Y. Park, *Top. Catal.* **2008**, *49*, 126-135.
- [2] B. Lim, Y. N. Xia, *Angew. Chem. Int. Ed.* **2011**, *50*, 76-85.
- [3] G. A. Somorjai, C. Aliaga, *Langmuir* **2010**, *26*, 16190-16203.
- [4] Y. J. Xiong, B. Wiley, Y. N. Xia, *Angew. Chem. Int. Ed.* **2007**, *46*, 7157-7159.
- [5] N. Semagina, L. Kiwi-Minsker, *Cat. Rev. Sci. Eng.* **2009**, *51*, 147-217.
- [6] N. Yan, C. X. Xiao, Y. Kou, *Coord. Chem. Rev.* **2010**, *254*, 1179-1218.
- [7] A. R. Tao, S. Habas, P. D. Yang, *Small* **2008**, *4*, 310-325.
- [8] Y. Xia, Y. J. Xiong, B. Lim, S. E. Skrabalak, *Angew. Chem. Int. Ed.* **2009**, *48*, 60-103.
- [9] Y. W. Zhang, M. E. Grass, J. N. Kuhn, F. Tao, S. E. Habas, W. Y. Huang, P. D. Yang, G. A. Somorjai, *J. Am. Chem. Soc.* **2008**, *130*, 5868-5869.
- [10] H. Song, R. M. Rioux, J. D. Hoefelmeyer, R. Komor, K. Niesz, M. Grass, P. D. Yang, G. A. Somorjai, *J. Am. Chem. Soc.* **2006**, *128*, 3027-3037.
- [11] Y. Zhang, M. E. Grass, W. Huang, G. A. Somorjai, *Langmuir* **2010**, *26*, 16463-16468.
- [12] J. N. Kuhn, C.-K. Tsung, W. Huang, G. A. Somorjai, *J. Catal.* **2009**, *265*, 209-215.
- [13] C. A. Stowell, B. A. Korgel, *Nano Lett.* **2005**, *5*, 1203-1207.
- [14] X. Wang, P. Sonström, D. Arndt, J. Stöver, V. Zielasek, H. Borchert, K. Thiel, K. Al-Shamery, M. Bäumer, *J. Catal.* **2011**, *278*, 143-152.
- [15] J. Y. Park, C. Aliaga, J. R. Renzas, H. Lee, G. A. Somorjai, *Catal. Lett.* **2009**, *129*, 1-6.
- [16] Y. Li, M. A. El-Sayed, *J. Phys. Chem. B* **2001**, *105*, 8938-8943.
- [17] R. Narayanan, M. A. El-Sayed, *J. Phys. Chem. B* **2004**, *108*, 8572-8580.
- [18] H. R. Choi, H. Woo, S. Jang, J. Y. Cheon, C. Kim, J. Park, K. H. Park, S. H. Joo, *ChemCatChem* **2012**, *4*, 1587-1594.
- [19] M. Crespo-Quesada, J.-M. Andanson, A. Yarulin, B. Lim, Y. Xia, L. Kiwi-Minsker, *Langmuir* **2011**, *27*, 7909-7916.
- [20] B. Wu, H. Huang, J. Yang, N. Zheng, G. Fu, *Angew. Chem. Int. Ed.* **2012**, *51*, 3440-3443.
- [21] Q. Zhang, J. Kang, Y. Wang, *ChemCatChem* **2010**, *2*, 1030.

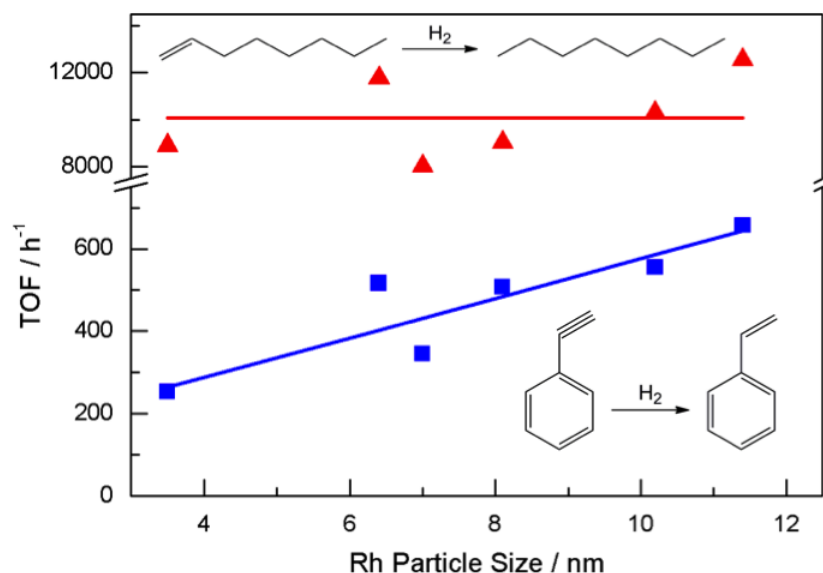
- [22] E. van Steen, M. Claeys, *Chem. Eng. Technol.* **2008**, *31*, 655-666.
- [23] A. Y. Khodakov, W. Chu, P. Fongarland, *Chem. Rev.* **2007**, *107*, 1692-1744.
- [24] J. J. Spivey, A. Egbebi, *Chem. Soc. Rev.* **2007**, *36*, 1514-1528.
- [25] R. A. van Santen, I. M. Ciobica, E. van Steen, M. M. Ghouri, *Adv. Catal.* **2011**, *54*, 127-187.
- [26] H. Pichler, H. Schulz, *Chem. Ing. Tech.* **1970**, *42*, 1162-1174.
- [27] B. H. Davis, *Catal. Today* **2009**, *141*, 25-33.
- [28] C. X. Xiao, Z. P. Cai, T. Wang, Y. Kou, N. Yan, *Angew. Chem. Int. Ed.* **2008**, *47*, 746-749.
- [29] X. B. Fan, Z. Y. Tao, C. X. Xiao, F. Liu, Y. Kou, *Green Chem.* **2010**, *12*, 795-797.
- [30] L. Liu, G. Sun, C. Wang, J. Yang, C. Xiao, H. Wang, D. Ma, Y. Kou, *Catal. Today* **2012**, *183*, 136-142.
- [31] C. Wang, H. Zhao, H. Wang, L. Liu, C. Xiao, D. Ma, *Catal. Today* **2012**, *183*, 143-153.
- [32] D. O. Silva, J. D. Scholten, M. A. Gelesky, S. R. Teixeira, A. C. B. Dos Santos, E. F. Souza-Aguiar, J. Dupont, *ChemSusChem* **2008**, *1*, 291-294.
- [33] X.-Y. Quek, Y. Guan, R. A. van Santen, E. J. M. Hensen, *ChemCatChem* **2011**, *3*, 1735-1738.
- [34] X.-Y. Quek, R. Pestman, I. A. W. Filot, V. Petkov, R. A. van Santen, E. J. M. Hensen, in-preparation.
- [35] J. Kang, S. Zhang, Q. Zhang, Y. Wang, *Angew. Chem. Int. Ed.* **2009**, *48*, 2565-2568.
- [36] J. M. a. G. I. Carballo, J. Yang, A. Holmen, S. García-Rodríguez, S. Rojas, M. Ojeda, J. L. G. Fierro, *J. Catal.* **2011**, *284*, 102-108.
- [37] G. L. Bezemer, J. H. Bitter, H. Kuipers, H. Oosterbeek, J. E. Holewijn, X. D. Xu, F. Kapteijn, A. J. van Dillen, K. P. de Jong, *J. Am. Chem. Soc.* **2006**, *128*, 3956-3964.
- [38] A. Lepp, O. Siiman, *J. Phys. Chem.* **1985**, *89*, 3494.
- [39] P. Jiang, S. Y. Li, S. S. Xie, Y. Gao, L. Song, *Chem. Eur. J.* **2004**, *10*, 4817.
- [40] C. Aliaga, J. Y. Park, Y. Yamada, H. S. Lee, C.-K. Tsung, P. Yang, G. A. Somorjai, *J. Phys. Chem. C* **2009**, *113*, 6150-6155.
- [41] M. L. Toebes, J. M. P. van Heeswijk, J. H. Bitter, A. Jos van Dillen, K. P. de Jong, *Carbon* **2004**, *42*, 307-315.
- [42] C. Kim, M. Min, Y. W. Chang, K.-H. Yoo, H. Lee, *J. Nanosci. Nanotechnol.* **2010**, *10*, 233-239.
- [43] C. H. Bartholomew, *Appl. Catal. A* **2001**, *212*, 17-60.
- [44] N. E. Tsakoumis, M. Ronning, O. Borg, E. Rytter, A. Holmen, *Catal. Today* **2010**, *154*, 162-182.
- [45] Y. Borodko, S. E. Habas, M. Koebel, P. Yang, H. Frei, G. A. Somorjai, *J. Phys. Chem. B* **2006**, *110*, 23052-23059.
- [46] Y. Borodko, L. Jones, H. Lee, H. Frei, G. Somorjai, *Langmuir* **2009**, *25*, 6665-6671.
- [47] G. P. Van der Laan, A. Beenackers, *Cat. Rev. Sci. Eng.* **1999**, *41*, 255-318.
- [48] R. A. Dictor, A. T. Bell, *J. Catal.* **1986**, *97*, 121-136.
- [49] R. A. van Santen, M. M. Ghouri, S. Shetty, E. J. M. Hensen, *Catal. Sci. Tech.* **2011**, *1*, 891-911.
- [50] B. H. Davis, *ACS Div. Fuel Chem. Preprints* **1992**, *37*, 172-183.
- [51] G. A. Huff Jr, C. N. Satterfield, *J. Catal.* **1984**, *85*, 370-379.

Chapter 6

Structure Sensitivity in the Hydrogenation of Unsaturated Hydrocarbons over Rh Nanoparticles

Summary

A series of Rh nanoparticles with sizes between 3.5 to 11.4 nm were synthesized in the presence of polyvinylpyrrolidone and evaluated for their performance as catalysts in the hydrogenation of phenylacetylene and 1-octene. The reaction is zeroth order in the reactant for phenylacetylene and 1-octene. The catalytic activity increased with Rh particle size in the hydrogenation of phenylacetylene, whereas the activity in 1-octene hydrogenation did not depend on particle size. The possible explanations for this different particle size behavior are discussed.



6.1 Introduction

The recent advancement in colloidal chemistry has allowed more effective control of the size and morphology of metallic nanoparticles with many applications in the field of catalysis [1-7]. Among the various methods employed to prepare colloidal nanoparticles, polyol reduction of metal salts in the presence of polyvinylpyrrolidone (PVP) is one of the most common methods to synthesize mono-dispersed nanoparticles with a narrow size distribution [1-3]. This approach has been shown to be effective in controlling both the size [8-9] and shape [10] of the particles. For instance, PVP stabilized Rh nanoparticles with sizes between 2 to 11 nm were prepared by the group of Somorjai [8-9]. In addition, Rh nanoparticles of different shapes were successfully synthesized including cube, tetrahedral, polyhedral, multipods, ultrathin plates, starfish-like and concave cubes Rh nanocrystals [10]. One advantage of using colloidal nanoparticles in fundamental catalysis studies is to decouple the effect of the metal-support interaction from the intrinsic effect of the particle size on the activity of the surface metal atoms. Thus, the use of colloidal nanoparticles offers opportunities to study the intrinsic structure-activity relationship of metal nanoparticles [1-6].

Based on the extensive work on Pt catalysts in the 1960s and early 1970s Boudart classified reactions as structure sensitive or structure insensitive [11]. For instance, the rate of alkane hydrogenolysis will strongly depend on the Pt particle size in contrast to the rate of olefin hydrogenation, which is structure insensitive [2, 4]. Che and Bennette classified structure sensitive/insensitive-particle size relationship into three different types, where rate normalized per exposed metal surface atom, decreases, remained constant or increases with increasing particle size. [12].

In the last decade or so a firm theoretical basis about surface reactivity of metals has been developed to understand structure sensitivity [13-15]. Van Santen reviewed the issue of structure sensitivity in detail from the viewpoint of reactivity of molecules at metal surface ensembles with different surface metal atom coordination and topology [14]. Broadly speaking, structure sensitivity depends on the type of bond to be activated during the rate limiting elementary reaction step at the surface. When this step involves the formation or cleavage of a π -bond as is the case in the activation of CO, NO or N₂, the rate will increase with increasing particle size. The reason lies in the much lower activation energy for such reactions over step-edge sites than over terraces, which is mainly related to the absence of surface metal atom sharing of the dissociating atoms. Activation of σ -bonds such as the dissociative adsorption of methane (C-H bond activation) occurs over a single surface metal

atom with a late transition state. In this case, Brønsted-Evans-Polanyi (BEP) considerations predict that lower surface metal atom coordination results in higher reactivity due to stabilization of the transition and final states because of increased adsorption energies of the dissociating molecule. Accordingly, one predicts that smaller particles are more active in σ -bond cleavage. In contrast, the reverse reaction that forms a σ -bond such as the case for hydrogenation is characterized by an early transition state. This implies that a stabilization of the initial state by a more reactive surface metal atom will also stabilize the transition state further. BEP considerations dictate then that the formation of a σ -bond does not strongly depend on the particle size. As such, this explains the structure insensitivity of metals such as Pt in olefin hydrogenation.

The influence of metal particle size on the hydrogenation of olefinic bonds is of great interest due to the importance of hydrogenation processes in the petrochemical, fine chemical and food industries [16-17]. Although hydrogenation is argued to be structure insensitive [14], contradicting reports can be found in literature. Some reports claim indeed that the hydrogenation is independent of particle size [2, 18-21], whereas others show that the activity increases with particle size [22-31].

Structure insensitivity in hydrogenation has mainly been reported for Pt and Pd catalysts. When Pt particles increase from 1 to 7 nm, the catalytic activity was found to be unaffected in the hydrogenation of ethylene [2, 18-19] and cyclohexene [2, 20]. For Pd particles between 6 to 11 nm, Semagina et al. [21] found that the activity for 1-hexyne hydrogenation did not depend on the particle size. In contrast, the activity increased with Pt nanoparticle size (1-7 nm) in the hydrogenation of cinnamaldehyde [22-23], crotonaldehyde [24] and cyclohexanone [25]. Higher activity was also observed for the hydrogenation of 1,3-butadiene [26], 2-methyl-3-butyl-2-ol [27] and allyl alcohol [28] with increasing Pd particle size from 1 to 13 nm. Although the effect of particle size in hydrogenation for Ru and Rh is less well documented, increasing catalytic activities with particle size have also been observed. Campbell et al. [29] reported increasing activities for 1,3-cyclohexadiene hydrogenation with increasing Ru nanoparticle size (1-3 nm). In the hydrogenation of ethyl pyruvate [30] and xylene [31], increasing the Rh particle size from 1-2 nm to 2-8 nm resulted in higher activity.

Despite Rh being an excellent hydrogenation catalyst, a comprehensive study on the particle size effect for Rh is still lacking. The aim of this work is to investigate whether hydrogenation of olefinic bonds is particle size dependent. PVP stabilized Rh nanoparticles

from 3.5 to 11.4 nm will be synthesized and used in the hydrogenation of phenylacetylene and 1-octene.

6.2 Experimental Methods

6.2.1 Synthesis of Materials

Polyvinylpyrrolidone (PVP, $M_n = 10\,000$, Sigma Aldrich) stabilized Rh nanoparticles were synthesized according to a published procedure [9]. Rh nanoparticles were prepared by reducing either rhodium(III) chloride hydrate ($\text{RhCl}_3 \cdot n\text{H}_2\text{O}$, Aldrich) or rhodium(III) acetylacetonate ($\text{Rh}(\text{acac})_3$, Aldrich) at different temperature in ethylene glycol (EG, Merck) or 1,4-butanediol (Sigma Aldrich). In a typical synthesis, 20 mg of $\text{Rh}(\text{acac})_3$ and 0.11 g of PVP were dissolved in 2 mL of tetrahydrofuran (THF, Sigma Aldrich) and 3 mL of 1,4-butanediol. The mixture was then added to 17 mL of 1,4-butanediol preheated to 220 °C and refluxed under N_2 flow for 6 h. The resultant black mixture was washed thoroughly with acetone and diethyl ether and collected by centrifugation. The isolated Rh nanoparticles were then redispersed in 3 mL deionized water. Although 1,4-butanediol and excess PVP can be removed by washing, a portion of PVP is still coordinated to the surface of the Rh particles. The only effective method of removing these surface coordinated PVP without using high temperature calcination is by UV-ozone cleaning [32].

6.2.2 Characterization

Transmission electron microscopy (TEM) was performed on FEI Tecnai 20 electron microscope at an acceleration voltage of 200 kV with a LaB_6 filament. A small amount of the sample was diluted with ethanol, dispersed and dried over a carbon-coated Cu grid. Particle size distribution was calculated by measuring more than 150 particles. X-ray diffraction was measured under ambient conditions with a Bruker Endeavour D4 diffractometer using filtered $\text{Cu K}\alpha$ radiation (40 kV and 40 mA). Diffraction data were recorded from 2θ from 25° to 60° at a resolution of 0.05°. X-ray photoelectron spectrometer (XPS) samples were prepared by drying the dispersed Rh nanoparticles on a silica wafer before introducing into a Thermo Scientific K-Alpha XPS equipped with a monochromatic $\text{Al K}\alpha$ X-ray. For survey and region scans, constant pass energies of 160 eV and 40 eV, respectively, were used. The background pressure was 2×10^{-9} mbar. Fitting was carried out with the CasaXPS program.

6.2.3 Catalytic Activity Measurements

Liquid phase catalytic hydrogenation experiments were carried out in a batch reactor operated at atmospheric pressure. 1 mmol of reactant being either phenylacetylene (Fluka) or 1-octene (Sigma Aldrich), 1.6 μmol of Rh nanoparticles, 0.4 mL of deionized water and 15 mL of n-heptane were introduced into a round-bottom flask. Pure molecular hydrogen was bubbled through the flask at a flow rate of 30 mL/min for 5 min under vigorous magnetic stirring (800 rpm). The reaction was initiated by immersing the flask into an oil bath maintained at 70 °C. The reaction time was 4 h for phenylacetylene and 1 h for 1-octene. Aliquots of 100 μL liquid were extracted from the reactor at regular intervals (1 h for phenylacetylene and 15 min for 1-octene) and diluted with ethanol before analysis. The liquid sample was analyzed by gas chromatography (QP5050, Shimadzu) equipped with a Rxi-5ms capillary column (30 m \times 0.25 mm \times 0.5 μm) and a flame ionization detector (FID).

The turn over frequency (TOF) are calculated base on the following equations:

$$\text{TOF} = \frac{\text{moles reacted}}{\text{mol Rh}_{\text{surface}} \times \text{reaction time}}$$

with the number of mol $\text{Rh}_{\text{surface}} = \text{mol Rh} \times D$ and D being the dispersion.

The dispersion (D) was calculated assuming spherical shapes by using the formula described by Scholten et al. [33]:

$$D = 10^{21} \times \frac{6 \times M \times \rho_{\text{site}}}{d_p \times N_{\text{AV}} \times \rho_{\text{metal}}}$$

with M being the atomic weight of Rh, ρ_{site} the surface density, ρ_{metal} the density of metal, N_{AV} Avogadro's number.

6.3 Results and Discussion

6.3.1 Catalyst Characterizations

Our initial approach to control the size of Rh nanoparticles was to vary the PVP/Rh molar ratio and the reduction time (t_R). The PVP/Rh ratio was varied from 6 to 24 and t_R was varied from 5 to 120 min as summarized in Table 6.1. Figure 6.1 shows the transmission electron micrographs and XRD patterns for Rh nanoparticles prepared using RhCl_3 with PVP/Rh molar ratio of 18 and 24 and $t_R = 5$ min. The average particle size of these PVP stabilized Rh nanoparticles from TEM analysis is 3.3 ± 0.5 nm for PVP/Rh ratios of 18 and 24, respectively. The Rh particle size estimated by applying Scherrer's equation to the

Rh(111) reflection gave similar results (3.3 nm for PVP/Rh = 18 and 24). Table 6.1 summarizes the particle size of Rh determined by XRD and TEM when the PVP/Rh ratio and t_R were varied. Although previous studies found that the size of Pt and Pd nanoparticles can be varied by changing the PVP/Rh ratio and reduction time [34-35], only small changes were found in the Rh particle size when varying these parameters. Hence, we conclude that changing Rh/PVP ratio and t_R is not a good method to obtain Rh nanoparticles with different sizes.

Table 6.1. Rh nanoparticles synthesis conditions and particle size.^[a]

Rh Source	Temperature (°C)	Solvent	PVP/Rh Molar Ratio	t_R (h)	$d_{XRD}^{[b]}$ (nm)	$d_{TEM}^{[c]}$ (nm)
RhCl ₃	140	EG	6	5 min	2.9	2.9 ± 0.6
RhCl ₃	140	EG	12	5 min	3.5	n.d.
RhCl ₃	140	EG	18	5 min	3.3	3.3 ± 0.5
RhCl ₃	140	EG	24	5 min	3.3	3.3 ± 0.5
RhCl ₃	140	EG	6	0.5	3.4	3.0 ± 0.7
RhCl ₃	140	EG	6	1	3.4	n.d.
RhCl ₃	140	EG	6	2	3.4	n.d.

[a] Molecular weight of PVP used, Mn = 58 000. [b] Particle size determine from XRD using Scherrer's equation for Rh(111) peak. [c] Average particle size and standard deviation determined from TEM.

Previous reports suggest that changing the reduction temperature and the Rh source is able to effectively control the size of Rh nanoparticles [8, 36]. Table 6.2 gives the results for such experiments by which Rh nanoparticles between 3.5 to 11.4 nm were obtained. Transmission electron micrographs and the corresponding particle size distributions are given in Figure 6.2. Figure 6.3 shows that higher reduction temperature resulted in larger Rh nanoparticles. By using Rh(acac)₃ instead of RhCl₃ under otherwise similar conditions we obtained larger particles, suggesting that the ligand is also important. Chaudret and co-workers have extensively investigated the possibilities to control the size and morphology of metallic nanoparticles by using organometallic precursor compounds [37-38]. Figure 6.3 also shows that reducing RhCl₃ at higher temperature cannot further increase the particle size. The particle size leveled off when the reduction temperature increases from 160 °C to 190 °C. However, for Rh(acac)₃ the size of Rh nanoparticles can be further increased by an increase of the reduction temperature. The temperature is however limited by the boiling point of 1,4-butandiol.

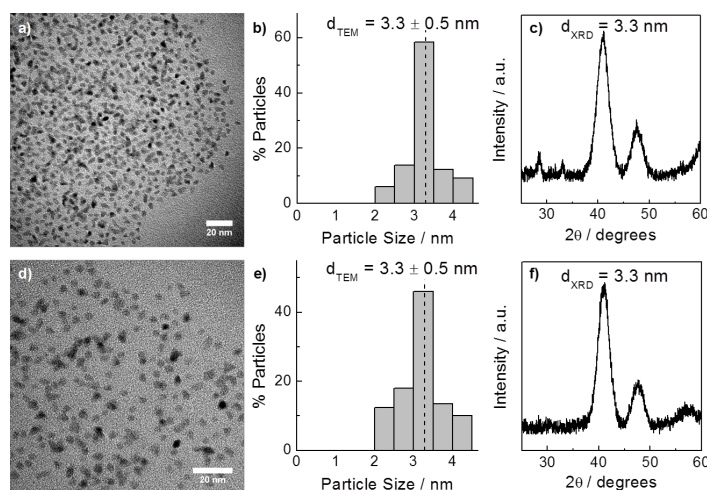


Figure 6.1: PVP-stabilized Rh nanoparticles: (a,d) Electron micrograph; (b,e) particle size distribution; (c,f) XRD pattern for PVP/Rh = 18 and $t_{\text{R}} = 5$ (a-c) and PVP/Rh = 24 and $t_{\text{R}} = 5$ (d-f).

TEM micrographs in Figure 6.2 show that smaller Rh particles are mostly composed of spherical particles. When the particle size increase, the portion of well faceted particles increases. The well-faceted PVP stabilized Rh nanoparticles contain various polygonal shapes such as hexagons, pentagons, triangles and rhombohedra. However, no dominant shape was observed among these particles.

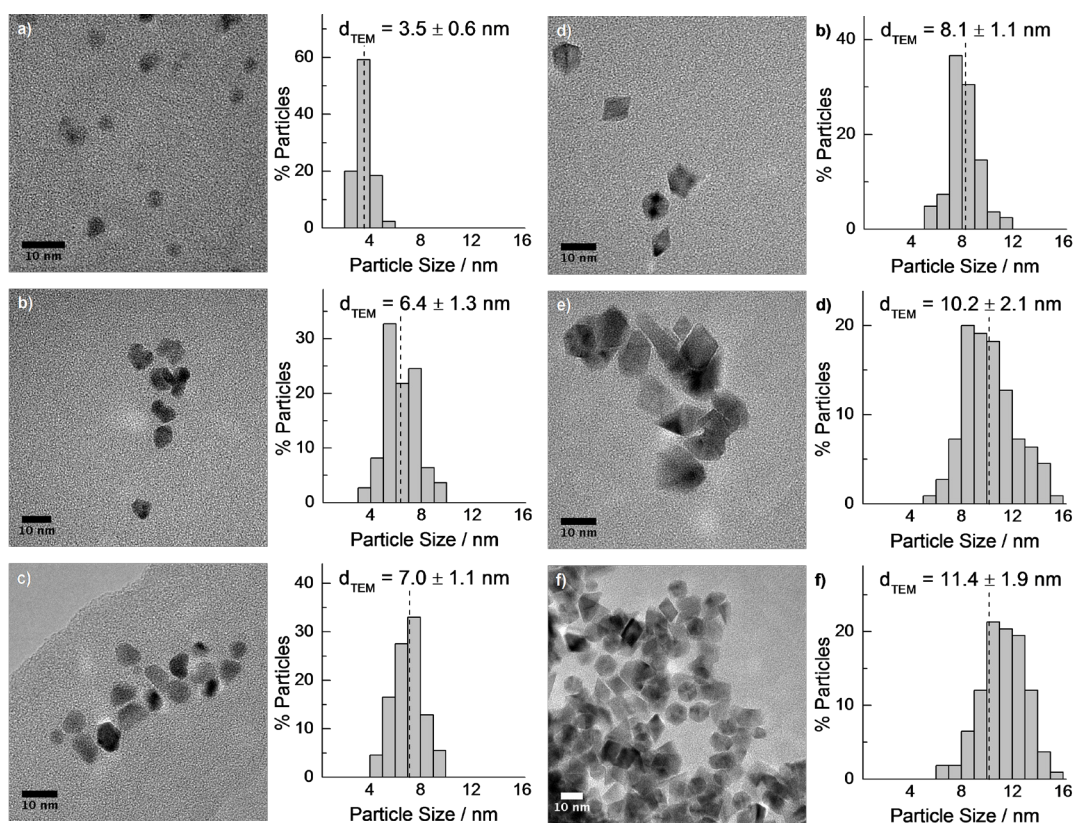


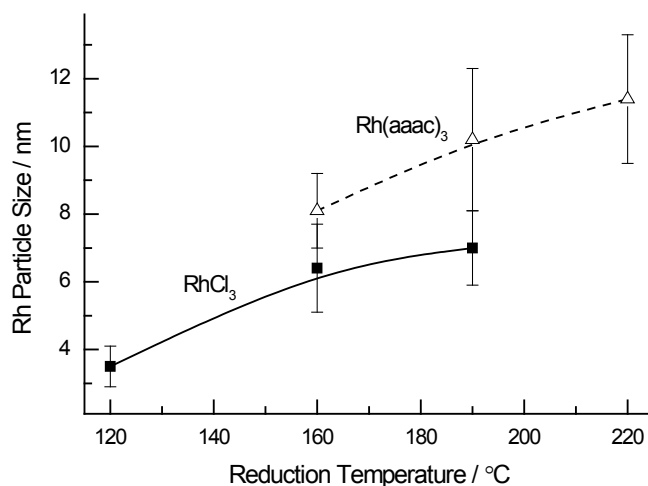
Figure 6.2: Electron micrograph and particle size distribution of Rh nanoparticles prepared using RhCl_3 (a,b,c) or $\text{Rh}(\text{acac})_3$ (d,e,f) reduced at 120 °C (a), 160 °C (b), 190 °C (c), 160 °C (d), 190 °C (e) and 220 °C (f).

Table 6.2. Rh nanoparticles synthesis conditions and particle size.^[a]

Catalyst	Rh Source	T (°C)	t _R (h)	d _p ^[b] (nm)	Rh Conc. ^[c] (µg/mL)	Rh ⁰ Content
Rh-3.5	RhCl ₃	120	5 min	3.5 ± 0.6	762	79
Rh-6.4	RhCl ₃	160	6	6.4 ± 1.3	974	79
Rh-7.0	RhCl ₃	190	6	7.0 ± 1.1	875	76
Rh-8.1	Rh(acac) ₃	160	6	8.1 ± 1.1	762	84
Rh-10.2	Rh(acac) ₃	190	6	10.2 ± 2.1	905	86
Rh-11.4	Rh(acac) ₃	220	6	11.4 ± 1.9	835	83

[a] 1,4-Butanediol as reducing agent and solvent, PVP/Rh molar ratio = 20, Mn(PVP) = 10 000. [b] Average particle size and standard deviation determined from TEM. [c] Determined from ICP. [d] Determined from XPS.

Figure 6.4 shows the X-ray photoelectron (XP) spectra for Rh-3.5 and Rh-11.4. The spectra of these nanoparticles contain peaks at 306.5 eV and 308.0 eV, indicating the presence of Rh⁰ and Rh³⁺, respectively. Although from the XP spectra, the presence of other oxidic Rh species cannot be excluded, we believe their contribution to the total Rh content is small and will be excluded in our discussion. The metallic Rh content for different particle size was determined from such XP spectra and are collected in Table 6.2. Although it is known that small particles are usually more oxidic in nature [39-40], our results indicate that decreasing particle size only slightly decrease the metallic Rh content. The average content of metallic Rh was 81 ± 4 %. One possible explanation for the small change in metallic Rh when particle size changes could be due to slight underestimation the metallic Rh in large particles due to penetration depth of XPS (maximum 10 nm).

**Figure 6.3:** Rh particle size as a function of reduction temperature.

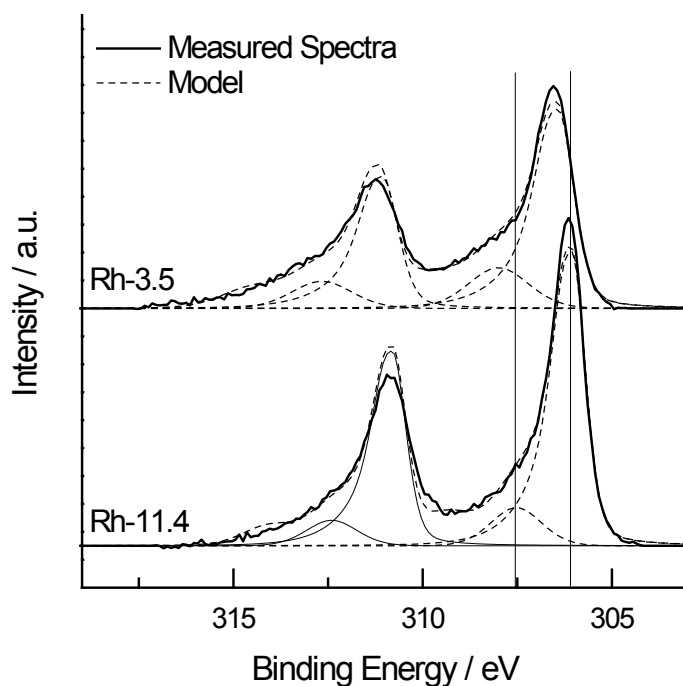


Figure 6.4: X-ray photoelectron spectra of Rh nanoparticles in the Rh 3d region.

6.3.2 Effect of PVP/Rh Ratio and Reduction Time

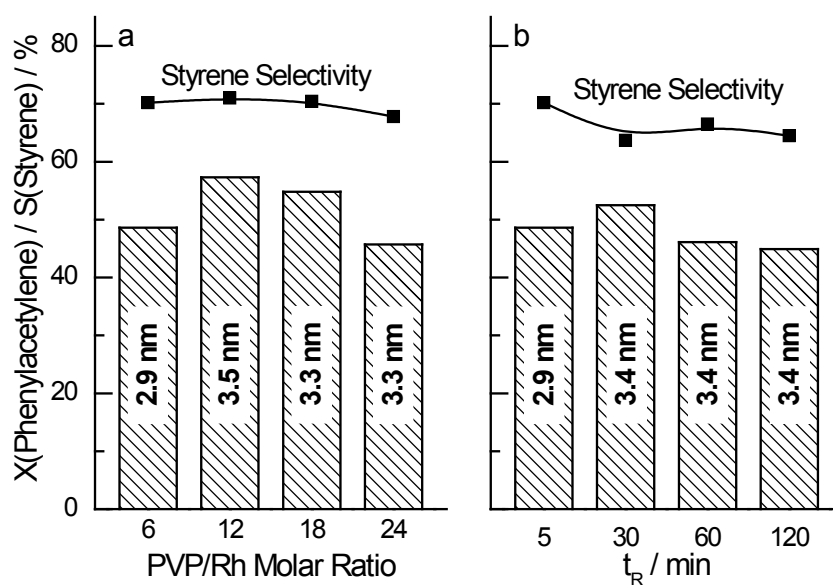


Figure 6.5: Rh nanoparticle size and catalytic activity in phenylacetylene hydrogenation as a function of (a) PVP/Rh ratio, and (b) reduction time.

Although recently Yang et al.[41] have showed that PVP stabilized Rh nanoparticles in ionic liquid is able to effectively convert styrene into ethylbenzene, our experiments shows that phenylacetylene is predominately semi-hydrogenated to styrene and ethylbenzene is being formed as a minor byproduct. In our studies, styrene was not formed as the main

product our experiments were conducted at atmospheric pressure by bubbling H_2 through our reaction mixture while Yang et al. [41] carried out the reaction under 50 bar H_2 . Thermodynamically, high pressure will favor hydrogenation to styrene as more hydrogen is being consumed. Figure 6.5 shows the effect of the PVP/Rh ratio on the phenylacetylene hydrogenation activity and selectivity. Phenylacetylene conversion remained nearly unchanged with increasing surfactant to Rh ratio ($51 \pm 5\%$). Styrene selectivity also remained constant at approximately $70 \pm 1\%$. Similarly, increasing reduction time had only very small effect on the hydrogenation activity and selectivity, that is the phenylacetylene conversion and styrene selectivity were $48 \pm 3\%$ and $66 \pm 3\%$, respectively, when the sample was longer reduced. These results show that particles of the same size yield comparable catalytic activities independent of the amount of PVP and the reduction time.

6.3.3 Time Dependent Hydrogenation Activity and Selectivity

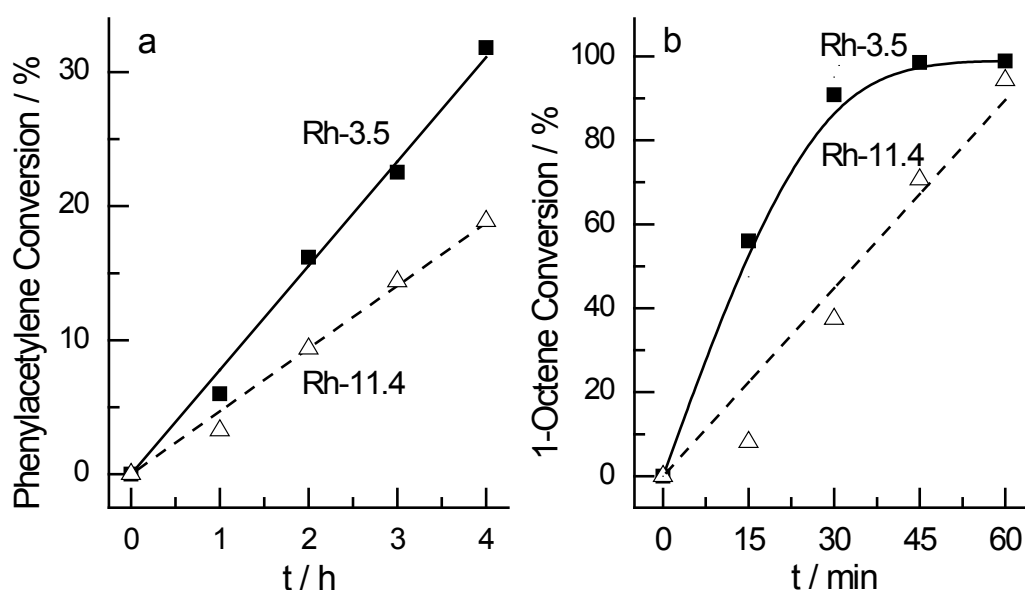


Figure 6.6: Hydrogenation of (a) phenylacetylene and (b) 1-octene over Rh-3.5 and Rh-11.4 as a function of reaction time.

Figure 6.6 shows the activity for phenylacetylene (Figure 6.6a) and 1-octene (Figure 6.6b) hydrogenation with reaction time for Rh-3.5 and Rh-11.4. In the hydrogenation of phenylacetylene, conversion increases linearly with reaction time for both Rh-3.5 and Rh-11.4. This indicates a zero order reaction with respect to phenylacetylene, which was also observed by Jackson and Shaw using a Pd/C catalyst [42]. Styrene selectivity remained unchanged with time at $74 \pm 3\%$ for both catalysts. Similarly, in the hydrogenation of 1-octene (Figure 6.6b), it was seen that conversion increased linearly with reaction time for Rh-

11.4, while a plateau was reached for Rh-3.5 at approximately 90% conversion. Hence, 1-octene hydrogenation also exhibits zero order behaviour in the reactant when conversion is kept below 80%.

6.3.4 Effect of Particle Size on Hydrogenation

Figure 6.7 shows the effect of the Rh particle size on the turnover frequency (TOF) for the hydrogenation phenylacetylene and 1-octene calculated on the basis of the total surface Rh atoms. In the hydrogenation of phenylacetylene, it is observed that TOF increases linearly from 250 to 650 h^{-1} when the Rh particle size increases from 3.5 to 11.4 nm. However, for 1-octene the TOF remained at about 10000 h^{-1} independent of the Rh particle size.

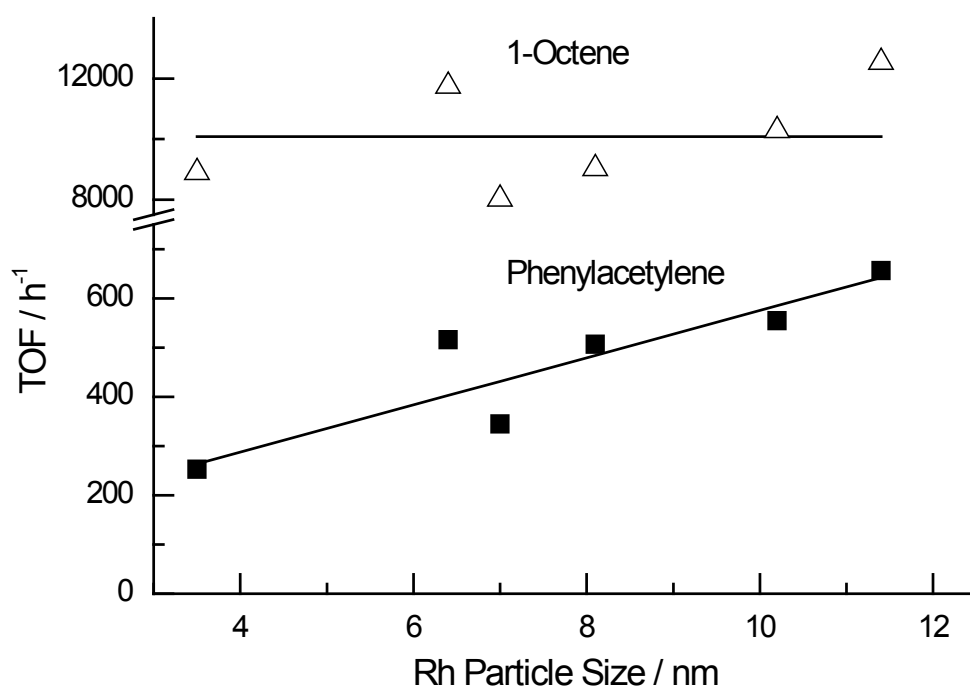
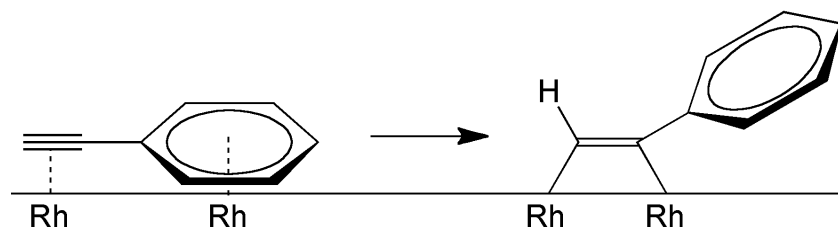


Figure 6.7: Effect of Rh particle size on the TOF of phenylacetylene and 1-octene hydrogenation.

An explanation for the different dependency of the activity on the particle size for the hydrogenation of phenylacetylene and 1-octene relates to the adsorption mode of the reactant on the surface of the Rh nanoparticle. It is well established that the electron-rich benzene ring prefers to adsorb in a planar mode to metal surfaces [43]. Hence, the adsorption of phenylacetylene would require a certain ensemble of metal atoms. Accordingly, larger particles with larger terrace surface planes may favor adsorption of the phenyl ring, thus increasing the catalytic activity. In contrast, the alkyl tail of 1-octene will hardly interact with the metal surface, as for instance observed for the adsorption of 1-hexene [43]. Therefore, the

adsorption of 1-octene requires a smaller ensemble of metal atoms compared to phenylacetylene and one does not expect large changes in the hydrogenation activity with the change in the particle size as predicted by modern insights into surface reactivity.



Scheme 6.1: Activation of adsorbed phenylacetylene on Rh surface from sp to sp^2 hybridization.

Another possible explanation for the different trend with increasing particle size for the hydrogenation of phenylacetylene and 1-octene could be a difference in the rate limiting steps. The general accepted mechanism for hydrogenation follows the Horiuti-Polanyi mechanism, which involves (i) adsorption of the unsaturated bond onto the catalyst surface, (ii) activation of the unsaturated bond and (iii) stepwise hydrogen addition to the substrate followed by (iv) desorption [44]. For the hydrogenation of phenylacetylene, the increasing activity with particle size may suggest that the activation of the triple bond is the rate limiting step. It has indeed been shown that the activation of unsaturated bonds proceeds more facile on larger particles [14]. In the other case where the hydrogenation of 1-octene is independent of particle size, stepwise addition of H to 1-octene will be the rate limiting step as formation of σ -bond is known to be independent of particle size [14]. One possible explanation for the suggestion of triple bond activation in phenylacetylene to be rate limiting lies in the opposing requirements for the adsorption of the benzene ring and the activation of phenylacetylene. In the activation of the triple bond, the hybridization of the alkyne carbons will change from sp to sp^2 , producing a phenylethylene as shown in Scheme 6.1. As a result of this, the benzene ring is no longer planar to the surface due to steric reasons [45]. Since benzene prefers to adsorb on the metal surface in a planar manner, the inclined position of the benzene ring during alkyne activation of phenylacetylene may hinder the activation of the triple bond. This will increase the activation energy barrier. A similar train of thought does not apply to the activation of 1-octene, because the alkyl chain does not have to be adsorbed on the metal surface. Another explanation for the difference in rate limiting step could be related to the substituent group attached to the unsaturated C-C bond (π -bond). Previous experimental and theoretical studies of phenylacetylene adsorption found that the interaction between the π -system of the benzene ring and triple bond produce an increase in electron density at the

alkyne carbon atoms [46]. Hence, the activation of the stabilized triple bond in phenylacetylene can be argued to be more difficult than the activation of the double bond in 1-octene.

Literature data were compared in order to determine the most important factor contributing to the particle size dependence during hydrogenation. Earlier, it has been reported that hydrogenation is insensitive for ethylene [2, 18-19], cyclohexene [2, 20] and 1-hexyne [21]. In these cases, unsaturated C-C bond is attached to a H atom or an alkyl group. Particle size dependence was reported for hydrogenation of an unsaturated C-heteroatom bond or a C-C bond attached to a group with high electron density. Example reactants of this type are cinnamaldehyde [22-23], crotonaldehyde [24], cyclohexanone [25], 2-methyl-3-butyl-2-ol [27] and allyl alcohol [28], 1,3-cyclohexadiene [29], ethyl pyruvate [30], 1,3-butadiene [26] and xylene [31]. For hydrogenation of relatively small molecules such as 1,3-butadiene, crotonaldehyde, ethyl pyruvate and crotonaldehyde, the increase in activity with particle size cannot be explained by the ensemble effect. Hence, we expect that in this case the difference in the rate limiting step has a more significant influence on the particle size dependence than the adsorption requirement. However, with such small molecules, we cannot differentiate between the particle size effect as a consequence of the change in hybridization or the substituent group attached to the unsaturated bond, because these molecules also contain an electron rich group, which prefers to be adsorbed on the surface. For cyclohexanone, the change in hybridization from sp^2 to sp^3 during the C=O activation has little influence on the adsorption of the attached cyclohexane, since it is not electron rich and does not need to be adsorbed on the metal surface in a planar manner. Therefore, the electron rich oxygen could have increased the electron density at the C=O bond and stabilized it. Hence, we postulate that the substituent group attached to the unsaturated bond is the most important factor, which determines whether the hydrogenation activity of a reactant containing unsaturated C-C bonds will depend on the metal particle size.

6.4 Conclusion

Size control of Rh nanoparticles stabilized by PVP is only possible to a very limited extent by varying the Rh to PVP ratio and reduction time. Rh nanoparticles of similar size exhibited similar activity in the semihydrogenation of phenylacetylene independent of the PVP/Rh ratio and reduction time. With variation of the reduction temperature and Rh source, Rh nanoparticles between 3.5 to 11.4 nm were obtained. For PVP stabilized Rh nanoparticles

catalyzed hydrogenation of phenylacetylene and 1-octene, we found zero order behavior with respect to the reactants. In the hydrogenation of phenylacetylene, activity was found to increase with increasing Rh particle size, but for 1-octene the activity remained constant. The dependence of the hydrogenation activity on the Rh metal particle size was proposed to be due to the difference in the adsorption site requirement (large surface ensemble for phenyl adsorption) and in the rate limiting step. We postulate that the most significant factor influencing the structure sensitivity in hydrogenation is due to the difference in rate limiting step. For phenylacetylene hydrogenation, the activation of the unsaturated π -bond is the rate limiting step. For 1-octene, the formation of the C-H σ -bond is the rate limiting step. The substituent group attached to the unsaturated bond is suspected to have influenced the rate limiting step.

References

- [1] A. R. Tao, S. Habas, P. D. Yang, *Small* **2008**, *4*, 310-325.
- [2] G. A. Somorjai, J. Y. Park, *Top. Catal.* **2008**, *49*, 126-135.
- [3] B. Lim, Y. N. Xia, *Angew. Chem. Int. Ed.* **2011**, *50*, 76-85.
- [4] G. A. Somorjai, C. Aliaga, *Langmuir* **2010**, *26*, 16190-16203.
- [5] Y. J. Xiong, B. Wiley, Y. N. Xia, *Angew. Chem. Int. Ed.* **2007**, *46*, 7157-7159.
- [6] N. Semagina, L. Kiwi-Minsker, *Cat. Rev. Sci. Eng.* **2009**, *51*, 147-217.
- [7] N. Yan, C. X. Xiao, Y. Kou, *Coord. Chem. Rev.* **2010**, *254*, 1179-1218.
- [8] M. E. Grass, S. H. Joo, Y. W. Zhang, G. A. Somorjai, *J. Phys. Chem. C* **2009**, *113*, 8616-8623.
- [9] M. E. Grass, Y. W. Zhang, D. R. Butcher, J. Y. Park, Y. M. Li, H. Bluhm, K. M. Bratlie, T. F. Zhang, G. A. Somorjai, *Angew. Chem. Int. Ed.* **2008**, *47*, 8893-8896.
- [10] Y. Xia, Y. J. Xiong, B. Lim, S. E. Skrabalak, *Angew. Chem. Int. Ed.* **2009**, *48*, 60-103.
- [11] M. Boudart, in *Advances in Catalysis*, Vol. 20, Academic Press, **1969**, pp. 153-166.
- [12] M. Che, C. O. Bennett, in *Advances in Catalysis*, Vol. 36, Academic Press, **1989**, pp. 55-172.
- [13] K. Honkala, A. Hellman, I. N. Remediakis, A. Logadottir, A. Carlsson, S. Dahl, C. H. Christensen, J. K. Nørskov, *Science* **2005**, *307*, 555-558.
- [14] R. A. Van Santen, *Acc. Chem. Res.* **2008**, *42*, 57-66.
- [15] R. A. van Santen, M. Neurock, S. G. Shetty, *Chem. Rev.* **2010**, *110*, 2005-2048.
- [16] C. X. Xiao, H. Z. Wang, X. D. Mu, Y. Kou, *J. Catal.* **2007**, *250*, 25-32.
- [17] C. Zhao, H. Z. Wang, N. Yan, C. X. Xiao, X. D. Mu, P. J. Dyson, Y. Kou, *J. Catal.* **2007**, *250*, 33-40.
- [18] R. M. Rioux, H. Song, J. D. Hoefelmeyer, P. Yang, G. A. Somorjai, *J. Phys. Chem. B* **2005**, *109*, 2192-2202.
- [19] H. Song, R. M. Rioux, J. D. Hoefelmeyer, R. Komor, K. Niesz, M. Grass, P. D. Yang, G. A. Somorjai, *J. Am. Chem. Soc.* **2006**, *128*, 3027-3037.
- [20] R. M. Rioux, B. B. Hsu, M. E. Grass, H. Song, G. A. Somorjai, *Catal. Lett.* **2008**, *126*, 10-19.
- [21] N. Semagina, A. Renken, L. Kiwi-Minsker, *J. Phys. Chem. C* **2007**, *111*, 13933-13937.
- [22] A. J. Plomp, H. Vuori, A. O. I. Krause, K. P. de Jong, J. H. Bitter, *Appl. Catal. A* **2008**, *351*, 9-15.
- [23] Z. Guo, Y. T. Chen, L. S. Li, X. M. Wang, G. L. Haller, Y. H. Yang, *J. Catal.* **2010**, *276*, 314-326.
- [24] M. Grass, R. Rioux, G. Somorjai, *Catal. Lett.* **2009**, *128*, 1-8.
- [25] K. A. Manbeck, N. E. Musselwhite, L. M. Carl, C. A. Kauffman, O. D. Lyons, J. K. Navin, A. L. Marsh, *Appl. Catal. A* **2010**, *384*, 58-64.
- [26] J. Silvestre-Albero, G. Rupprechter, H. J. Freund, *Chem. Commun.* **2006**, 80-82.
- [27] N. Semagina, A. Renken, D. Laub, L. Kiwi-Minsker, *J. Catal.* **2007**, *246*, 308-314.
- [28] O. M. Wilson, M. R. Knecht, J. C. Garcia-Martinez, R. M. Crooks, *J. Am. Chem. Soc.* **2006**, *128*, 4510-4511.
- [29] P. S. Campbell, C. C. Santini, F. Bayard, Y. Chauvin, V. Colliere, A. Podgorsek, M. F. C. Gomes, J. Sa, *J. Catal.* **2010**, *275*, 99-107.

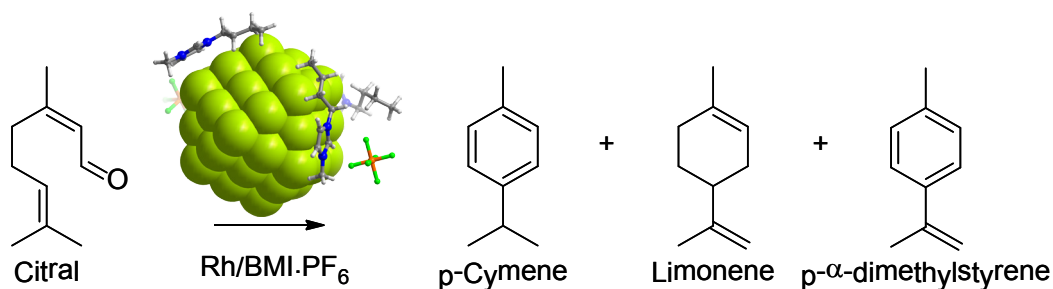
- [30] F. Hoxha, N. van Vegten, A. Urakawa, F. Krurneich, T. Mallat, A. Baiker, *J. Catal.* **2009**, *261*, 224-231.
- [31] H. B. Pan, C. M. Wai, *J. Phys. Chem. C* **2010**, *114*, 11364-11369.
- [32] C. Aliaga, J. Y. Park, Y. Yamada, H. S. Lee, C.-K. Tsung, P. Yang, G. A. Somorjai, *J. Phys. Chem. C* **2009**, *113*, 6150-6155.
- [33] J. J. F. Scholten, A. P. Pijpers, A. M. L. Hustings, *Cat. Rev. Sci. Eng.* **1985**, *27*, 151-206.
- [34] T. Iwamoto, K. Matsumoto, T. Matsushita, M. Inokuchi, N. Toshima, *J. Colloid Interface Sci.* **2009**, *336*, 879-888.
- [35] N. Zakarina, E. Bekturov, *Chin. J. Catal.* **2008**, *29*, 1165-1168.
- [36] Y. W. Zhang, M. E. Grass, S. E. Habas, F. Tao, T. F. Zhang, P. D. Yang, G. A. Somorjai, *J. Phys. Chem. C* **2007**, *111*, 12243-12253.
- [37] B. Chaudret, *Actualite Chimique* **1996**, 26-35.
- [38] M. L. Kahn, A. Glaria, C. Pages, M. Monge, L. Saint Macary, A. Maisonnat, B. Chaudret, *J. Mater. Chem.* **2009**, *19*, 4044-4060.
- [39] D. A. J. M. Ligthart, R. A. van Santen, E. J. M. Hensen, *Angew. Chem. Int. Ed.* **2011**, *50*, 5306-5310.
- [40] D. A. J. M. Ligthart, R. A. van Santen, E. J. M. Hensen, *J. Catal.* **2011**, *280*, 206-220.
- [41] X. Yang, N. Yan, Z. Fei, R. M. Crespo-Quesada, G. b. Laurenczy, L. Kiwi-Minsker, Y. Kou, Y. Li, P. J. Dyson, *Inorg. Chem.* **2008**, *47*, 7444-7446.
- [42] S. D. Jackson, L. A. Shaw, *Appl. Catal. A* **1996**, *134*, 91-99.
- [43] A. M. Goda, M. Neurock, M. A. Barteau, J. G. Chen, *Surf. Sci.* **2008**, *602*, 2513-2523.
- [44] I. Horiuti, M. Polanyi, *Transactions of the Faraday Society* **1934**, *30*, 1164-1172.
- [45] G. Iucci, V. Carravetta, G. Paolucci, A. Goldoni, M. V. Russo, G. Polzonetti, *Chem. Phys.* **2005**, *310*, 43-49.
- [46] V. Carravetta, G. Iucci, A. Ferri, M. V. Russo, S. Stranges, M. de Simone, G. Polzonetti, *Chem. Phys.* **2001**, *264*, 175-186.

Chapter 7

Ionic Liquid Stabilized Rh Nanoparticles for Citral Cyclodehydration

Summary

Cyclodehydration of citral has been achieved using rhodium nanoparticles dispersed in an imidazolium-based ionic liquid. Three cyclic products, namely *p*-cymene, *p*- α -dimethylstyrene and limonene were obtained with selectivity greater than 75%. The interaction between imidazolium cations and the reduced metal nanoparticles resulted in an acidic catalyst, which plays a similar function as a mineral acid. The activity of this novel system is one order of magnitude higher than that of diluted sulfuric acid but it undergo deactivation in subsequent runs.



7.1 Introduction

Citral is widely used in the fragrances and fine chemicals industry. Due to the presence of several unsaturated groups, citral has been investigated as a model compound for a wide array of reactions [1-6]. *p*-Cymene and *p*- α -dimethylstyrene are two useful products which can be obtained from citral by cyclodehydration. *p*-Cymene and *p*- α -dimethylstyrene are important starting chemicals to produce fragrances, pharmaceuticals and fine chemicals. These compounds can be obtained by ring closure of the isolated olefin and carbonyl group of citral [5]. Cyclodehydration was first observed by Semmler in 1891 using potassium hydrogen sulphate [7] and was later reported with mineral acid catalysts [5-6, 8]. Currently, *p*-cymene is produced by alkylation of toluene and Friedel-Crafts alkylation of benzene. *p*- α -Dimethylstyrene can be obtained by the dehydrogenation of *p*-cymene [9] or limonene [10].

Ionic Liquids (ILs) are promising reaction media for a variety of catalytic reactions [11-19]. ILs are also known to stabilize metal nanoparticles, which for instance exhibit high activity in hydrogenation reactions [20-23]. The ILs may also act as ligands modifying the product selectivity [23-24]. Rh is a very active metal for citral hydrogenation. Rh nanoparticles supported on inorganic oxides favor the hydrogenation of the conjugated C=C bond in citral to produce citronellal [25-27]. Modifiers [26-29] change the product selectivity to geraniol and nerol by favoring hydrogenation of the carbonyl bond. Other systems [1-3] promote the conversion of citral to products such as menthol. Herein we report that Rh nanoparticles stabilized by 1-*n*-butyl-3-methylimidazolium hexafluorophosphate (BMI·PF₆) are very active and efficient catalysts for the cyclodehydration of citral. The combination of the presumed acidic function with the metal results in ring closure and dehydrogenation of citral.

7.2 Experimental Methods

7.2.1 Synthesis of Materials

Rh nanoparticles using ILs as stabilizer

Ionic liquid stabilized rhodium nanoparticles were prepared according to a modified procedure published by Roucoux et al. [20] In a typical experiment, RhCl₃·*n*H₂O (10 mg) was dissolved in THF (5 mL) and imidazolium based ionic liquid (2 mL). Sodium borohydride (3.6 mg) dissolved in water (20 μ L) was added to the mixture under vigorous stirring at ambient conditions. The colloidal mixture was then dried under vacuum for 2 h to remove THF and other impurities.

Rh nanoparticles using P123 as stabilizer

Rh nanoparticles stabilized by P123 were synthesized based on a modified method reported by Li et al. [30]. In a typical experiment, $\text{RhCl}_3 \cdot n\text{H}_2\text{O}$ (20 mg) was dissolved in distilled water (6 mL). The RhCl_3 solution was then added to ethylene glycol (14 mL) and P123 (1.86 g). The mixture was stirred in a 50 °C water bath until all the P123 were dissolved. The mixture was then allowed to cool to room temperature before adding 0.5 M NaBH_4 solution (2 mL) dropwise under vigorous stirring. After stirring for 5 min, ethanol was added to the mixture and the Rh nanoparticles were washed with acetone and collected by centrifugation. The isolated Rh nanoparticles were then re-dispersed in methanol (5 mL).

Rh nanoparticles without stabilizer

Typically, $\text{RhCl}_3 \cdot n\text{H}_2\text{O}$ (10 mg) was dissolved in distilled water (3 mL) and ethylene glycol (7 mL). 0.5 M NaBH_4 solution (1 mL) was added dropwise under vigorous stirring. After stirring for 5 min, ethanol was added to the mixture and the Rh nanoparticles were washed with acetone and collected by centrifugation. The isolated Rh nanoparticles were then dried and re-dispersed in methanol (2 mL). These unprotected Rh nanoparticles were re-dispersed in ILs by adding specific amount of Rh nanoparticles solution to IL (1 mL). The resultant mixture was then dried under vacuum for more than 3 h to remove methanol before using as catalyst (named Rh+ PF_6).

RhO_x particles

RhO_x particles were synthesized according to literature [31]. $\text{RhCl}_3 \cdot n\text{H}_2\text{O}$ (10 mg) was dissolved in distilled water. Rh^{3+} was precipitated by adding 0.1 M of NaOH solution dropwise to the solution (to pH 10). The precipitate was aged at room temperature for 1 h, and then washed and dried at 60 °C for 48 h, followed by calcination at 500 °C for 2 h. The resultant RhO_x was verified by powder XRD.

7.2.2 Characterization

Transmission electron microscopy (TEM) was performed on FEI Tecnai 20 electron microscope at an acceleration voltage of 200 kV with a LaB_6 filament. The Rh particles were isolated by dissolving a small amount of the sample in methanol and collected by centrifugation. The isolated particles were then redispersed in ethanol and dried over a carbon-coated Cu grid. Particle size distribution was obtained by measuring more than 100 particles.

7.2.3 Catalytic Activity Measurements

The liquid phase cyclodehydration of citral was carried out using a batch-type reactor operated under atmospheric condition. Citral (1 mmol), Rh catalyst (0.019 mmol) in ILs (1 mL), *n*-octane (as internal standard, 0.1 mmol) and *n*-heptane (15 mL) were introduced into a round-bottom flask, followed by bubbling pure molecular hydrogen or helium (20 mL/min) under vigorous magnetic stirring (500 rpm). The reaction was carried out at 70 °C for 6 h.

High-pressure reactions were carried out at 20 bar and 70 °C for 2 h using a stainless steel autoclave. Citral (1 mmol), Rh catalyst (0.019 mmol) in IL (1 mL), *n*-octane (0.1 mmol) and *n*-heptane (5 mL) were introduced into the autoclave. The autoclave was flushed with H₂ for 3 times before reaction.

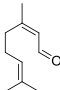
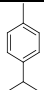
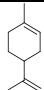
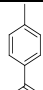
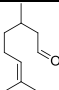
Recyclability tests were performed by partially extracting the top liquid followed by washing of the catalyst with methanol and ultrasound for 10 min. The catalyst was recovered by drying the mixture under vacuum for more than 3 h.

Reaction samples were analyzed by gas chromatograph – mass spectrometry (QP5050, Shimadzu) equipped with a CP-Sil 8CB capillary column (30 m × 0.32 mm, film thickness 0.5 µm). The identification of citral, *p*-cymene, limonene and *p*- α -dimethylstyrene was established by GC-MS and by the retention time of authenticate samples. Quantitative analysis of the citral, *p*-cymene, limonene and *p*- α -dimethylstyrene was established by using authenticate samples and *n*-octane (0.1 mmol) as the internal standard.

7.3 Results and Discussion

In the course of our investigations, we observed that the hydrogenation of citral in *n*-heptane at 70 °C under 1 atm H₂ using 1.8 nm BMI·PF₆ stabilized Rh nanoparticles reduced by NaBH₄ (Figure 7.1a,b) did not give the expected hydrogenation products (Table 7.1, GC-MS spectra in Figure 7.2). Instead, this catalyst afforded *p*-cymene, limonene and *p*- α -dimethylstyrene with respective selectivities of 41%, 12% and 14% at a citral conversion of 90%. The remaining products are side products including hydrogenation products. As the main products were not those expected from citral hydrogenation, the reaction was repeated under inert gas (Rh-PF₆-He). The selectivity to the dehydrogenation product *p*- α -dimethylstyrene increases at the expense of hydrogenation products. The other products are now mainly intermediates of cyclodehydration (see below). An experiment with aqueous H₂SO₄ also yielded *p*-cymene, limonene and *p*- α -dimethylstyrene but with lower selectivity.

The reaction by an equimolar amount of H^+ compared to Rh proceeds very sluggishly (H_2SO_4 -He).

Table 7.1. Performance of Rh catalyzed citral transformation. ^[a]						
Catalyst	Conversion (%)	Selectivity (%)				
		 citral	 <i>p</i> -cymene	 limonene	 <i>p</i> - α -dimethylstyrene	 citronellal
Rh-PF ₆ -H ₂	90	41	12	14	—	34 ^[b]
Rh-PF ₆ -He	84	47	9	23	—	21
Rh+PF ₆ -He ^[c]	87	48	8	21	—	23
Rh-PF ₆ -0.5 ^[d]	17	54	12	32	—	2
Extract-2 ^[e]	21	45	14	25	—	16
Rh-P123-H ₂	42	4	1	3	92	—
Rh-P123+PF ₆ -H ₂	13	30	3	8	59	—
Rh-PF ₆ -HP-H ₂ ^[f]	98	21	14	5	—	59 ^[g]
PF ₆ -He ^[h]	—	—	—	—	—	—
H ₂ SO ₄ -He	8	24	9	20	—	48

[a] Citral (1 mmol), octane (0.1 mmol), Rh/citral molar ratio (0.019), IL (1 mL), *n*-heptane (15 mL), *T* = 70 °C, *t* = 6 h, 1 atm, gas flow (20 mL/min). [b] Hydrogenation products of citral, *p*-cymene, limonene and *p*- α -dimethylstyrene. [c] Unprotected Rh nanoparticles (0.019 mmol) redispersed in 1 mL BMI·PF₆. [d] Reaction time (*t* = 0.5 h). [e] Organic fraction extracted from Rh-PF₆-0.5 and further reacted for 2 h. [f] 20 bar H₂, *t* = 2 h. [g] Main products: menthane, isomers of menthene, menthenol and 3,7-dimethyl-1-octanol. [h] BMI·PF₆ (1 mL).

Further experiments focused on establishing the unique nature of this novel catalytic system. Dissolved RhCl₃ and RhO_x dispersed in BMI·PF₆ ILs did not convert citral. The activity of the BMI·PF₆ IL was also negligible. These findings show that metallic Rh is a prerequisite. In order to investigate the role of the IL, 4.3 nm Rh nanoparticles were prepared in a similar manner but without the ionic liquid (Figure 7.1c,d). Citral was not converted by these nanoparticles under similar conditions. When these Rh nanoparticles were redispersed in BMI·PF₆ (Rh+PF₆-He), similar cyclodehydration products were obtained as in the Rh-PF₆-He experiment. This result shows that the reactivity is related to the interaction between metallic Rh and IL. Dupont et al. reported that in the presence of water HF may be formed during the synthesis of PF₆-based IL stabilized metal nanoparticles [32]. To exclude such possibility, the cyclodehydration of citral was carried out using Rh-PF₆ for 0.5 h (Rh-PF₆-0.5), followed by the extraction of the top liquid at the reaction temperature. The extract was

then allowed to react for another 2 h (Extract-2). The conversion did not increase further, which eliminates the possibility of homogeneous catalysis by HF or dissolved Rh.

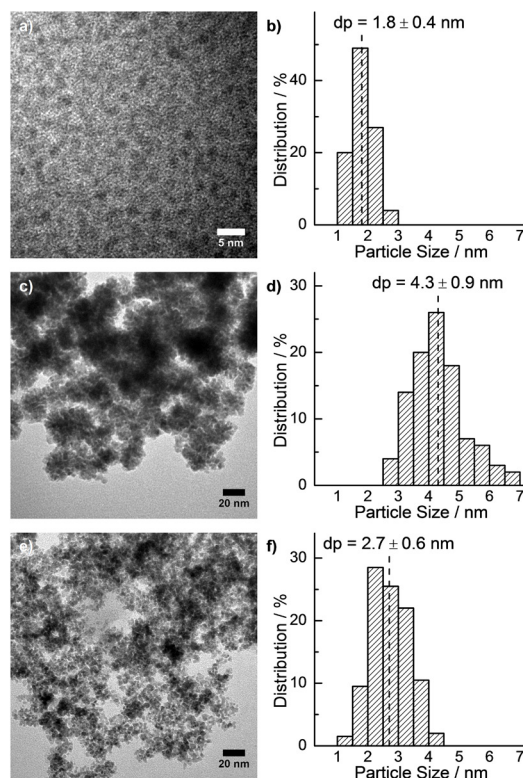


Figure 7.1: Rh nanoparticles: (a,c,e) Electron micrograph; (b,d,f) particle size distribution; (a,b) BMI·PF₆ stabilized (a,b) stabilizer free (c,d) P123 stabilized (e,f).

A synergetic effect between Rh nanoparticles and the IL becomes evident from these results. In yet another experiment we stabilized 2.7 nm Rh nanoparticles by the triblock copolymer P123 (Figure 7.1e,f). Without any ILs, these Rh nanoparticles were shown to be a very active hydrogenation catalyst (Rh-P123-H₂) giving more than 90% selectivity to citronellal at 42% citral conversion. This catalyst was then redispersed in BMI·PF₆ (Rh-P123+PF₆-H₂) and we found that the *p*-cymene selectivity was increased substantially at the expense of the hydrogenation selectivity. The reduced hydrogenation activity in the presence of BMI·PF₆ for Rh-P123 catalysts is likely due to the low solubility of H₂ in ionic liquid at atmospheric pressure. This explains the absence of hydrogenated products for the Rh-PF₆-H₂ catalyst. In this case, cyclodehydration is preferred over hydrogenation. Using IL stabilized Pd nanoparticles, Virtanen et al. obtained citral cyclohydrogenation products such as menthol and isopulegol at elevated H₂ pressure [3]. To establish the effect of pressure, we carried out citral hydrogenation at 20 bar H₂ (Rh-PF₆-HP-H₂) which gave a citral conversion of 98% after 2 h. The selectivity to *p*-cymene was lower than in the corresponding atmospheric-pressure experiments. The use of high pressure H₂ favors the hydrogenation of

cyclodehydration products, which led to the formation of menthane as well as isomers of menthene and menthenol. A previous study has shown that imidazolium based ILs interact so strongly with Ir nanoparticles that transient surface carbenes are formed [33]. This activation of IL may lead to new catalytic properties and, in particular, the formation of Brønsted acidity is relevant to the chemistry described here.

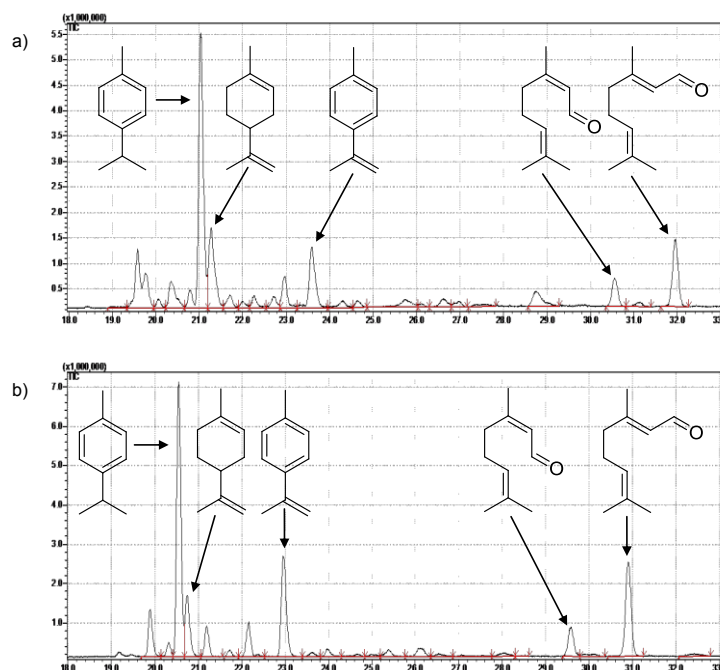
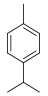
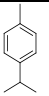
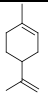
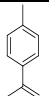


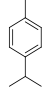
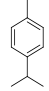
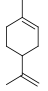
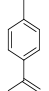
Figure 7.2: GC-MS spectra for citral cyclodehydration reaction catalyzed by (a) Rh-PF₆-H₂ (b) Rh-PF₆-He.

In an attempt to establish the critical role of BMI·PF₆, Rh nanoparticles were stabilized by different imidazolium based ILs (Table 7.2). Amyes et al. have shown that imidazolium cations may act as weak acids due to proton exchange at the C₂ position as shown by their H/D exchange in the presence of water [34]. This kind of acidity is enhanced in the presence of metals such as Ir [33]. To investigate the role of C₂-H in citral hydrogenation, it was replaced by a methyl group. When 1-butyl-2,3-dimethylimidazolium hexafluorophosphate (BM₂I·PF₆) was the IL (Rh-BM₂I·PF₆), the citral conversion was lower at 53% with a selectivity towards cyclic products of 90%, considerably higher than for Rh/BMI·PF₆. This suggests that the acidity of the C₂ hydrogen is not unique. Protons of the C₂-methyl group of BM₂I are also slightly acidic [18, 35-36], which explains the lower activity of the Rh-BM₂I·PF₆ system. In addition, protons in other positions such as those at the C₄, C₅ and C₈ atoms are also able to undergo H/D exchange [33].

To further investigate the role of the ILs, different counter anions were used to stabilize the Rh nanoparticles. Results show that the cyclodehydration of citral decreases in

Table 7.2. Performance of Rh catalyzed citral cyclodehydration using different ionic liquids. ^[a]					
Counter anion	Conversion (%)	Selectivity (%)			
		 citral	 <i>p</i> -cymene	 limonene	 <i>p</i> - α -dimethylstyrene
PF ₆	84	47	9	23	21
BM ₂ I-PF ₆	53	79	8	7	6
BF ₄	4	4	9	11	79
OTf	6	11	18	25	46
NTf ₂	25	22	20	18	41
[a] Citral (1 mmol), octane (0.1 mmol), Rh/citral molar ratio (0.019), IL (1 mL), <i>n</i> -heptane (15 mL), <i>T</i> = 70 °C, <i>t</i> = 6 h, 1 atm, He flow (20 mL/min).					

the order Rh-PF₆ >> Rh-NTf₂ > Rh-BF₄ ~ Rh-OTf. The activity increases with decreasing strength of the interaction of the imidazolium cation and the counter anion [37]. The citral cyclodehydration activity with the BF₄⁻ ion is negligible. This result corresponds to the finding that in this case the BMI part of the IL does not undergo H/D exchange [18, 35-36]. Evidently cyclodehydration of citral is affected by acidity of the imidazolium cation, which is strongly influenced by the presence of the metal as well as the strength of the interaction with the counter anion.

Table 7.3. Investigation of the recyclability of Rh-PF ₆ catalyst. ^[a]					
Experiment	Conversion (%)	Selectivity (%)			
	 citral	 <i>p</i> -cymene	 limonene	 <i>p</i> - α -dimethylstyrene	Other Cyclic
Rh-PF ₆ -1	84	47	9	23	21
Rh-PF ₆ -2	41	66	13	22	–
Rh-PF ₆ -3	29	62	19	19	–
Rh-PF ₆ -4	15	55	24	21	–
Rh-PF ₆ -5+PF ₆ ^[b]	12	42	24	35	–
[a] Reaction conditions: Citral (1 mmol), octane (0.1 mmol), Rh/citral molar ratio (0.019), IL (1 mL), n-heptane (15 mL), T = 70 °C, t = 6 h, He flow rate under atmospheric pressure (20 mL/min). [b] BMI·PF ₆ (1 mL) was added to the spent catalyst during the fifth cycle.					

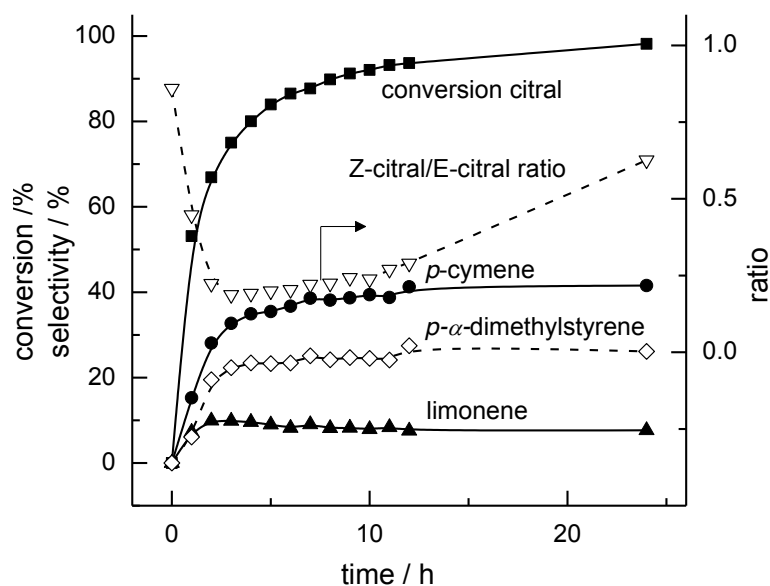
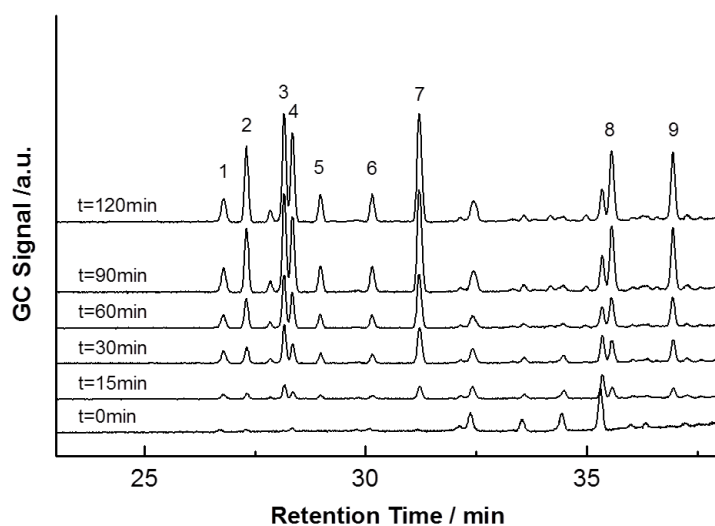


Figure 7.3: Time-on-stream reaction profile using Rh-PF₆-He catalyst.



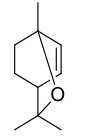
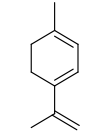
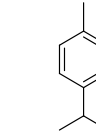
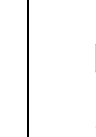
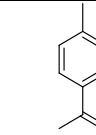
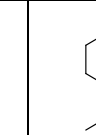
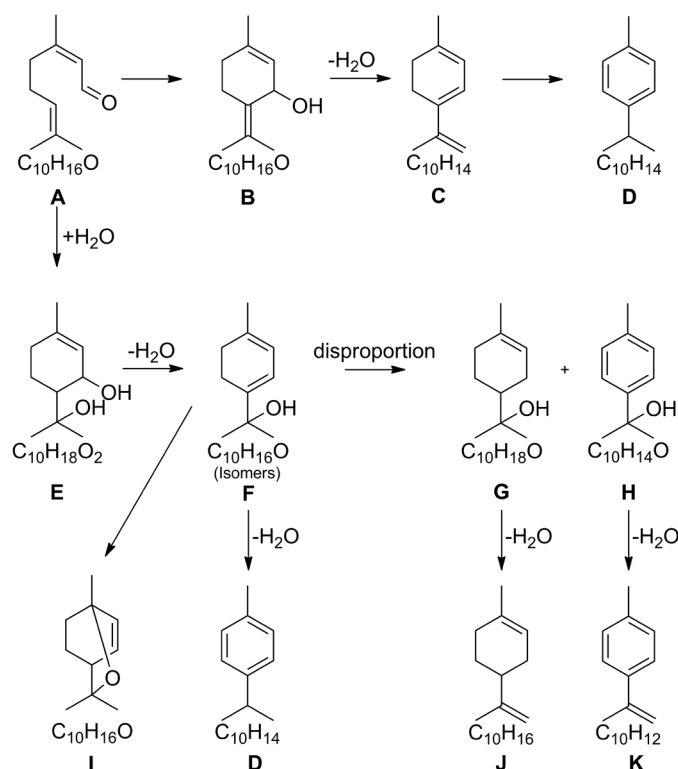
Components				
Peak Number	1	2	3	4
Components	Unknown	Unknown		
Peak Number	5	6	7	8, 9

Figure 7.4: GC-MS spectra of citral cyclodehydration products with time-on-stream using Rh-PF₆-catalyst.

The possibility to recycle the Rh-PF₆ catalyst was investigated in five consecutive runs (Table 7.3). The conversion of citral decreased during subsequent cycles. During the fifth run, 1 mL BMI·PF₆ was introduced to the spent catalyst (Rh-PF₆-5+PF₆). We

anticipated that, if the deactivation would be caused by the consumption or deactivation of $\text{BMI} \cdot \text{PF}_6$, addition of $\text{BMI} \cdot \text{PF}_6$ would significantly restore catalytic activity. However, a further decline in citral conversion was observed. Similar to the observation made by Dupont et al. [38], separation of large Rh particles from the suspension was observed. This suggests that sintering of the stabilized Rh particle is the main cause of catalyst deactivation. Another reason for deactivation may be due to the poisoning effect of the intermediate products [39]. Note that the selectivity to cyclic product was 100% after the first cycle.



Scheme 7.1: Proposed reaction mechanism for cyclodehydration of citral.

p- α -Dimethylstyrene is the product of dehydrogenation of *p*-cymene and *p*-cymene that of limonene. Time-on-stream experiments (Figure 7.3) reveal that *p*-cymene, limonene and *p*- α -dimethylstyrene are not formed according such a consecutive reaction mechanism. Initially, *p*-cymene is the dominant product. The rapid decrease of the ratio of *Z*-citral and *E*-citral directly after the start of reaction indicates that cyclization of the *Z* isomer occurs. We hypothesize that the reaction mechanism for the cyclodehydration of citral using $\text{Rh} \cdot \text{PF}_6$ catalyst is similar to that proposed for mineral acids (Scheme 7.1) [5, 8]. This mechanism includes cyclodehydration to *p*-cymene and a pathway involving hydration towards *p*-menthadienol which can disproportionate into limonene and *p*- α -dimethylstyrene. *p*-Cymene is also a product of *p*-menthadienol dehydration. Figure 7.2 confirms that the latter products

are initially formed in equimolar amounts. As the reaction progresses, limonene is dehydrogenated to *p*-cymene and *p*- α -dimethylstyrene. This was verified with an independent experiment using limonene as the substrate in the presence of Rh-PF₆ catalyst, where *p*-cymene and *p*- α -dimethylstyrene were obtained. A detailed product analysis (Figure 7.4) evidences the presence of additional products such as 2,3-dehydro-1,8-cineole (**I**), *p*-menthatriene (**C**) and the two isomers of *p*-menthadienol (**F**). Two further products could not be unequivocally identified, but we surmise that these are the two isomers of compound G given their mass spectra and molecular weight of 154.

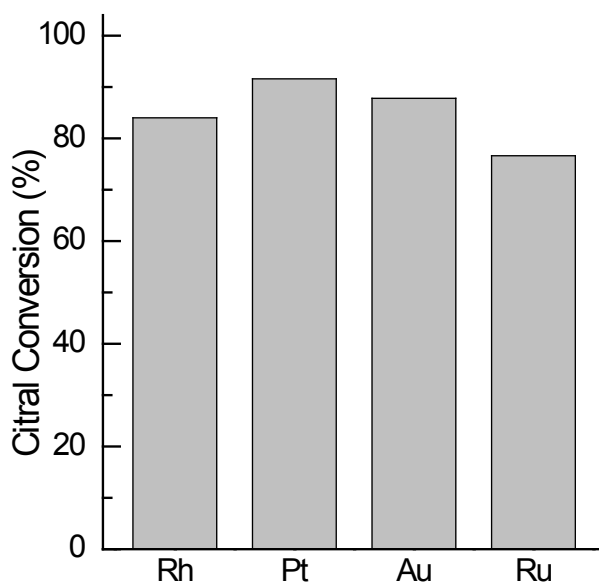


Figure 7.4: Activity for citral cyclodehydration catalyzed by BMI·PF₆ stabilized metal nanoparticles.

Rh, Ru, Pt and Au nanoparticles stabilized by BMI·PF₆ were also investigated for the cyclodehydration of citral (Figure 7.4). Results show that these transition metals stabilized by BMI·PF₆ is also able to catalyze the cyclodehydration of citral. The use of different transition metal have only minute impact on the activity for the cyclodehydration of citral. Greater than 75% selectivity towards cyclodehydration products were maintained for all four transition metal particles.

7.4 Conclusion

In summary, the selective cyclodehydration of citral to *p*-cymene, limonene and *p*- α -dimethylstyrene was successfully demonstrated using BMI·PF₆ stabilized Rh nanoparticles. This catalyst outperforms a mineral acid such as aqueous H₂SO₄. Essential ingredients in this catalytic system are an imidazolium based cation in combination with a metal which renders an acidic catalyst. The data suggest that the metal stabilizes a carbene-type intermediate

giving rise to enhanced Brønsted acidity compared to the metal-free case. The counter anion of the IL should not interact too strongly with the organic cation. The reaction proceeds by ring closure of *Z*-citral and dehydration to *p*-menthatriene which isomerizes to *p*-cymene. The eliminated water catalyzes the parallel reaction path to *p*-menthadienol that amongst others disproportionate to limonene and *p*- α -dimethylstyrene.

7.5 References

- [1] Y. T. Nie, S. Jaenicke, G. K. Chuah, *Chem. Eur. J.* **2009**, *15*, 1991-1999.
- [2] A. F. Trasarti, A. J. Marchi, C. R. Apesteguia, *J. Catal.* **2007**, *247*, 155-165.
- [3] P. Virtanen, H. Karhu, G. Toth, K. Kordas, J. P. Mikkola, *J. Catal.* **2009**, *263*, 209-219.
- [4] A. Corma, S. Iborra, A. Velty, *Chem. Rev.* **2007**, *107*, 2411-2502.
- [5] D. A. Baines, R. A. Jones, T. C. Webb, Campions.Ih, *Tetrahedron* **1970**, *26*, 4901-4913.
- [6] B. C. Clark, C. C. Powell, T. Radford, *Tetrahedron* **1977**, *33*, 2187-2191.
- [7] F. W. Semmler, *Berichte der deutschen chemischen Gesellschaft* **1891**, *24*, 201-211.
- [8] K. Kimura, H. Nishimura, I. Iwata, J. Mizutani, *J. Agric. Food. Chem.* **1983**, *31*, 801-804.
- [9] M. J. Lawrenson, Smith, Paul Christopher J. (BP Chemicals Limited), European Patent EP0460827, **1994**.
- [10] P. Horrillo-Martínez, M.-A. Virolleaud, C. Jaekel, *ChemCatChem* **2010**, *2*, 175-181.
- [11] D. B. Zhao, M. Wu, Y. Kou, E. Min, *Catal. Today* **2002**, *74*, 157-189.
- [12] T. Welton, *Coord. Chem. Rev.* **2004**, *248*, 2459-2477.
- [13] H. Weingärtner, *Angew. Chem. Int. Ed.* **2008**, *47*, 654-670.
- [14] K. A. D. Swift, *Top. Catal.* **2004**, *27*, 143-155.
- [15] R. A. Sheldon, *Green Chem.* **2005**, *7*, 267-278.
- [16] V. I. Parvulescu, C. Hardacre, *Chem. Rev.* **2007**, *107*, 2615-2665.
- [17] Y. L. Gu, G. X. Li, *Adv. Synth. Catal.* **2009**, *351*, 817-847.
- [18] S. Sowmiah, V. Srinivasadesikan, M. C. Tseng, Y. H. Chu, *Molecules* **2009**, *14*, 3780-3813.
- [19] Z. Ma, J. Yu, S. Dai, *Adv. Mater.* **2010**, *22*, 261-285.
- [20] B. Leger, A. Denicourt-Nowicki, H. Olivier-Bourbigou, A. Roucoux, *Inorg. Chem.* **2008**, *47*, 9090-9096.
- [21] B. Leger, A. Denicourt-Nowicki, H. Olivier-Bourbigou, A. Roucoux, *Tetrahedron Lett.* **2009**, *50*, 6531-6533.
- [22] V. Mevellec, A. Roucoux, E. Ramirez, K. Philippot, B. Chaudret, *Adv. Synth. Catal.* **2004**, *346*, 72-76.
- [23] J. P. Mikkola, P. Virtanen, H. Karhu, T. Salmi, D. Y. Murzin, *Green Chem.* **2006**, *8*, 197-205.
- [24] P. H. Li, L. Wang, M. Wang, Y. C. Zhang, *Eur. J. Org. Chem.* **2008**, 1157-1160.
- [25] P. Maki-Arvela, L. P. Tiainen, A. K. Neyestanaki, R. Sjöholm, T. K. Rantakyla, E. Laine, T. Salmi, D. Y. Murzin, *Appl. Catal. A* **2002**, *237*, 181-200.
- [26] G. Lafaye, T. Ekou, C. Micheaud-Especel, C. Montassier, P. Marecot, *Appl. Catal. A* **2004**, *257*, 107-117.
- [27] T. Ekou, A. Vicente, G. Lafaye, C. Especel, P. Marecot, *Appl. Catal. A* **2006**, *314*, 64-72.
- [28] M. Steffan, M. Lucas, A. Brandner, M. Wollny, N. Oldenburg, P. Claus, *Chem. Eng. Technol.* **2007**, *30*, 481-486.
- [29] L. Sordelli, R. Psaro, G. Vlaic, A. Cepparo, S. Recchia, C. Dossi, A. Fusi, R. Zanon, *J. Catal.* **1999**, *182*, 186-198.
- [30] Y. Chen, K. Y. Liew, J. L. Li, *Appl. Surf. Sci.* **2009**, *255*, 4039-4044.
- [31] S. Music, A. Saric, S. Popovic, M. Ivanda, *J. Mol. Struct.* **2009**, *924-926*, 221-224.
- [32] G. S. Fonseca, A. P. Umpierre, P. F. P. Fichtner, S. R. Teixeira, J. Dupont, *Chem. Eur. J.* **2003**, *9*, 3263-3269.
- [33] L. S. Ott, M. L. Cline, M. Deetlefs, K. R. Seddon, R. G. Finke, *J. Am. Chem. Soc.* **2005**, *127*, 5758-5759.
- [34] T. L. Amyes, S. T. Diver, J. P. Richard, F. M. Rivas, K. Toth, *J. Am. Chem. Soc.* **2004**, *126*, 4366-4374.
- [35] S. T. Handy, M. Okello, *J. Org. Chem.* **2005**, *70*, 1915-1918.
- [36] J. Y. Cheng, Y. H. Chu, *Tetrahedron Lett.* **2006**, *47*, 1575-1579.
- [37] S. Tsuzuki, H. Tokuda, K. Hayamizu, M. Watanabe, *J. Phys. Chem. B* **2005**, *109*, 16474-16481.
- [38] P. Migowski, J. Dupont, *Chem. Eur. J.* **2007**, *13*, 32-39.
- [39] P. Forzatti, L. Lietti, *Catal. Today* **1999**, *52*, 165-181.

Summary

Structure Sensitivity in Nanoparticle Catalysis

For Fischer-Tropsch and other Hydrogenation Reactions

Catalysis plays a pivotal role in meeting our energy demand in the past and will continue to be of paramount importance in shifting to more diverse and greener feedstocks. Fischer-Tropsch (FT) synthesis offers an attractive route to produce fuels and chemicals from syngas (a mixture of CO and H₂), which can be derived from natural gas, coal and biomass. Ru is the most active transition metal for the FT reaction catalyzing the formation of long chain products in three main reaction steps: (1) initiation, (2) chain growth and (3) chain termination. The steps involved in the FT reaction bear resemblance to other polymerization processes, except that in FT synthesis, the monomer is produced by CO dissociation. Due to the complexity of the FT reaction, the understanding of the role of the catalyst at the molecular level is extremely challenging. In particular, the origin of the particle size dependence and the formation of side-products such as oxygenates during FT have not been elucidated yet. This thesis explores structure sensitivity of nanoparticle catalysis for several chemical reactions, including Fischer-Tropsch synthesis in the aqueous phase.

Chapter 2 explains the origin of the unprecedented oxygenate selectivity observed in aqueous phase FT, catalyzed by a colloidal Ru catalyst. Low temperature operations resulted in high oxygenate selectivity (about 70%). The very different kinetic parameters for the formation of oxygenates and hydrocarbons strongly point to the involvement of different catalytic reaction centers. By considering molecular kinetics, oxygenates (hydrocarbons) are proposed to be formed on sites with high (low) barrier for CO dissociation.

Subject of further study was the catalytic performance of the FT reaction with changing Ru particle size, which is discussed in Chapter 3 and 4. Chapter 3 describes the preparation and characterization of PVP-stabilized Ru nanoparticles. Ru nanoparticles between 1 to 5 nm were prepared by polyol reduction of different Ru salts at various temperatures. The colloidal Ru catalysts were characterized by transmission electron microscopy, FTIR of adsorbed CO, X-ray absorption spectroscopy and X-ray Diffraction combined with structural analysis. XANES shows that all catalysts were nearly in completely

reduced state, after a second reduction using high-pressure H_2 in an autoclave batch reactor. The characterization data shows an increasing concentration of coordinatively unsaturated sites with decreasing particle size. The Ru-Ru distances of the first coordination shell obtained from XRD-PDF are in agreement with the results obtained from EXAFS. The structure of the Ru nanoparticles was resolved by applying reversed Monte Carlo fitting of the XRD-PDF data. The resolved structure of the Ru nanoparticles revealed that particles have a *hcp* structure but their structural disorder increases with decreasing particle size. The comparison of different size nanoparticles shows a highly disordered surface structure, which is very different from the surfaces usually considered when modeling reactions on the surface of nanoparticles.

Chapter 4 relates the change in the FT reactivity to the structural information of the Ru catalyst depicted in Chapter 3. Activity and selectivity of aqueous phase FT are strongly dependent on the Ru particle size, in the range of 1 to 5 nm. From the resolved structure of the Ru particles, it is concluded that activity scales linearly with the density of step edge sites. The rate of FT normalized to the fraction of step edge sites is found to be independent of particle size. Oxygenates selectivity is found to decrease with increasing particle size. The ASF chain growth parameter of oxygenates is lower than that of hydrocarbon for all particle sizes. The chain growth parameter for hydrocarbon formation is independent of particle size but is constant for oxygenates only for particles larger than 3 nm. The lower chain growth probability for oxygenates of small particles is related to the higher methane selectivity. These results supports earlier claims that two different reaction centers are involved in the formation of hydrocarbons and oxygenates. Lumped kinetic model was developed to account for the growth of hydrocarbons and oxygenates at different reactive centers.

The use of Ru nanoparticles for liquid phase operations requires the use of organic capping agent. Chapter 5 investigates the effect of organic capping agent on FT activity in the aqueous phase. To exclude effects of particle size, the capping agents were placed on carbon nanofiber supported Ru nanoparticles of 3.4 nm. It is established that increasing the interacting strength between the capping agent and the surface of the Ru particles, FT activity decreases: polyvinylpyrrolidone as the stabilizer can decrease activity up to 50%, whereas stabilizer containing thiol and/or sulfonate strongly suppresses activity. Despite these changes, kinetic data suggests that the FT mechanism is largely unaffected by the presence of capping agents. The presence of these organic capping agents on the catalyst has only small influence on the selectivity. It is also found that replacing water with n-hexadecane as the solvent results in an increase of the rate of formation and a decrease in the chain growth

probability for hydrocarbons, whilst the production of oxygenates is unaffected. This trend is consistent with the proposal that hydrocarbons are formed on reaction centers, which involves facile CO dissociation and it is the termination step that controls the rate of reaction. For oxygenates, CO dissociation is proposed to be the rate controlling step.

Chapter 6 focuses on the effect of Rh particle size on the hydrogenation of phenylacetylene and 1-octene. A series of Rh nanoparticles with sizes between 3.5 to 11.4 nm were synthesized in the presence of polyvinylpyrrolidone. The reaction is zeroth order in the reactant for phenylacetylene and 1-octene. The catalytic activity increased with Rh particle size for phenylacetylene hydrogenation, but remained constant for 1-octene hydrogenation. The possible explanations for this different behavior towards change in particle size are discussed.

Chapter 7 illustrates an extreme example of the influence of the organic capping agent, where Rh nanoparticles stabilized by an imidazolium-based ionic-liquid (IL) acts as an acid catalyst. When benchmarked against other Rh catalysts with comparable particle sizes, the IL stabilized Rh nanoparticles exhibit lower activity in citral hydrogenation. However, such catalyst was found to be extremely active for the cyclodehydration of citral. The catalytic activity is argued to be due to acidity generation by interaction of imidazolium cations and metal nanoparticles.

For the very first time, this work has revealed extensive knowledge behind the formation of oxygenates and the origin of particle size effect during the FT reaction. Different catalytic centers with different rate limiting steps, are found to be responsible for the formation of oxygenates and hydrocarbons. The FT activity is found to increase with the fraction of specific coordinately uncoordinated sites on the catalyst, where activity normalized to these sites are found to be independent of particle size effect. These valuable molecular understanding on the FT reaction will play a significant role in the future development of a more active FT catalyst and hold the possibility of tuning the selectivity of the reaction to preferentially form hydrocarbons or oxygenates.

Acknowledgement

I would like to begin by sharing a quote from Dr. Daisaku Ikeda (Buddhist philosopher), which I strongly stand by, “Life can unfold unlimitedly as long as we have a heart of appreciation and an undefeated mind.” For me, this thesis does not mark the end, but the start of a new chapter in my life. All of this would not be made possible without the support from all the people I have mentioned in this book.

First and foremost, I would like to express my sincere gratitude to Prof.dr.ir. Emiel Hensen for granting me this opportunity to pursue a PhD with the Schuit Institute of Catalysis in Eindhoven University of Technology. Besides a great mentor, I see Emiel as an admirable sparring partner during our discussions. We came from very different cultures, backgrounds and sometimes different way of thinking but we share the same passion for science, hence I truly enjoyed working with him. I am very grateful for the trust he put on me, which has enabled me to explore interesting areas outside my scope of work. His enthusiasm, meticulousness and devotion for seeking the truth in science has inspired me to want to further develop myself professionally as a scientist.

Prof.dr. Rutger van Santen is a man that not only has so much wisdom inside him, he also has a noble heart to share his immense knowledge and nurture young people. He has showed me the importance of modelling and the possibility of developing kinetic equations by simplifying complex reactions. His in-depth knowledge and valuable views on Fischer-Tropsch, especially on the mechanistic aspects, have always spurred me to look deeper into my results and find loopholes in my hypothesis. Thanks to his kind guidance, I get to bring with me valuable attributes for a good scientist.

It is with immense gratitude that I acknowledge the other members of my defence committee – Prof. Harry Bitter, Prof. Krijn de Jong, Prof. Guido Mul, Prof. Hans Niemantsverdriet, Prof. Jaap Schouten and Dr. Xander Nijhuis for taking their precious time to evaluate my thesis and attend my defence.

I consider it an honour to work with the members in the Fischer-Tropsch subgroup, namely Yejun, Robert, Michel, Ivo, Abdul, Wei, Jeroen and Arno (Arnie). I appreciate the productive and enthusiastic discussions we had during our subgroup meetings and also during one to one discussions. Yejun and I were the only two persons working on Fischer-Tropsch when I first started my PhD. We hit off really well from the start. I am grateful to him for a

smooth start of my PhD life. Robert and I had our fair share of different views and disagreements initially but we eventually found a way to work things out together. I really appreciate his help to review my work meticulously and also for offering alternative view. Other than the late nights in the laboratory and collaboration works, I really got to know Michel a lot better during our Grenoble trips and also during the conference in Detroit. It was enjoyable to work with Ivo on both scientific and non-scientific stuff, including the discussion about our “parameter”, during the conference in South Africa. It was my pleasure to work with Evgeny in the final few months, on a side project related to Fischer-Tropsch.

One of the memorable part of my PhD life was with the Grenoble gang – Volkan, Michel, Asegul, Johan, Tiny, Arno and Wei. It was very nice to work with all of them under the pressure of time to get things. I have really learnt a lot from them. My “Nutella” buddy, Volkan, has really taught me a lot about EXAFS measurements. I will never forget the fun we had during night shift and the time when we were rejected to enter a pub at Glasgow after queuing up for hours.

Special thanks to my (ex)office mates – Sami, Farid and Lu, for the help through the years and the conducive working environment. It was nice to share the office with them and I enjoyed the occasional small chats we had. Lunch is always enjoyable with lots of discussion, gossips and laughter with – Alessandro, Guanna, Leilei (also “suffering” with me during TEM), Tianwei, Yi, Chaochao, Lu and Weiyu. I am also grateful to Aless for his help in many work and non-work related things as well.

I would like to also extend my appreciation to other current members of IMC for all the random discussions we had and strong support given to me: Tonek, Pieter Magusin, Peng, Christiaan, Xueqing, Burcu, Xiaochun, William (Graaff Graaff), Lennart, Georgy (collaboration in OGO), Nikolay, Bartek, Quanbao, Tamas, Xiaoming, Kaituo, Anton, Xuefang, Lingqian, Yi Ma, Kristina, Venkata, Jae and Jose. I have also benefitted and enjoyed working with previous members of IMC: Xiaobo, Haodong, Yanmei, Guo Qiang, Arjan, Pieter, Remco, Shuxia, Victor, Cristina and Meiling. I have enjoyed working with some of the Master/Erasmus students in our group – Arianna, Jeroen, Arno and Roderigh. I am glad that Arianna had enjoyed her time in Eindhoven and managed to find a job that she like in Italy. I would like to also extend my gratitude to various members from the “old” SKA for the discussions, support and fun through these four years – Peter Thune (OGO), Kees-Jan, Ajin (ATR measurements), Basar, Deshen, Hans F., Gilbere and Xuwei.

This thesis will not be possible without the professional technical supports from Johan (for everything), Tiny (XPS), Adelheid (ICP), Paul (TEM), Ad, Brahim and Ton (advice on

autoclaves). The administrative support provided by secretaries of our group Emma and Elize is highly appreciated. Emma, thank you for all the help.

I would like to express my sincere gratitude to Dr. Yanhui Yang (NTU, Singapore), whom I see as my “启萌老师” in research. He was the one who aroused my interest, passion in catalysis research and encouraged me to pursue my PhD outside Singapore.

I am deeply indebted to my parents for their love, support, encouragement and understanding to allow their only child to be working halfway around the globe. There is no way of expressing my love and gratitude for my Ah Ma (grandma). Even though she has left us during my PhD studies, she will always be in my heart. I am also very grateful for family(-in-laws) for visiting me and my wife in Netherlands and for the all the goodies they have brought along with them: – Mummy, Daddy, my mother-in-law, grandma-in-law, Edwin, Bryan, Auntie Dolly and Cherie. I would also like to express my appreciation to Daniel, Camila and their lovely daughter, Ariana, for the support given to us during the cosy weekend dinners, where we discuss about our futures, careers and I definitely benefitted from the “mock interview” role play that we did together.

Last but certainly not least, I am really very appreciative to my wife for her love, support, understanding for all these years. It was her firm encouragement that allowed me to embark on the more challenging journey to pursue my dreams in Netherlands. I am very thankful of what she has done all these years to allow me to focus on my research work, especially for single-handedly organising our wedding and renovation works for our beautiful new house in Singapore. I was ecstatic when she was finally able to join me in Netherlands in 2012. Let us unfold the next phase of our life together. 宝贝, I love you.

I would also like to thank all the people who were not mentioned above but helped and supported me in one way or another during the past four years.

List of Publications

1. X.Y. Quek, Y. Guan, R.A. van Santen, E.J.M. Hensen, "Ionic-liquid stabilized rhodium nanoparticles for citral cyclodehydration" *ChemSusChem* **2010**, 3, 1264-1267.
2. X.Y. Quek, Y. Guan, R.A. van Santen, E.J.M. Hensen, "Unprecedented oxygenate selectivity in aqueous-phase Fischer-Tropsch synthesis by ruthenium nanoparticles" *ChemCatChem* **2011**, 3, 1735-1738.
3. X.Y. Quek, Y. Guan, E.J.M. Hensen, "Structure sensitivity in the hydrogenation of unsaturated hydrocarbons over Rh nanoparticles", *Catal. Today* **2012**, 183, 72-78.
4. X. Li, X.Y. Quek, D.A.J.M. Ligthart, M. Guo, Y. Zhang, C. Li, Q. Yang, E.J.M. Hensen, "CO-PROX reactions on copper cerium oxide catalysts prepared by melt infiltration" *Appl. Catal. B*, **2012**, 123-124, 424-432.
5. Y. Zhang, X.Y. Quek, L. Wu, Y. Guan, E.J.M. Hensen, "Palladium nanoparticles entrapped in polymeric ionic liquid microgels as recyclable catalysts for hydrogenation reactions" **2013**, *submitted*.
6. X.Y. Quek, R. Pestman, R.A. van Santen, E.J.M. Hensen, "Effect of the organic capping agent on Ru-nanoparticle catalyzed aqueous phase Fischer-Tropsch synthesis" **2013**, *submitted*.
7. X.Y. Quek, R. Pestman, I.A.W. Filot, V. Petkov, R.A. van Santen, E.J.M. Hensen, "Identification of catalytic reaction centers for low barrier CO dissociation: a high-energy x-ray diffraction and modelling study of Ru nanoparticles" **2013**, *in-preparation*.
8. X.Y. Quek, R. Pestman, I.A.W. Filot, V. Petkov, R.A. van Santen, E.J.M. Hensen, "Ruthenium nanoparticle catalyzed aqueous phase Fischer-Tropsch synthesis" **2013**, *in-preparation*.

Other Publications

9. X.Y. Quek, Q.H. Tang, S. Hu, Y. Yang, "Liquid phase *trans*-stilbene epoxidation over highly active cobalt substituted TUD-1 mesoporous materials" *Appl. Catal. A*, **2009**, 361, 130-136.
10. D. Liu, X.Y. Quek, W.N.E. Cheo, R. Lau, A. Borgna, Y. Yang, "MCM-41 supported nickel-based bimetallic catalysts with superior stability during carbon dioxide reforming of methane: Effect of strong metal-support interaction" *J. Catal.*, **2009**, 266, 380-390.
11. D. Liu, X.Y. Quek, S. Hu, L. Li, H.M. Lim, Y. Yang, "Mesoporous TUD-1 supported molybdophosphoric acid (HPMo/TUD-1) catalysts for n-heptane hydroisomerization" *Catal. Today*, **2009**, 147, S51-S57.

12. D. Liu, X.Y. Quek, H.H.A. Wah, G. Zeng, Y. Li, Y. Yang, "Carbon dioxide reforming of methane over nickel grafted SBA-15 and MCM-41 catalyst" *Catal. Today*, **2009**, *148*, 243-250.
13. X.Y. Quek, D. Liu, W.N.E. Cheo, H. Wang, Y. Chen, Y. Yang, "Nickel grafted TUD-1 mesoporous catalysts for carbon dioxide reforming of methane" *Appl. Catal. B*, **2010**, *95*, 374-382.
14. H. Wang, B. Wang, X.Y. Quek, L. Wei, J. Zhao, L.J. Li, M.B. Chan-Park, Y. Yang, Y. Chen, "Selective Synthesis of (9,8) Single walled carbon nanotubes on cobalt incorporated TUD-1 catalysts" *J. Am. Chem. Soc.*, **2010**, *132*, 16747-16749.

Curriculum Vitae

Xian-Yang Quek was born in Singapore on November 9th 1983. After graduating from Singapore Polytechnic with a Diploma in Chemical Engineering in 2003, he served as a combat engineer platoon commander in the Singapore Armed Forces from 2003 to 2005. In 2009, he graduated from Nanyang Technological University (Singapore) with a Bachelor of Engineering (Chemical and Biomolecular Engineering) with a First Class honors. He was in the Dean's list from 2006-2009 and also received the University Scholar award in 2009. During his Bachelor studies, he performed research on heterogeneous catalysis in the group of dr. Yanhui Yang from 2006 to 2009. In May 2009, Xian-Yang started his PhD project on Fischer-Tropsch synthesis in the Schuit Institute of Catalysis, Laboratory of Inorganic Materials Chemistry at the Eindhoven University of Technology under the supervision of prof.dr.ir. Emiel J.M. Hensen and prof.dr. Rutger A. van Santen. The aim of his project is to study the structure sensitivity of nanoparticle catalysis for several chemical reactions, with emphasis on Fischer-Tropsch synthesis. These 4 years of PhD study in TU/e will served as a solid foundation for Xian-Yang to continue to pursue his ambition and passion in R&D as a Research Scientist at Johnson Matthey Technology Centre, Sonning Common, UK.